



LAPPEENRANTA  
UNIVERSITY OF TECHNOLOGY

*Lassi Aarniovuori*

·  
·  
·  
·

## **INDUCTION MOTOR DRIVE ENERGY EFFICIENCY – SIMULATION AND ANALYSIS**

*Thesis for the degree of Doctor of Science  
(Technology) to be presented with due  
permission for public examination and  
criticism in the Auditorium 1381 at  
Lappeenranta University of Technology,  
Lappeenranta, Finland on the 27th of  
August, 2010, at noon.*

Acta Universitatis  
Lappeenrantaensis  
**396**

Supervisor Professor Juha Pyrhönen  
Institute of Energy Technology  
Department of Electrical Engineering  
Lappeenranta University of Technology  
Lappeenranta, Finland

Reviewers Professor Bimal Bose  
The University of Tennessee  
Department of Electrical Engineering and Computer Science  
Knoxville, USA

Ph.D. Yujing Liu  
ABB Corporate Research  
Västerås, Sweden

Opponents Professor Bimal Bose  
The University of Tennessee  
Department of Electrical Engineering and Computer Science  
Knoxville, USA

Ph.D. Yujing Liu  
ABB Corporate Research  
Västerås, Sweden

ISBN 978-952-214-962-6  
ISBN 978-952-214-963-3 (PDF)  
ISSN 1456-4491

Lappeenrannan teknillinen yliopisto  
Digipaino 2010

## **ABSTRACT**

Lassi Aarniovuori

### **Induction Motor Drive Energy Efficiency - Simulation and Analysis**

Lappeenranta 2010

128 p.

Acta Universitatis Lappeenrantaensis 396

Diss. Lappeenranta University of Technology

ISBN 978-952-214-962-6, ISBN 978-952-214-963-3 (PDF), ISSN 1456-4491

A coupled system simulator, based on analytical circuit equations and a finite element method (FEM) model of the motor has been developed and it is used to analyse a frequency-converter-fed industrial squirrel-cage induction motor. Two control systems that emulate the behaviour of commercial direct-torque-controlled (DTC) and vector-controlled industrial frequency converters have been studied, implemented in the simulation software and verified by extensive laboratory tests.

Numerous factors that affect the operation of a variable speed drive (VSD) and its energy efficiency have been investigated, and their significance in the simulation of the VSD results has been studied.

The dependency of the frequency converter, induction motor and system losses on the switching frequency is investigated by simulations and measurements at different speeds for both the vector control and the DTC. Intensive laboratory measurements have been carried out to verify the simulation results.

Keywords: Simulation, combined simulation, modelling, frequency converter, electric drives, direct torque control, vector control, losses, converter-caused losses, loss distribution, energy efficiency

UDC 621.3.017 : 621.313.333 : 681.532.55 : 621.314.26 : 004.942 : 681.5.017



## **ACKNOWLEDGEMENTS**

The research documented in this thesis was carried out between the years 2006 and 2010 in the LUT Institute of Energy Technology (LUT Energia) at Lappeenranta University of Technology (LUT). This research project was funded by ABB.

I wish to thank all the people involved in this process, I express my gratitude to Professor Juha Pyrhönen, the supervisor of the thesis for his valuable comments and corrections to the work.

The effort and comments of pre-examiners Professor Bimal K. Bose and Dr. Yujing Liu are greatly appreciated.

The author wishes to thank Dr. Markku Niemelä for his valuable guidance throughout the work and Dr. Lasse Laurila for the collaboration and encouragement during the years. I wish to thank the entire project group of ABB, who have participated in this research project.

Special thanks are due to Dr. Hanna Niemelä for reviewing and improving the language of this work and Mr. Martti Lindh for the laboratory arrangements.

Financial support for this work by Walter Ahlström Foundation, the Finnish Foundation for Technology Promotion and Ulla Tuominen Foundation is gratefully appreciated.

I also express my gratitude to my colleagues, friends and especially my family for their help and support during this process.

Lappeenranta, August 2010

*Lassi Aarniovuori*



## CONTENTS

1	INTRODUCTION.....	11
1.1	Electrical drive systems - variable speed drives.....	11
1.2	Improving energy efficiency of an electric motor drive system.....	12
1.3	Principles of pulse width modulation for electric power converters .....	13
1.3.1	Principles of space vector theory.....	13
1.4	Space Vector Modulation (SVM) .....	17
1.5	Control methods.....	23
1.5.1	Coordinate transformation and reference frames.....	24
1.5.2	DTC.....	25
1.5.3	Vector control – symmetrical two-phase modulation .....	27
1.6	Simulation .....	28
1.7	Scope of the work and outline of the thesis .....	30
1.8	Scientific contributions of the doctoral thesis.....	31
2	HARMONICS AND HARMONIC ANALYSIS METHODS .....	34
2.1	Harmonic analysis.....	34
2.2	Harmonic sources.....	34
2.3	Effects of harmonics on rotating machines.....	35
2.4	Discrete Fourier Transformation (DFT).....	36
2.5	Harmonic distortion .....	37
3	LOSSES.....	40
3.1	Converter losses.....	40
3.1.1	Input inductor losses .....	40
3.1.2	Diode bridge losses.....	41
3.1.3	Intermediate circuit losses.....	41
3.1.4	IGBT module losses .....	42
3.1.5	Inverter extra losses .....	42
3.2	Induction machine losses.....	43
3.2.1	Simulated motor losses .....	43
3.3	Resistive losses .....	44
3.3.1	Iron loss model.....	44
3.4	Drive system losses.....	45
4	SIMULATION MODELS .....	47
4.1	Overview of the simulator .....	47
4.2	Frequency converter model .....	48
4.2.1	Diode bridge and intermediate circuit.....	48
4.2.2	Inverter model.....	50
4.3	Frequency converter nonidealities .....	50
4.3.1	Current measurement delay and A/D conversion .....	50
4.3.2	Dead time.....	51
4.4	Motor models.....	52
4.4.1	Analytical motor models.....	52
4.4.2	FEM model .....	54
4.5	Coupled simulation .....	55
4.6	Process model .....	55
4.7	Model of the control system .....	55
4.7.1	Model of the direct torque control system.....	55
4.7.2	Model of the rotor-flux-oriented current control .....	58

5	ANALYSIS OF MEASUREMENTS AND SIMULATION RESULTS .....	61
5.1	Spectra in the DTC.....	62
5.2	Effect of current measurement delay in the DTC.....	68
5.3	Analysis of the measured data .....	70
5.4	Calculating the switching frequency and voltage vectors.....	71
5.5	Spectrum analysis with the analytical and the FEM motor model .....	75
5.6	Effect of the time step length in the FEA of the frequency-converter fed IM.....	80
5.7	Effect of dead time in the simulation results.....	85
5.8	Comparison of simulation results and measurements at the nominal point with a sinusoidal supply.....	87
6	COMPARISON OF THE MEASURED AND SIMULATED LOSSES .....	88
6.1	25 Hz operating point.....	88
6.2	40 Hz operating point.....	93
6.3	50 Hz operating point.....	98
6.4	Concluding remarks .....	104
6.5	Torque ripple .....	108
7	CONCLUSION .....	109
7.1	Suggestions for further work .....	110
	APPENDIX A PARAMETERS OF THE DRIVE SYSTEMS.....	116
	APPENDIX B EFFICIENCY MEASUREMENTS OF THE 37 KW INDUCTION MOTOR.....	120
	APPENDIX C SPECTRA FIGURES .....	122

## ABBREVIATIONS AND SYMBOLS

### Roman letters

<i>A</i>	magnetic vector potential
<i>B</i>	flux density
<i>d</i>	direct axis quantity in the rotating reference frame
<i>f</i>	frequency
<i>I</i>	current
<i>j</i>	imaginary unit
<i>J</i>	mechanical inertia
<i>J</i>	current density
<i>L</i>	inductance
<i>M</i>	modulation index
<i>n</i>	rotational speed
<i>p</i>	number of pole pairs
<i>P</i>	power
<i>q</i>	quadrature axis quantity in the rotating reference frame, number of slots per pole and phase
<i>R</i>	resistance
<i>S</i>	switch state
<i>t</i>	time
<i>T</i>	torque, duration time
<i>U</i>	voltage

### Greek letters

$\alpha$	real axis quantity in the stationary reference frame
$\beta$	imaginary axis quantity in the stationary reference frame
$\psi$	flux linkage
$\eta$	efficiency
$\theta$	phase shift
$\omega$	angular frequency

### Acronyms

ABB	ASEA Brown Boveri
AC	Alternating Current
CO <sub>2</sub>	Carbon Dioxide
DFT	Discrete Fourier Transform
DOL	Direct-On-Line
DTC	Direct Torque Control
DPWM	Discontinuous Pulse-Width-Modulation
ESR	Equivalent Series Resistance
EU	European Union
FEM	Finite Element Method
IGBT	Insulated Gate Bipolar Transistor
IGCT	Integrated Gate-Commutated Thyristor
MOSFET	Metal-Oxide-Semiconductor Field-Effect Transistor

PMSM	Permanent Magnet Synchronous Machine
PWM	Pulse-Width-Modulation
RMS	Root Mean Square
SCR	Short Circuit Ratio
TEFC	Totally Enclosed Fan Cooled
THD	Total Harmonic Distortion
TD	Total Distortion
VC	Vector Control
VSC	Voltage Source Converter
VSD	Variable Speed Drive

### Subscripts

$\sigma$	leakage
C	conducting
e	electrical
est	estimated
F	flux
fund	fundamental wave
m	magnetizing
M	magnetizing ( $\Gamma$ -equivalent circuit)
mech	mechanical
R	rotor ( $\Gamma$ -equivalent circuit)
r	rotor (T-equivalent circuit)
T	torque
s	stator
sw	switching

## 1 INTRODUCTION

Electrical drives play an important role in the field of energy efficiency. Modern power electronic drives provide good opportunities to efficiently control the energy flows. The global concern over climate change results in an increasing use of electrical drives in industrial and other processes. According to the present understanding, the reduction of carbon dioxide (CO<sub>2</sub>) emissions is one of the most important targets in the future. Among other issues, this can be reached by reducing the amount of energy consumed. Electric motors are the most important type of electric load. They are used in all sectors from households to the industry and commercial sector. Electric motors are used in a wide range of applications, such as fans, compressors, pumps, mills, elevators, transports and cars. Electric motors use over half of all electricity consumed in developed countries, and hence, it is important to utilize electric energy in electric motor drives as efficiently as possible. In the European Union (EU), electric-motor-driven systems are by far the most important type of load in industry, using about 70 % of the consumed electricity (Almeida et al., 2001). According to de Almeida, et al. (2001), electric motor systems consume about one third of all energy in the tertiary sector. Therefore, as electric motor drives are used widely in various sectors, they are an attractive target for energy efficiency improvements. The wide use of drive systems provides a large potential for significant energy savings. Even small efficiency improvements would produce extensive savings globally (de Almeida et al., 2001). The problem, however, is that drives are slowly replaced by new ones as the lifetime of a correctly designed drive can reach 30 years.

The price of the electrical energy that a motor consumes over its lifespan is multiple times the motor purchase price. The cost savings are the most important motivation to the industry to move on to more energy efficient solutions.

Considering the industrial processes, one may come to different savings potentials, but the key challenges to the increased efficiency in systems driven by electrical machines lie in the following three targets: 1) to extend the application areas of variable-speed electric drives using power electronics to efficiently control the drive, 2) to integrate the drive and the driven load to maximize system efficiency and 3) to increase the efficiency of the electrical drive itself.

### 1.1 Electrical drive systems - variable speed drives

The main function of a variable speed drive (VSD) is to control the power flow from the mains to the load. Variable speed drives are established when an electric motor is combined with a power electronic converter. By introducing variable speed to the driven load, it is possible to optimize the efficiency of the entire system, and it is in this area that the greatest efficiency gains are possible. Fig 1.1 describes the general elements of a power electronic drive system. It can be seen that several electric components lie in the route of the power flow from the mains to the process. Important elements of this chain are frequency converters and motors whose efficiency will be studied in detail in this thesis. So far, the efficiency improvement of the drive system based on the process optimization has been good enough and the frequency converter and motor losses have almost been ignored. But now the time has arrived when the efficiency of the converter itself should be increased and the converter-caused losses in the motor minimized. Induction motors are by far the most widely used motor in the power range of 1–150 kW using over 90 % of the electricity consumed by all motors in that range (de Almeida et al., 2000). Therefore, the induction motor energy efficiency is a hot topic, and environmental aspects are setting new standards. The International Electrotechnical Commission (IEC) has introduced new standards relating to energy efficient motors. IEC 60034-30 (2008) defines three new IE (Internal Efficiency) classes: standard efficiency (IE1), high efficiency (IE2) and premium

efficiency (IE3) for single-speed, three-phase, cage induction motors, and IEC 60034-2-3 is a new testing standard under development that defines specific test methods for determining the losses and efficiency of converter-fed AC machines.

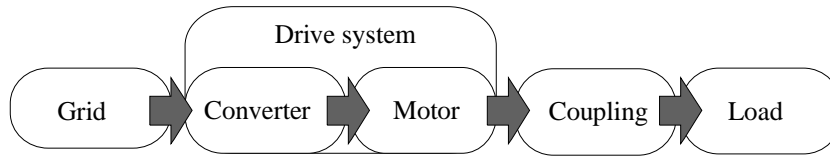


Fig 1.1. Elements of a modern drive system.

## 1.2 Improving energy efficiency of an electric motor drive system

There are various methods to improve the energy efficiency of electric drives: One obvious option is to select the best available motor technology for the variable speed drive (VSD). An ultimate solution for a VSD motor is to use copper rotor windings, an optimized rotor slot form and high-quality lamination stacks instead of standard motor materials. However, the best improvements in the drive performance can be achieved by replacing constant-speed mechanically controlled processes with variable-speed-controlled processes or by replacing DC motor drives with induction motor VSDs. New very efficient motor types such as permanent magnet synchronous motors may also be used instead of the induction motor, but as the induction motor still remains the workhorse of the industry, this thesis concentrates on its performance in a variable speed drive.

In most cases, the majority of the efficiency increase can be achieved by the improved system efficiency, which very often, but not always, can be obtained with a variable-speed drive. The state-of-the-art silicon-semiconductor-based inverter technology for feeding AC motors in variable speed drives has rated efficiencies of roughly 96–98 %; this may seem high, but in practice, there still remains development work to be done. Hence, it is important to analyse carefully where the losses of a variable speed drive exactly take place.

According to de Almeida (2005), the greatest potential for energy savings by variable speed drives can be found in the area of fluid-flow applications (pumps, compressors, fans) with variable flow requirements. Pumps and fans of this kind are often run well below their rated power, in which case fixed-speed machines are run in an ‘on-off’ manner. However, the power requirement is related to the cube of the flow, so that if for instance running a pump continuously at half speed produces a large enough pressure difference, it will produce the same flow as one at full speed for one-half of the time, but will only require only one-quarter of the energy. On the other hand, it should be borne in mind that the frequency converter should not be placed in the application that is running with a constant speed; in a constant-speed application, the frequency converter losses are wasted, while a properly chosen DOL (Direct-On-Line) motor and pump could be a more energy efficient alternative than a VSD.

Some of this improvement arises from the efficiency of the machine. However, the efficiencies of motors cannot be significantly increased further, but there is still clearly something to be done also in this field, especially in matching the motor and converter together. The induction machine is at the moment the most commonly used machine type despite the fact that PM machines have a better efficiency. Induction motor design could focus on the inverter drive, but typically, the same designs are used in DOL drives and VSDs thereby sacrificing the drive efficiency to some degree.

Alternative solutions to improve the efficiency are the integration of mechatronics, the use of direct drives, where gearboxes are replaced by speed control or the use of compact drives where the motor and the power drive are integrated. For instance, each cogwheel contact may consume one per cent of the energy flow running through a gearbox (Polinder et al., 2006). Thus, a two-stage gearbox generates heat as efficiently as a modern frequency converter.

An optimal control of the energy flow provides yet another way to reduce the losses in a motor drive. In frequency-converter-fed induction motor drives, there is also the option to reduce the drive losses by adjusting the motor magnetization level according to the motor load. This iron loss saving method is a well-known technique, which is applied to various kinds of electrical machines and which is implemented in different control algorithms.

The whole drive system must be carefully dimensioned to obtain low losses. The sizing of the industrial process instrumentation starts from the actuator. Motors rarely operate at their full-load point. In the European Union and the USA, field tests indicate that, on average, the motors operate at around 60 % of their rated load. The induction motor efficiency often peaks near 75 % of the full load and is relatively flat down to the 50 % load point (de Almeida et al., 2000). Motors in the larger size ranges can operate with a reasonably high efficiency at loads down to 30 % of the rated load.

By adopting well-known, proven concepts, it is possible to increase the efficiency of systems driven by electrical machines and reduce the total electricity consumption. According to Binder (2008), the largest savings potential of about 20 % is given by the optimization of the whole drive system. The efficiency of an electrical machine is a complex function of machine type, size, speed of operation, loadings, materials and operating conditions, and will not be studied here in detail.

### **1.3 Principles of pulse width modulation for electric power converters**

In many industrial applications, it is often required to control the output voltage of the inverter for the constant voltage to frequency ratio control of the induction machine. In the literature, various pulse width modulation (PWM) methods have been suggested to control the output voltage waveform of the inverter. Two different principles based on a variable and constant switching frequency have been selected for the analysis, namely the direct torque control (DTC) (Depenbrock, 1988), (Noguchi and Takahashi, 1986) and the symmetrical two-phase modulation (van der Broeck, 1991). They are discussed in the following sections. The principle of the PWM is simple. In voltage source converters (VSCs), the mains voltage is rectified by a rectifier bridge and the following intermediate circuit constant DC voltage is connected to the motor phases by using variable pulse lengths. The pulse lengths are controlled to create the desired fundamental wave frequency and amplitude. The PWM pattern is controlled by the control system. The basic idea of the control system is to keep the desired speed, frequency or torque of the machine as close to its reference value as possible. The target can be achieved by using different controllable variables such as stator flux and torque or rotor flux and stator current. A wide variety of control systems can be implemented in different reference frames such as stator, air gap flux linkage, rotor flux linkage or rotor reference frame.

#### **1.3.1 Principles of space vector theory**

The single-phase equivalent circuit represents the motor using sinusoidal voltages in the continuous state. The investigation of the dynamical behaviour of the electrical motors is usually carried out with the space vector theory, which was proposed by Kovács and Rácz

(1959) when studying the transient phenomena in AC machines. Even though the space vector theory is developed to investigate the dynamic behaviour in AC machines, the theory is useful also when analysing any electrical multiphase system.

In the space vector theory, the flux density in the air gap is assumed to be sinusoidal, the saturation of the magnetizing circuit is assumed constant, and iron losses are zero. Additionally, the resistances and inductances are assumed to be independent of frequency and temperature. In the space vector theory, the coils divided into several slots or non-salient poles are presented with concentrated windings that are symmetrically divided into the three magnetic axes of the motor. The concentrated windings are located 120 electric degrees apart from each other, and they are assumed to produce a sinusoidal distribution of current linkage that is assumed to have its peak value in the direction of the magnetic axis of the original winding.

When investigating a universal three-phase system, rotating at an angular speed  $\omega$ , the instantaneous phase quantities of the system can be written

$$x_U(t) = \hat{x}_U \cos(\theta(t) + \phi_U(t)), \quad (1.1)$$

$$x_V(t) = \hat{x}_V \cos(\theta(t) - 2\pi/3 + \phi_V(t)), \quad (1.2)$$

$$x_W(t) = \hat{x}_W \cos(\theta(t) - 4\pi/3 + \phi_W(t)), \quad (1.3)$$

where  $\hat{x}$  is the peak value of the phase quantity and the phase angle

$$\theta(t) = \int_0^{t_1} \omega(t) dt + \theta(0). \quad (1.4)$$

This kind of a three-phase system can be presented by using the space vector theory with a complex space vector  $\mathbf{x}^s(t)$  and a real zero sequence component  $x_0(t)$ , which are denoted as

$$\mathbf{x}^s = c [\mathbf{a}^0 x_U(t) + \mathbf{a} x_V(t) + \mathbf{a}^2 x_W(t)] \text{ and} \quad (1.5)$$

$$x_0 = c_0 [x_U(t) + x_V(t) + x_W(t)], \quad (1.6)$$

where  $a = e^{j2\pi/3}$  is the phase shift operator. This definition is applicable to the currents, voltages or flux linkages needed in the analysis of electric motors. The superscript  $s$  denotes that the vector is presented in a stationary reference frame. The direction of the stationary or stator reference frame is usually chosen to be in the direction of the a-phase magnetic axis. The gains  $c$  and  $c_0$  are scaling factors. Typical values for  $c = 2/3$  and  $c_0 = 1/3$ , when the magnitude of the space vector is equal to the peak value of the phase quantity. Also other scaling factors are used in the literature, but as a disadvantage, we cannot then use directly the equivalent circuit parameters from star connection. For instance when  $c = \sqrt{2/3}$  and  $c_0 = 1/\sqrt{3}$ , we may create a power invariant definition for space vectors, and the voltage vector amplitude corresponds to the RMS value of the line-to-line voltage in a symmetrical three-phase system.

In Fig 1.2 we observe how the voltage vectors are created. To generate the voltages  $u_A$ ,  $u_B$  and  $u_C$ , the switches are connected to the potentials of the DC link. When considering the windings of an electrical machine, we may state that the possible voltages acting in the windings are, in principle, dependent on the switching situation,  $\pm 2/3 u_{DC}$ ,  $\pm 1/3 u_{DC}$  and 0. The output voltage vector now obtains the values:

$$\begin{aligned}
 \mathbf{u}_0 &= 0, \\
 \mathbf{u}_1 &= \frac{2}{3} u_{DC} \mathbf{a}^0, \\
 \mathbf{u}_2 &= -\frac{2}{3} u_{DC} \mathbf{a}^2, \\
 \mathbf{u}_3 &= \frac{2}{3} u_{DC} \mathbf{a}^1, \\
 \mathbf{u}_4 &= -\frac{2}{3} u_{DC} \mathbf{a}^0, \\
 \mathbf{u}_5 &= \frac{2}{3} u_{DC} \mathbf{a}^2, \\
 \mathbf{u}_6 &= -\frac{2}{3} u_{DC} \mathbf{a}^1, \\
 \mathbf{u}_7 &= 0.
 \end{aligned} \tag{1.7}$$

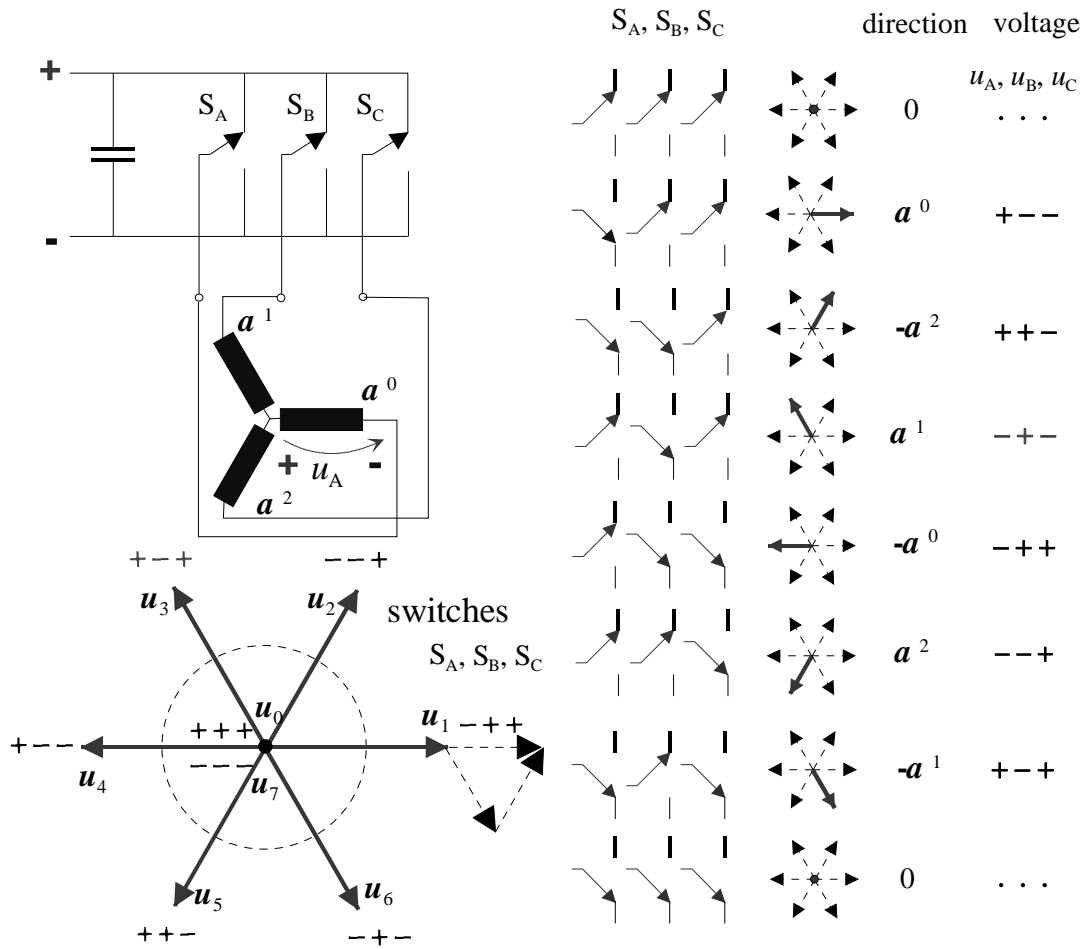


Fig 1.2. Switching alternatives of a three-phase inverter with a VSI and the directions of the possible output voltage vectors, which are the positive and negative directions of the magnetic axes of the phase windings. The zero value of the output voltage has no direction. Note that the right-hand column determines the direction of the voltage experienced by the windings, which is signed positive, when the direction corresponds to the direction of the voltage of the motor winding according to the figure ( $u_A$ ). The voltage signs of the switch positions are thus exactly opposite to the signs of the voltages experienced by the windings. This distinction has to be made in order for the positive voltage vector to produce a parallel current vector in the windings. In Fig 1.2 the voltages are arranged so that a positive voltage vector also produces a positive corresponding current vector (Pyrhönen, 2009).

The right-hand notations of Fig 1.2 represent those values that have to be substituted to the equation of the voltage vector in order for the directions of the current and voltage vectors to be convergent.

#### 1.4 Space Vector Modulation (SVM)

SVM is one of the most generic space vector modulating methods. It was shown above that the inverter bridge generates the voltage vectors together with the motor windings. The vectors can now be employed in space vector modulation. The complex reference vector of the modulator for the voltage is written as

$$\mathbf{u}_{\text{ref}} = u_{\text{ref}} e^{j\theta} = u_{\alpha,\text{ref}} + j u_{\beta,\text{ref}} \quad (1.8)$$

Fig 1.3 illustrates the principle of space vector modulation.

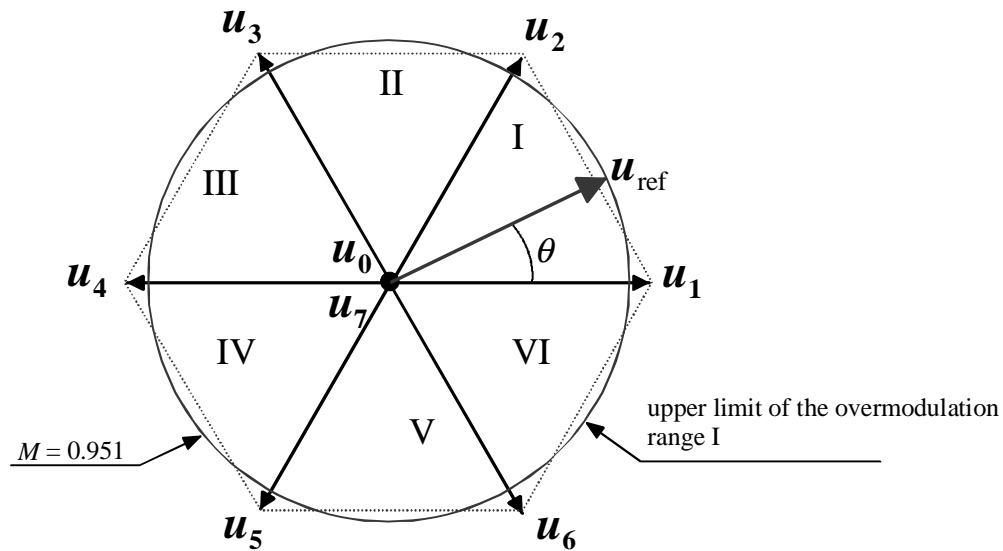


Fig 1.3. Voltage vectors  $\mathbf{u}_0 \dots \mathbf{u}_7$  of the voltage source inverter. Active vectors and zero vectors are shown. The reference vector ( $\mathbf{u}_{\text{ref}}$ ) and its generation from active vectors are shown. The outer hexagon indicates the maximum length of the voltage vector at each point. The circle inside the hexagon indicates the locus of the maximum voltage vector producing a sinusoidal output. The length of the corresponding voltage vector is  $2/3 U_{\text{DC}}$  (Pyrhönen, 2009).

The reference vector is sampled at a fixed clock frequency. The time duration of the modulation sequence  $T_{\text{sw}}$  can be determined as dependent on the switching frequency  $f_{\text{sw}}$

$$T_{\text{sw}} = 2T_{\text{sub}} = \frac{1}{f_{\text{sw}}}. \quad (1.9)$$

Here  $T_{\text{sub}}$  is the duration of the modulation subsequence. The voltage vector according to the sampling of the reference vector is constructed by the space vectors illustrated in Fig 1.3. The complex plane is subdivided according to Fig 1.3 into six equal sectors, the active vectors acting as the sides of the sectors. Modulation in the sector I is based on the equation

$$\mathbf{u}_{\text{ref}} T_{\text{sub}} = t_1 \mathbf{u}_1 + t_2 \mathbf{u}_2 + t_0 \mathbf{u}_{0,7} \quad T_{\text{sub}} = t_1 + t_2 + t_0. \quad (1.10)$$

The construction of the reference vector by modulation requires two active vectors and both zero vectors. In Fig 1.3, the reference vector is generated in the sector I by selecting the active vectors  $\mathbf{u}_1$  and  $\mathbf{u}_2$  and both the zero vectors  $\mathbf{u}_0$  and  $\mathbf{u}_7$ . The switching durations  $t_1$  and  $t_2$  are calculated for the selected active vectors, the on-duration  $t_1$  being the switching duration of the vector on the leading edge, and  $t_2$  being the on-duration on the trailing edge. The formulae for the switching durations for active vectors are given in Table 1.1. For instance in the sector I, the on-duration  $t_1$  can be calculated by the sine rule from the triangle of Fig 1.3, defined by the voltage vectors  $\mathbf{u}_1$  and  $\mathbf{u}_2$ .

The symbol  $M$  in the definitions denotes the modulation index determined for instance by Holtz (1994), this modulation index

$$M = \frac{\hat{u}_{\text{ref}}}{\hat{u}_{6p,1}} = \frac{\hat{u}_{\text{ref}}}{\frac{2}{\pi} U_{\text{DC}}}; \quad \hat{u}_{6p,1} = \frac{2}{\pi} U_{\text{DC}} \quad (1.11)$$

being now different from the modulation index of the modulation based on the sine-triangle comparison. In (1.11)  $\hat{u}_{\text{ref}}$  is the length of the reference vector (i.e., the peak value of the respective phase voltage curve) and  $U_{\text{DC}}$  is the voltage of the intermediate DC link.  $M$  is thus now the ratio of the peak voltage to the peak value of the fundamental harmonic of the phase voltage obtained by the six-pulse modulation.

The modulation index  $M$  increases from 0 to 0.907 while the output frequency and voltage of the modulator increase linearly. The utilization of zero vectors stops at  $M = 0.907$ . When  $M > 0.907$  the modulator enters the overmodulation range I, and after  $M = 0.951$  the modulator enters the overmodulation range II, at the upper limit of which only a square wave output is found and the machine stator flux linkage follows a hexagonal path (Holtz 1994).

Table 1.1. Switching durations of the active voltage vectors in the space vector modulation.

Sector	Location angle of the reference vector	Active voltage vectors used in modulation	Switching durations of the active voltage vectors
I	$0 \leq \theta < \frac{\pi}{3}$	$\mathbf{u}_1$ $\mathbf{u}_2$	$t_1 = \frac{\sqrt{3}}{2} MT_{\text{sub}} \cdot \sin\left(\frac{\pi}{3} - \theta\right)$ $t_2 = \frac{\sqrt{3}}{2} MT_{\text{sub}} \cdot \sin(\theta)$
II	$\frac{\pi}{3} \leq \theta < \frac{2\pi}{3}$	$\mathbf{u}_2$ $\mathbf{u}_3$	$t_1 = \frac{\sqrt{3}}{2} MT_{\text{sub}} \cdot \sin\left(\frac{2\pi}{3} - \theta\right)$ $t_2 = \frac{\sqrt{3}}{2} MT_{\text{sub}} \cdot \sin\left(\theta - \frac{\pi}{3}\right)$
III	$\frac{2\pi}{3} \leq \theta < \pi$	$\mathbf{u}_3$ $\mathbf{u}_4$	$t_1 = \frac{\sqrt{3}}{2} MT_{\text{sub}} \cdot \sin(\pi - \theta)$ $t_2 = \frac{\sqrt{3}}{2} MT_{\text{sub}} \cdot \sin\left(\theta - \frac{2\pi}{3}\right)$
IV	$\pi \leq \theta < \frac{4\pi}{3}$	$\mathbf{u}_4$ $\mathbf{u}_5$	$t_1 = \frac{\sqrt{3}}{2} MT_{\text{sub}} \cdot \sin\left(\frac{4\pi}{3} - \theta\right)$ $t_2 = \frac{\sqrt{3}}{2} MT_{\text{sub}} \cdot \sin(\theta - \pi)$
V	$\frac{4\pi}{3} \leq \theta < \frac{5\pi}{3}$	$\mathbf{u}_5$ $\mathbf{u}_6$	$t_1 = \frac{\sqrt{3}}{2} MT_{\text{sub}} \cdot \sin\left(\frac{5\pi}{3} - \theta\right)$ $t_2 = \frac{\sqrt{3}}{2} MT_{\text{sub}} \cdot \sin\left(\theta - \frac{4\pi}{3}\right)$
VI	$\frac{5\pi}{3} \leq \theta < 2\pi$	$\mathbf{u}_6$ $\mathbf{u}_1$	$t_1 = \frac{\sqrt{3}}{2} MT_{\text{sub}} \cdot \sin(2\pi - \theta)$ $t_2 = \frac{\sqrt{3}}{2} MT_{\text{sub}} \cdot \sin\left(\theta - \frac{5\pi}{3}\right)$

In the linear modulation range, the switching periods of the zero vectors are determined by the on-durations of the active vectors.

$$t_0 = t_7 = \frac{1}{2}(T_{\text{sub}} - t_1 - t_2). \quad (1.12)$$

In the time domain, the converter phase outputs behave as in Fig 1.4. It illustrates a single sequence of the space vector modulation when processing the reference vector of Fig 1.3. Fig 1.4 also shows that one inverter leg passes one switch on – switch off sequence.

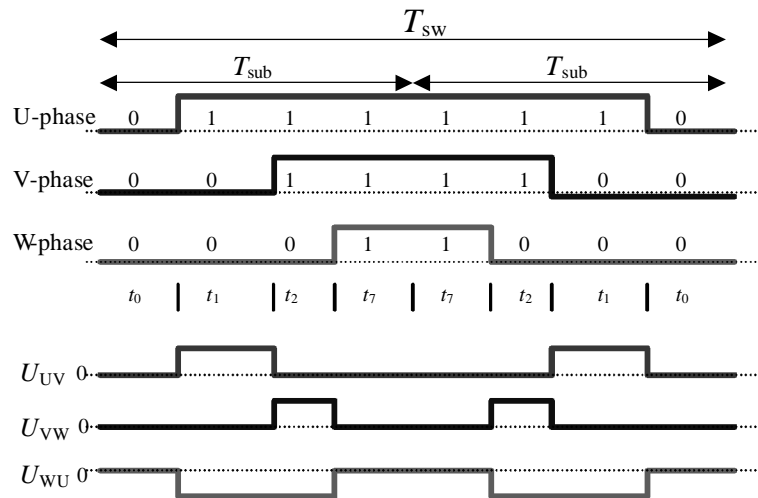


Fig 1.4. Generation of the vector in the switching sequence of the standard SVM and the respective switching durations in the sector I. Voltage vectors  $\mathbf{u}_0$ ,  $\mathbf{u}_1$ ,  $\mathbf{u}_2$  and  $\mathbf{u}_7$  are applied in such a way that two change-over switches are never switched simultaneously (Pyrhönen 2009).

### Overmodulation

The modulation methods use active and zero vectors to create a desired frequency and amplitude of the fundamental voltage waveform. In the overmodulation region in Fig 1.5, the zero vectors are no more used, because the switching durations of zero vectors would be negative.

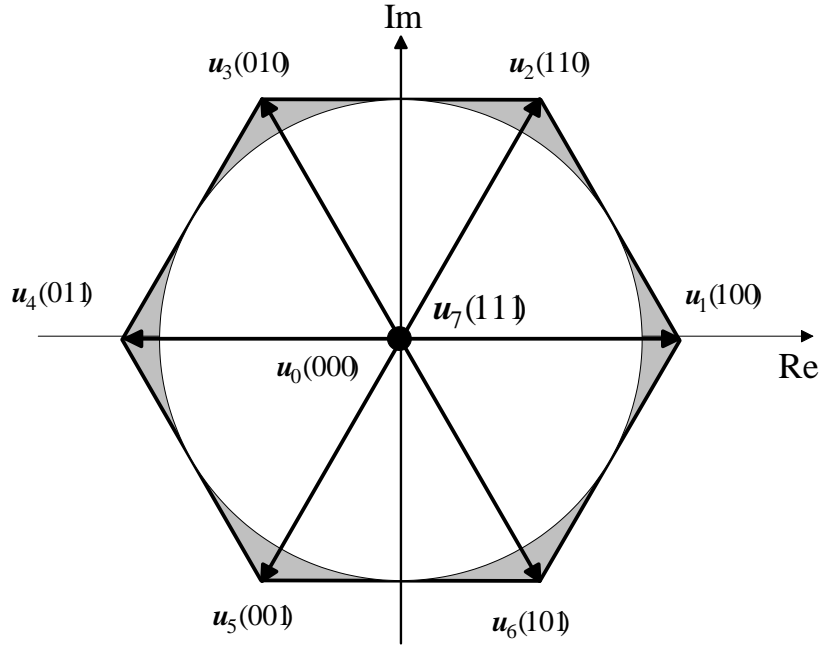


Fig 1.5. Two-level inverter voltage vectors and overmodulation. The overmodulation range is the grey area outside the circle.

The overmodulation region starts, when the desired voltage reference circle in stationary coordinates no longer fits inside the voltage hexagon. The radius of the maximum circle that fits in the voltage hexagon is

$$u_{\max} = \frac{2}{3} \cos\left(\frac{\pi}{6}\right) u_{\text{dc}} = \frac{u_{\text{dc}}}{\sqrt{3}}. \quad (1.13)$$

This gives the modulation index  $0.9069\left(\frac{\pi}{2\sqrt{3}}\right)$ . The modulation index range from 0.9069 to 0.952 is usually called overmodulation area I and when the modulation index is further increased from 0.952 to the six-step mode ( $M = 1$ ), the index range is referred to as overmodulation area II.

In the overmodulation area I, a distorted continuous voltage reference is used. The magnitude of the voltage reference vector is changed while the angle remains unchanged. The reduced fundamental component in the region where the reference trajectory exceeds the hexagon is compensated by a higher value in the corner. The overmodulation area I ends when the stator voltage reference is travelling along the sides of the voltage hexagon.

The distorted discontinuous voltage reference signal is used in the overmodulation area II. Both the reference magnitude and the angle have to be changed compared with the linear region. The modified reference vector is held at a vertex of the hexagon sides in every sector for the rest of the switching period. In the six-step mode, the voltage vector closest to the reference vector is selected for one-sixth of the fundamental period, giving the maximum possible converter voltage (Malinowski, 2001).

### Field weakening

The magnetic field of an AC motor depends on the supply/input voltage–frequency relationship in the motor. Field weakening occurs once the voltage remains constant and the frequency increases. In the field weakening region, the torque decreases in proportion to the increasing speed, and the power remains constant.

More specifically, variable-frequency rotating-field AC motor drives have a linear frequency that depends on the connection between the produced electromotive force  $e$  and the stator flux linkage modulus, defined by the angular speed  $\omega$  of the stator flux linkage vector (Pyrhönen, 1998)

$$|e| = \omega |\psi_s| \quad (1.14)$$

If the motor uses the nominal flux linkage, the maximum available voltage will be reached with a certain speed. This particular speed is called the field weakening point, since the rotating speed cannot be increased above it without decreasing the flux linkage modulus. The speed range above the field weakening point is called the field weakening range or constant power region, whereas the speed below it is called the nominal speed range or constant flux range. The difference between the maximum available voltage modulus (neglecting resistive voltage losses) and the electromotive force is defined as the voltage reserve

$$u_{\text{res}} = |u_s| - |e_s| = |u_s| - \omega |\psi_s| \quad (1.15)$$

The stator voltage modulus  $|u_s|$  depends on the intermediate circuit DC voltage level, and the flux linkage modulus  $|\psi_s|$  is regulated by the control system. In the field weakening range, only a small voltage reserve is available, and thus the drive dynamics are reduced (Pyrhönen, 1998). Depending on the drive type, the field weakening point is roughly the point at which the output voltage equals 90–100 % of the input voltage of the frequency converter. The voltage reserve can be selected, and it can be different in different frequency converters. Lowering the field weakening point speed gives more voltage reserve to react in dynamical situations. This means that the voltage capability of the converter is not used in full in the continuous state, which leads to larger currents and losses. In the field weakening range, torque capability of the motor is reduced as the frequency increases, because the torque produced by the motor is proportional to the magnetic flux.

Fig 1.6 illustrates the principles of the constant flux region and the field weakening region in an induction motor drive where the maximum torque decreases substantially in the field weakening range. The field weakening starts when the voltage reserve defined above reaches its minimum value as the speed increases.

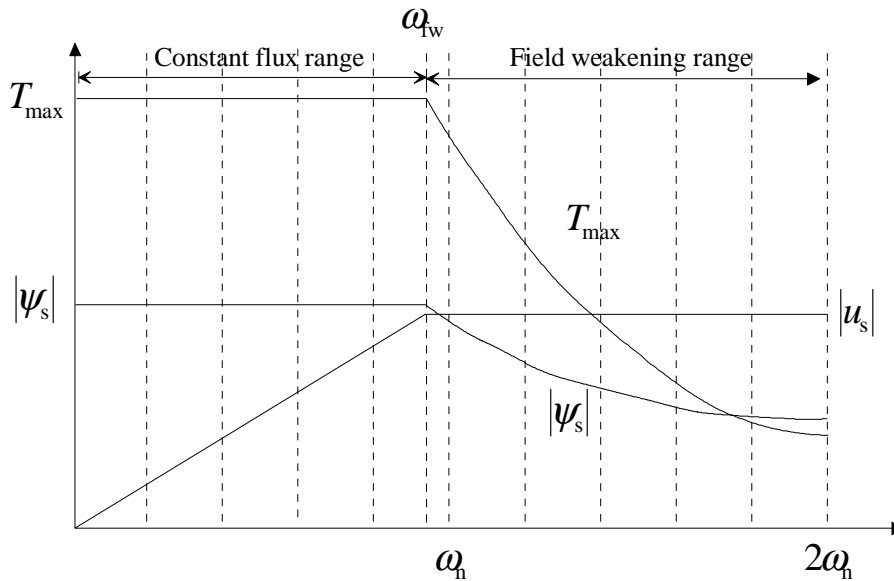


Fig 1.6. Induction motor characteristics and capabilities. Torque is proportional to the square of the air gap flux and in the field weakening, where the flux is inversely proportional to the speed and the maximum torque decreases inversely proportional to the speed squared.

### Motor nominal frequency and frequency converter

Typically, general-purpose induction motors have rated values at 50 Hz (or 60 Hz) supply frequency on the rating plate. The 50 Hz (or 60 Hz) point is not necessarily a normal operation point for a VSD at least if the motor is designed for 50 Hz and 400 V or 690 V. When using a 50 Hz, 400 V machine in a VSD, the 50 Hz operation requires either overmodulation or it is located in the field weakening range. When using a diode bridge supply, the theoretical value of the intermediate circuit DC voltage is about 1.35 times the line-to-line voltage  $U_{LL}$ . Thus, the maximum available phase voltage without overmodulation is 0.956 p.u. If a linear  $U/f$  relationship and a rated flux are used, the field weakening starts at the frequency of 48 Hz. The field weakening point depends on the terminal voltage of the frequency converter, the supply voltage and the cable length. The field weakening point is also affected by the voltage losses in the frequency converter, especially in the rectification of the network voltage and filtering of the DC voltage. In practice, using AC chokes in front of the diode rectifier results in a lower DC link voltage than using a DC choke in the DC link itself for filtering the converter input. With an active rectifier, the voltage can be controlled actively and a certain DC voltage level can be maintained independently of the network voltage level or fluctuations.

### 1.5 Control methods

A popular AC drive configuration uses a VSI employing PWM techniques to synthesize the AC waveform as a train of variable-width DC pulses. The inverter uses either IGBTs, IGCTs, gate turnoff thyristors, MOSFETs or bipolar power transistors for the purpose. Currently, the VSI PWM drive offers the best energy efficiency over a wide speed range for drives up to 5–30 MW. Another advantage of PWM drives is that, unlike other types of drives, it is not necessary to vary the rectifier output voltage to control the motor speed (Dugan et al., 2002).

### 1.5.1 Coordinate transformation and reference frames

The transformation from phase quantities to two-axis quantities ( $\alpha\beta$ -frame) can be written as

$$\begin{bmatrix} X_\alpha \\ X_\beta \\ X_0 \end{bmatrix} = \frac{2}{3} \begin{bmatrix} \cos \theta & \cos\left(\theta - \frac{2\pi}{3}\right) & \cos\left(\theta + \frac{2\pi}{3}\right) \\ \sin \theta & \sin\left(\theta - \frac{2\pi}{3}\right) & \sin\left(\theta + \frac{2\pi}{3}\right) \\ \frac{1}{2} & \frac{1}{2} & \frac{1}{2} \end{bmatrix} \begin{bmatrix} X_U \\ X_V \\ X_W \end{bmatrix} \quad (1.16)$$

and the inverse transformation is

$$\begin{bmatrix} X_U \\ X_V \\ X_W \end{bmatrix} = \begin{bmatrix} \cos \theta & \sin \theta & 1 \\ \cos\left(\theta - \frac{2\pi}{3}\right) & \sin\left(\theta - \frac{2\pi}{3}\right) & 1 \\ \cos\left(\theta + \frac{2\pi}{3}\right) & \sin\left(\theta + \frac{2\pi}{3}\right) & 1 \end{bmatrix} \begin{bmatrix} X_\alpha \\ X_\beta \\ X_0 \end{bmatrix}, \quad (1.17)$$

In the simulation or implementation of vector-controlled drives there is usually a need to switch from one coordinate system to another. The coordination transform from the  $xy$ -frame to the rotating reference frame ( $d$ - $q$ -axis) travelling with a speed  $\omega$

$$x_d = x_\alpha \cos(\omega t) + x_\beta \sin(\omega t) \quad (1.18)$$

$$x_q = -x_\alpha \sin(\omega t) + x_\beta \cos(\omega t) \quad (1.19)$$

In the Fig. 1.7 is presented the typical representation of the signals in electrical engineering.

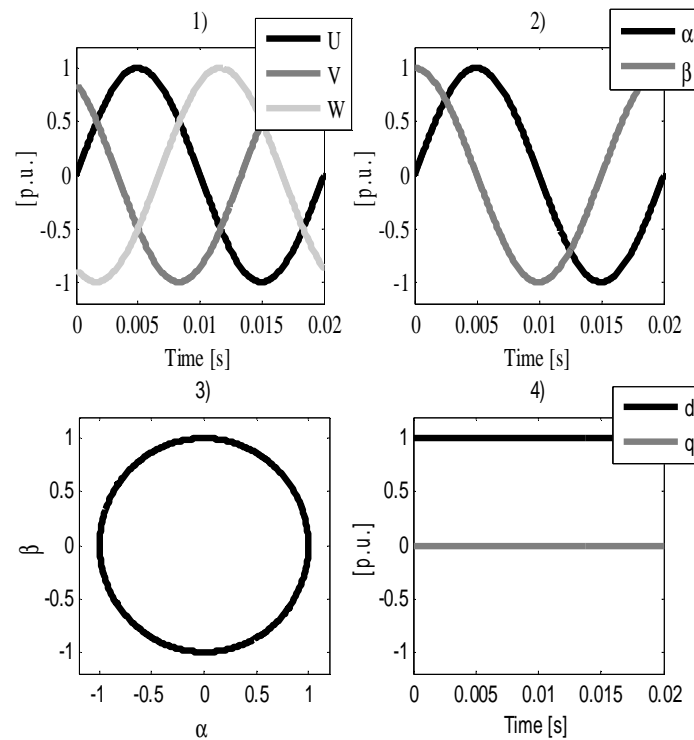


Fig 1.7. Typical representation of the signals in electrical engineering. 1. Balanced three-phase quantities with a  $2\pi/3$  phase shift. 2. Two-axis components as a function of time. 3. Two-axis components in the stator reference frame. 4. Rotor coordinates (or rotor flux coordinates) or synchronously rotating coordinates).

## 1.5.2 DTC

Direct torque control (DTC) was proposed for AC drives by Depenbrock and Takahashi in the 1980s (Depenbrock 1988), (Noguchi and Takahashi 1986). The DTC has advantages of high torque response, simple design and robustness against parameter variations. The variable switching frequency and high torque ripple are drawbacks of the classical DTC. Direct torque control has been a topic of numerous scientific works over the past two decades; the switching frequency of the DTC is analysed by Casadei et al. (1999), Kang and Sul (2001) and Salem and Masmoudi (2007). Numerous improvements in the classical DTC have been proposed for instance by Kang and Sul (1999), Idris and Yatin (2000, 2003) and Lascu et al. (2000, 2004).

The main principle of the DTC is to control the torque and the modulus of the stator flux linkage directly by controlling the inverter switches using the outputs of the hysteresis comparators and selecting the correct voltage vector from the optimal switching table (Pohjalainen et al. 1994). The estimate of the stator flux linkage is calculated with the integral

$$\psi_{s,\text{est}} = \int (\mathbf{u}_s - r_s \mathbf{i}_s) dt, \quad (1.20)$$

and the estimate of electric torque is calculated from the estimated flux linkage components and the measured stator currents in the two-axis stationary reference frame

$$T_{e,\text{est}} = \frac{3}{2} p (\psi_{sa} i_{s\beta} - \psi_{s\beta} i_{sa}). \quad (1.21)$$

In the DTC there is no fixed switching frequency but the average switching frequency is controlled with flux linkage and torque hysteresis bands. The hysteresis bands are controlled by the reference switching frequency to achieve the desired average value. In the DTC, there is no predetermined switching pattern either, and the frequency component content of the voltages is not known beforehand.

The difference between standard PWM methods and the DTC lies in the switching mode; in the classical PWM, the switching follows a sequential pattern, while in the DTC method, the switching is controlled by torque and flux errors. As a result, the DTC method should ensure simultaneous minimization of both the pulsation and switching frequency. The above features are necessary to improve not only the technical properties of the drive (i.e. decrease of speed pulsation) but also its economic characteristics, as the switching frequency influences the power losses, and hence, the inverter efficiency, Fig 1.8.

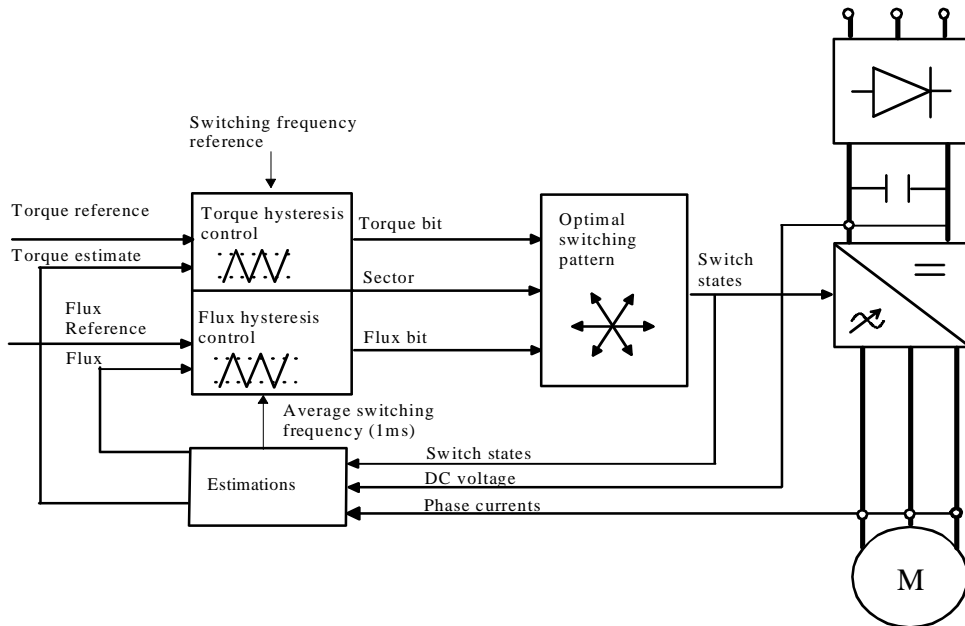


Fig 1.8. DTC drive construction.

### 1.5.3 Vector control – symmetrical two-phase modulation

The two-phase space vector modulation represents one type of discontinuous pulse width modulation technique. To avoid unnecessary switchings and to improve the converter efficiency, one of the three phases is clamped by 60 degrees either to the lower or upper DC bus, and only two phases are switched. The two-phase SVM provides a 33 % reduction in the effective switching frequency and switching losses compared with the standard SV-PWM. The modulation method has a high current harmonic content at a low modulation index. The principle of voltage vector selections in symmetrical two-phase modulation is illustrated in Fig 1.9.

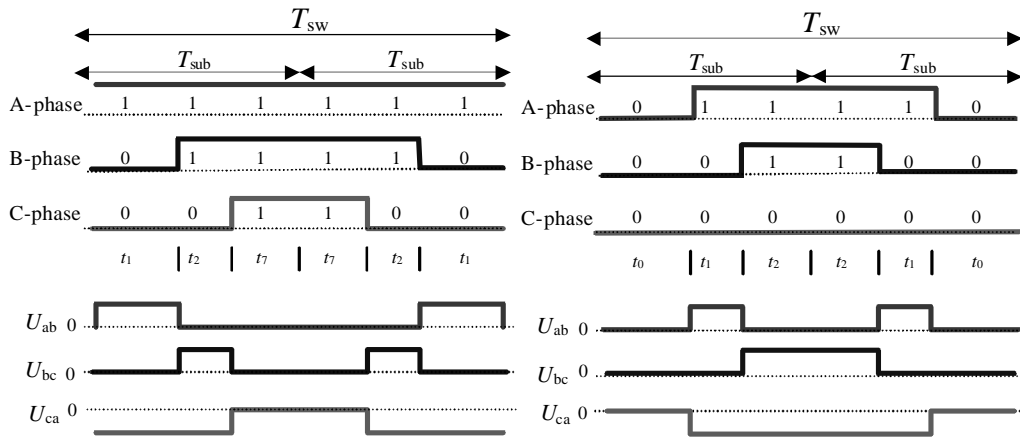


Fig 1.10. Generation of voltage vectors in the switching sequence of the symmetrical two-phase modulation and the respective switching durations in sectors I and II.

#### Per unit values

Per unit values are widely used in electrical engineering, and they are also used in this thesis. They are a valuable tool in the control system design, implementation and simulations. In general, the per unit value is the ratio of the actual and base value of the same quantity

$$\text{per unit value} = \frac{\text{actual value}}{\text{base value}} \quad (1.22)$$

The base values are related to the nominal values of the apparatus. When power electronics is considered, the base value for current is the peak value of the nominal phase current fundamental

$$I_b = \hat{I}_n = \sqrt{2}I_n, \quad (1.23)$$

where  $I_n$  is the RMS value of the nominal sinusoidal phase current. Correspondingly, the base value for the voltage is the peak value of the nominal phase voltage

$$U_b = \hat{U}_{\text{phase}} = \sqrt{\frac{2}{3}}U_{LL}, \quad (1.24)$$

where  $U_{LL}$  is the RMS value of the nominal line-to-line voltage. The base value for angular frequency is

$$\omega_b = 2\pi f_n, \quad (1.25)$$

where  $f_n$  is the nominal frequency. With these three base values, it is possible to derive other base values required in electrical engineering.

Impedance is written as

$$Z_b = \frac{U_b}{I_b}. \quad (1.26)$$

All base values are only magnitudes. They are not associated with any rotational angle. The per unit values, however, are space vectors. The phase angles of the currents and voltages and the power factor of the circuit are not affected by the conversion to per unit values. It is important to note that also the physical time  $t$  has per unit scaling. If physical time is used in the per-unit-valued equations instead of per unit time  $\tau_{pu}$ , it has to be multiplied with the base value of the angular frequency. This is common in simulation models and control systems. The time base value is defined as

$$\tau_b = \frac{1}{\omega_b}. \quad (1.27)$$

For example the integral equation (1.20) in per unit values is

$$\psi_{s,est} = (\mathbf{u}_s - r_s \mathbf{i}_s) \omega_b t, \quad (1.28)$$

where flux linkage, voltage, current and resistance are per unit values and time  $t$  is real time.

## 1.6 Simulation

When modelling electromagnetic devices, it is beneficial to solve the magnetic and electric equations simultaneously. In this work, an approach is taken to simulate the control system and the electromagnetic properties of a frequency converter simultaneously supplying an electric motor. Here, a 2D FEM simulation tool FCSMEK is combined with a C-language-based circuit simulator. The losses of the electric devices in different parts of an electric drive can be modelled accurately by various independent software, such as electric circuit simulators and finite element method design and analysis software. Problems with software of this kind may arise from a vast or very specific need for parameters and a typically long calculation time, if a high accuracy of results is required. The parameters needed in the calculation can be difficult to determine. Furthermore, several software codes may be required to calculate the losses of different parts of the frequency converter system; for instance, FEM software for the inductor, and yet another software, that is, a circuit simulator, for the diode bridge, and so on. Both the converter and the motor produce specific harmonics that interact with each other, and the harmonics produced by the converter depend essentially on the control system.

Different modulation methods of the PWM converter influence the conduction and switching losses of the inverter. Thus, there arises a need for the coupled simulation of the circuit simulator, the finite element method and the control algorithm. Moreover, the parameters needed for simulation and loss calculation are desired to be defined with reasonable effort.

### **Benefits of simulation**

Over the last decade, several papers have been published to combine the magnetic fields with electric circuit equations in machine modelling. In a motor design process, the FEM is the state-of-the-art method, and in a design process, it is the last step before prototype construction. A reliable and reasonably accurate loss model for an induction motor and converter system is very important for the performance prediction of variable speed drives.

Two-dimensional programs based on the finite element method have turned out to be effective tools when analysing new constructions of electrical machines. Usually, the terminal voltages or the currents can be treated as given quantities within the finite element analysis. Although in many types of electrical drives, this assumption is reasonable, there still remain a variety of cases where the properties of the machine significantly affect the behaviour of the external circuit.

The design of an electrical machine and an electric drive is an iterative process. To reduce the costs and development time, prototyping can, to a large degree, be replaced by simulations.

### **C-language simulator**

The C-language-based converter model combined with the FEM machine model tops the commonly used approaches such as PSPICE or the MATLAB/SIMULINK-based converter model. The C-language based-model provides advantages in transparency, controllability and simulation efficiency. Moreover, the use of a C-language platform is not restricted by any licence fees.

The C-language approach provides an option to save, modify and examine all parameters. Furthermore, options to add on new features and the expandability of the simulator are almost unlimited. The C-language is a natural choice to emulate the behaviour of the control system of commercial devices as closely as possible, because the modern frequency converter control systems in commercial products are implemented in the C-language (or together with an assembly language).

The C-language approach outperforms more user-friendly approaches such as PSPICE or MATLAB/SIMULINK in calculation time. The complete control system simulation coupled with a simple frequency converter model and an analytical motor model in simulation software such as PSPICE or SIMULINK are somewhat slow. To improve the calculation speed and to reduce the massive computational burden that is unavoidable when applying the FEA, the C-language software includes here a model for the complete control system and the frequency converter as well as its loss models. It is shown in this thesis that to reach good overall simulation results of the drive system and its energy efficiency, it is sufficient to use relatively simple loss models for frequency converter components and assign the computational capacity to the motor calculation.

## 1.7 Scope of the work and outline of the thesis

This research focuses on the energy efficiency of controlled induction motor drives. The ultimate objective behind this study is to calculate the drive system losses and efficiency with a reasonable accuracy and to select the best available frequency converter control for a specific motor, and vice versa, to find the most functional and energy efficient alternative. From the VSD manufacturer's point of view, such a simulation tool will be extremely important in the future when new efficiency standards will be issued for VSDs. The manufacturers must be capable of giving accurate information about their converter efficiencies at different operating points. As measurements are extremely time consuming, there is a need to reduce their amount and use simulation tools at least in the interpolation of operating points.

Development, programming and testing of the software simulator constitute the core of this research work. The simulator under development can be used to analyse the losses of the frequency converter and the motor with a closed-loop control system.

Many of the electric drive losses depend on the square of the current. Frequency and flux density levels are other important factors when evaluating the losses of the drive. To calculate losses accurately, the current and flux distributions in the frequency domain have to be correct. Although the operating temperatures of the motor and semiconductor devices have an effect on the motor losses, in this thesis the temperature is assumed to be constant. The reason for this is that in this doctoral thesis, the simulation software is used to analyse only the steady-state performance, losses and efficiencies of frequency-converter-controlled induction motors applying a time-stepping finite element model. The simulation tool can be used as part of a loss-optimized design of the converter machine system.

Simulation tools cannot replace the need for laboratory measurements, neither can they be as accurate as measurements; nevertheless, simulations can essentially reduce the need for measurements. In high-efficiency systems, the loss measurements are also very challenging, especially if only direct electrical measurements are used. Often only Joule-metric measurements give accurate enough results for the losses. Such an approach is, however, very time consuming and is not suitable for dynamic loss measurements.

The doctoral thesis answers to the simulation questions: which is the sufficiently small time step for time-stepping simulation, and what is the calculation time for different time steps.

The current output approach is shown to be suitable for simulating electrical machines with frequency converters; this has been validated by experimental results by Kanerva (2005).

Below, the contents of the chapters are introduced in brief:

**Chapter 1** gives an introduction to the topic.

**Chapter 2** introduces harmonics and harmonic analysis methods. In rotating AC machines, some harmonics are always present. The chapter gives basic information of the harmonic analysis and sources of harmonics. The effects of harmonics on the rotating machines are discussed. The definition of Discrete Fourier Transform (DFT) is presented, and it is explained how it is used in this doctoral thesis.

**Chapter 3** focuses on the drive system losses. The converter and machine loss mechanisms are presented. The principles of loss models used in this thesis are given. The chapter also includes some aspects of extra losses produced by the PWM method in the motor.

**Chapter 4** introduces the simulation models used in the analysis. The simulation model of the frequency converter is presented together with some of the converters nonidealities. The analytical motor model and the FEM program used in the analysis are described. Further, the models of control systems are summarized in brief.

**Chapter 5** concentrates on practical measurements and simulations. The current spectra of the DTC are analysed analytically and by simulations. The effect of the current measurement delay on the spectrum is presented. The measured and simulated spectrum is compared using two drive combinations.

**Chapter 6** introduces the results of the temperature rise tests and the motor, converter and drive loss measurements. The calculation accuracy of losses is examined using various operating points with a 37 kW induction motor drive system.

**Chapter 7** includes conclusions and summarizes the most relevant results. The chapter also introduces ideas for further simulator development and scientific work.

## 1.8 Scientific contributions of the doctoral thesis

A drive system simulation tool has been developed in order to be capable of accurately analyse the energy efficiency of power-electronics-controlled induction motor drives. The tool is based on a combination of a circuit simulator, control system software that emulates the behaviour of commercial DTC- and vector-controlled PWM drives and a FCSMEK FEM tool, developed originally by the Laboratory of Electromechanics of Helsinki University of Technology and ABB. An important target was to find an accurate division of the electric and magnetic losses in the drive. Verification of the simulation tools has been carried out with laboratory tests. The simulation tool results have been analysed and compared with the measurements.

The PWM converter simulation tool proved accurate, and the results support the earlier studies (e.g. Kanerva 2005) where it is stated that the current output approach coupling method between the circuit simulator and the FEM motor model should be valid for the simulation of electric drives. Here, the comparison between the simulated results and the measurements showed that the FEM tool may effectively be used in the simulations with a reasonable accuracy.

Because of the chaotic nature of the DTC, its accurate simulation was shown to be a very demanding task. In the DTC simulation, however, the most difficult problem was to tune the simulation tool to be capable of accurately producing similar current spectra compared with the actual drive tests. Reasons for the initial discrepancy between the simulated current spectra and the actual current spectra were sought and given in this work.

The time step length in the time-stepping analysis of the converter-fed induction machine was studied, and no significant changes were observed in the accuracy of the current spectra. It was, however, observed that the loss analysis is slightly dependent on the length of the time step.

Different nonidealities of the actual hardware and their effects on the simulation results were studied. For example, the current measurement delay in the digital signal chain was shown to be an important factor in the simulation. In the simulations, the effects of artificial current measurement delays were studied. In some cases, adjusting the delay resulted in correct current spectra.

The effect of the hysteresis control in the DTC was also studied. The hysteresis control was shown to be an important factor from the current spectrum point of view.

An in-depth analysis of an induction motor drive at the 50 Hz operation point showed that the theoretical value of the converter switching frequency is not valid near the field weakening or overmodulation area. An analysis method, independent of the modulation pattern, was developed to determine the switching frequency of the converter from the measured three-phase voltages.

Further studies on the converter digital hardware and its properties showed that the delays used in the simulations are in the correct delay range of the digital electronics. An in-depth analysis of the digital hardware was, however, beyond the scope of this thesis.

The energy efficiency of the drive system and its loss distribution were analysed with the drive simulator, and the simulator accuracy was verified by measurements. It was also shown that within the measurement accuracy, the tool can be used in the evaluation of the energy efficiency of electrical drives.

The most relevant publications related to this thesis are:

1. Aarniovuori L., Laurila, L., Niemelä, M. and Pyrhönen, J. (2007), "Loss Calculation of a Frequency Converter with a Fixed-Step Circuit Simulator," In *the 12th European Conference on Power Electronics and Applications (EPE)*, Aalborg, Denmark.
2. Aarniovuori L., Laurila, L., Niemelä, M. and Pyrhönen, J. (2008), "Comparison of the Induction Motor Simulation Models – Analytical and FEM – in Drive System Controlled with Direct Torque Control," In *the 19th International Symposium on Power Electronics, Electrical Drives, Automation and Motion (SPEEDAM)*, Ischia, Italy.
3. Aarniovuori L., Laurila, L., Niemelä, M. and Pyrhönen, J. (2008), "Switching Frequency Harmonics of DTC IM Drive in a System Simulator with Analytical and FEM Motor Model," In *the 18th International Conference on Electrical Machines (ICEM)*, Vilamoura, Algarve, Portugal.
4. Aarniovuori L., Laurila, L., Niemelä, M. and Pyrhönen, J. (2009), "Comparison of Induction Motor FEM simulations fed by measured and reconstructed DTC inverter voltages," In *the 13th European Conference on Power Electronics and Applications (EPE)*, Barcelona, Spain.

5. Aarniovuori L., Laurila, L., Niemelä, M. and Pyrhönen, J. (2010), "DTC IM Drive Losses – Simulation and Measurements," In *the 19th International Conference on Electrical Machines (ICEM)*, Rome, Italy.

This doctoral thesis provides an extended approach to the issues addressed in the above publications. This thesis adds knowledge to the field of simulation of electrical machines and provides deeper understanding of variable speed drive operation. The topic of publication 1, frequency converter loss calculation, is discussed in more detail in Chapters 3 and 4. An extended analysis of the topics of Publications 2 and 3 is given Chapter 5. The results of Publication 4 show that inverter switch states can be solved from measured three phase voltages reliable; this is discussed in Chapter 5. The topic of Publication 5 is extended to the symmetrical two-phase modulation in Chapter 6. The contents of these publications are produced and written by the author. The co-authors have participated in the preparation of these publications by revision comments and suggestions.

## 2 HARMONICS AND HARMONIC ANALYSIS METHODS

### 2.1 Harmonic analysis

Harmonic analysis is a process of calculating the magnitudes and phases of the fundamental and higher-order harmonics of a periodic waveform. The resulting series, known as the Fourier series, establishes a relationship between the time domain function and the same function in the frequency domain.

In practice, data are often available in the form of a sampled time function, represented by a time series of amplitudes, separated by fixed time intervals of limited duration. When dealing with such data, a modification of the Fourier transform, the Discrete Fourier Transform, is used (Arrillaga and Watson, 2003).

### 2.2 Harmonic sources

When a source of sinusoidal voltage is applied to a nonlinear device or load, the resulting current is not perfectly sinusoidal. In the presence of system impedance this current causes a non-sinusoidal voltage drop and, therefore, produces voltage distortion at the load terminals, in other words, the latter contains harmonics. Harmonics in the rotating electrical machines are produced by the current linkage distribution of poly-phase AC windings and the slotting of the machine.

The winding of the induction machine is divided into the stator slots and cannot be spread smoothly over the stator inner surface. A multi-phase stator winding produces spatial harmonics of odd number in the air gap (Heller, 1977)

$$v = 2m_s k_s + 1, \quad k_s = 0, \pm 1, \pm 2, \pm 3, \dots$$

where  $m_s$  is the number of phases. In the case of a three-phase winding, the harmonic orders are  $v = 1, -5, +7, -11, +13, \dots$

The stator slotting causes permeance harmonics, the orders of which are

$$v_{\text{slot}} = 2m_s q_s k_{\text{slot}} + 1, \quad k_{\text{slot}} = 0, \pm 1, \pm 2, \pm 3, \dots$$

where  $q_s$  is the number of slots per pole and phase. These nonidealities in the motor also result in non-sinusoidal stator currents even in a case where the supply is sinusoidal. Fig 2.1 illustrates as an example the measured stator current harmonic amplitudes of a 37 kW induction motor in per cent of the fundamental wave current amplitude when the load torque is 92 % of the nominal load. It must be, of course, remembered that the supply voltage is not purely sinusoidal and phase symmetric.

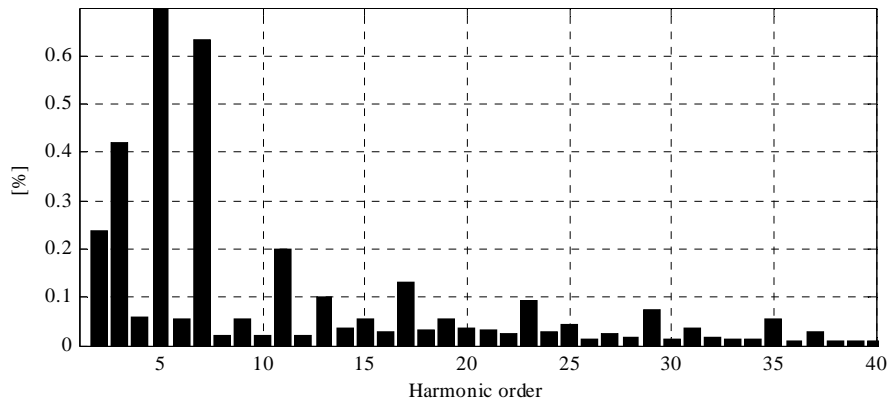


Fig 2.1. Measured stator phase current harmonic amplitudes of a 37 kW induction motor supplied from the grid. The 5<sup>th</sup> current harmonic amplitude is scaled outside the figure and the amplitude of the 5<sup>th</sup> harmonic component is 1.87 %.

In Fig 2.1 the most significant stator current harmonic component is the 5<sup>th</sup> harmonic. Other harmonic components caused by the distributed windings (7<sup>th</sup>, 11<sup>th</sup>, 13<sup>th</sup>, 17<sup>th</sup>...) are also clearly visible. The first permeance harmonics pair for this machine ( $m_s=3$ ,  $q_s=4$ ) should give a rise to harmonics of the order 23 and 25. In addition to the spatial harmonics caused by the distributed winding system and permeance harmonics, also time harmonics caused by the PWM supply are possible. Analytical derivation of the harmonics produced by different PWM methods can be found for instance in Holmes and Lipo (2003).

### 2.3 Effects of harmonics on rotating machines

Non-sinusoidal voltages applied to electrical machines may cause overheating. Motors are not normally derated as long as the harmonic distortion remains within 5 % normally recommended by regulations (Arrillaga and Watson, 2003). Above that limit the motors often experience excessive heating problems. On the positive side, motors contribute to the damping of the system harmonic content by the virtue of the relatively high  $L/R$  ratio of their blocked rotor circuit.

Harmonic voltages of currents give rise to additional losses in the stator windings, rotor circuits and rotor laminations. The losses in the stator and rotor conductors are greater than those associated with the DC resistances because of the eddy currents and skin effect.

Leakage fields set up by harmonic currents in the stator and rotor end windings produce extra losses. In the case of induction motors with skew rotors, the flux changes in both the stator and the rotor, and a high frequency can produce substantial iron loss. The magnitude of this loss depends on the amount of skew and the iron loss characteristics of the laminations.

Extra power loss is probably the most serious effect of harmonics on AC machines. The capability of a machine to withstand extra harmonic currents depends on the total additional loss and its effect on the overall machine temperature rise and local overheating. A cage-induction motor tolerates higher rotor losses and temperatures provided that these do not result in unacceptable stator temperatures, whereas machines with insulated rotor windings may be more limited with this respect.

Harmonic currents present in the stator of an AC machine produce harmonic torques. All positive-sequence harmonics develop shaft torques thereby assisting shaft rotation, whereas negative-sequence harmonic components have an opposite effect. Because the slip to harmonic frequencies is almost unity, the torques produced by harmonic currents are very small, and moreover, the small torques occur in pairs, which tend to cancel each other. The effects of harmonics on the mean torque can, in most cases, be neglected. Although harmonics have little effect on the mean torque, they can produce significant torque pulsations.

The stray capacitances in converter-fed electric motors in the presence of harmonics cause capacitive currents to flow through the motor bearings and are often a reason for their failure. Harmonic components are also the major cause of sound in electrical machines. Motors powered with pulse width modulation exhibit their predominant sound levels at the modulating frequency. The level of sound is not a function of load, but is inversely proportional to the motor speed (Arrillaga and Watson, 2003).

## 2.4 Discrete Fourier Transformation (DFT)

The discrete Fourier transform is a specific kind of Fourier transform, used in the Fourier analysis. It transforms the function in the time domain to the frequency domain representation. The DFT can be used to functions that are discrete. The discrete function can be created by sampling of a continuous signal, such as current or voltage. The mathematical derivation of Fourier series can be found for instance in Kreyzig (1993), Proakis and Manolakis (1996) and Arrillaga and Watson (2003) and it is not in the scope of this thesis.

The discrete form of the Fourier transformation is most suited for time-dependent data analysis. The discrete Fourier transformation is defined as

$$X(f_k) = \frac{1}{N} \sum_{n=0}^{N-1} x(t_n) e^{-j2\pi kn/N}, \quad (2.1)$$

where  $N$  is the number of samples,  $t_n$  represents the  $N$  samples of the function in the time domain and  $f_k$  represents the  $k$  points in the frequency domain.

In the DFT, the number of samples determines the maximum number of frequency components that can be calculated. If  $N$  samples have been taken during time  $T$ , it is possible to calculate the DC component and  $N/2$  frequency components. This means also that the signal to be sampled should not have frequency components that have a higher frequency than  $N/(2 \times T)$ . The frequencies above this limit must be filtered before the DFT analysis is performed. If no filtering is done, the calculated frequency components have an error that depends on the magnitudes of the frequency components above  $N/(2 \times T)$ . This error is commonly called aliasing. This is an interpretation of the sampling theorem, which states that the sampling of the frequency component must be at least twice the highest frequency contained in the original signal for a correct transfer of the information to the sampled system.

In the DFT, different windowing functions can be used. The application of the window function has the effect of multiplying each point of a time domain signal by the corresponding time point of the window function. The spectral leakage can be reduced by changing the form of the window function. In the literature, various window functions are presented; for example, rectangular, triangular, cosine squared (Hanning), Hamming, Gaussian, Dolphy-Chebyshev, Kaiser-Bessel and Flat-Top. The rectangular window function, defined by

$$W(t) = \begin{cases} 1 & \text{for } -T/2 < t < T/2 \\ 0 & \text{otherwise} \end{cases} \quad (2.2)$$

has a noise effective bandwidth of  $1/T$ , where  $T$  is the window length: the side lobe levels are large (-13 dB from the main lobe for the first side lobe), and their rate of decay with frequency is low (20 dB per decade). This means that when evaluating the fundamental component of a signal, interfering spectral components close to it will be weighted heavily, contributing greater interference to the fundamental component than for the other windows. A rectangular window ideally results in zero spectral leakage and high spectral resolution when the duration of the rectangular window is equal to an integer multiple of the period of a periodic signal. This frequency matching gives the greatest resolution of the periodic frequency (Arrillaga and Watson). In this thesis, the frequency matching with a rectangular window is used.

In addition, the phase angles of the frequency components are filtered in the frequency domain when other than the box window is used. The phase information for other than rectangular window can be used only to check mutual phase differences between two signals because the windowing alters the phase shifts (Niiranen, 2001).

## 2.5 Harmonic distortion

The visual examination of the signal spectrum is one way to determine the harmonic content of the signal, although it is not very practical if multiple signals have to be analysed. In the literature, various different indices for distortion of the signals have been presented, for example a Total Distortion Factor (TDF) and a Total Demand Distortion (TDD). The most commonly used one in electrical engineering is the total harmonic distortion (THD)

$$\text{THD}_H = \frac{\sqrt{\sum_{k=2}^{k=H} I_k^2}}{I_1} \cdot 100\% , \quad (2.3)$$

where  $I_1$  is the fundamental current RMS value and  $I_k$  is the RMS current value of the harmonic component. The THD is calculated up to the harmonic component  $H$ . The widely used standards provided by IEC and IEEE give different values for  $H$ ; the IEC uses 40 harmonic components instead of IEEE's 50 components (IEEE, 1992). In this thesis, 50 harmonic components are used, when the THD is calculated. Total harmonic distortion identifies the amount of unwanted harmonic frequencies in proportion to the fundamental wave. In frequency converter applications, the switching-frequency-caused phenomena are not necessarily harmonic frequencies at all. Hence, in this kind of an analysis, the total distortion (TD) can be used to describe the signal quality. Here, the TD is defined as

$$\text{TD}_{20000} = \frac{\sqrt{\sum_{k=2}^{k=20000} I_k^2}}{I_1} \cdot 100\% . \quad (2.4)$$

The upper limit of the frequency component that was included in the analysis in this thesis was chosen to be 20 kHz, and thus, the first multiple of the 8 kHz carrier frequency can be taken into account. Consequently, the TD value includes all harmonic, subharmonic and interharmonic components from 1 Hz to 20 kHz with a 1 Hz resolution. This value should give more information about the current distortion level in the variable speed drives than the THD,

where only harmonic current components are calculated. As an example, two motor phase current waveforms are shown in Fig 2.2.

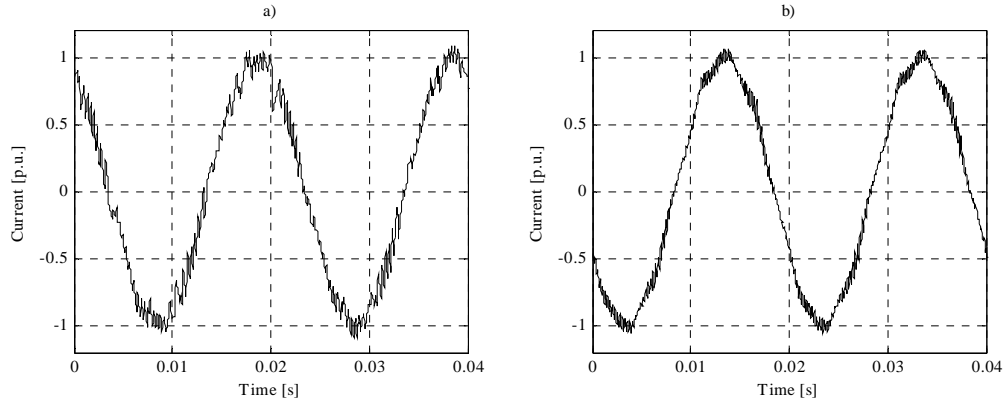


Fig 2.2. Motor phase current waveforms. The frequency reference is 50 Hz and the load is equal to 92 per cent of the nominal load. a) DTC converter with a 1 kHz switching frequency. b) Vector converter with a 4 kHz carrier frequency.

The time domain presentation of the measured motor phase currents in Fig 2.2 shows that the waveform **a** is more distorted than the waveform **b** and it has lower frequency harmonic components than the waveform **b**. In **b** there are some low-frequency harmonic components, and in addition, a high-frequency component. The same information can be examined more precisely in Fig 2.3, where the results of the DFT of the phase currents are presented.

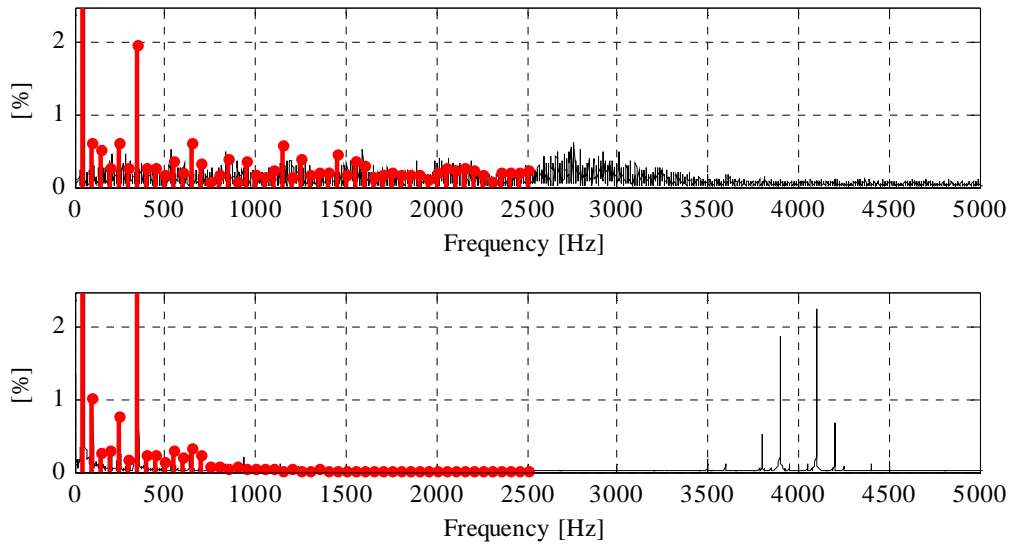


Fig 2.3. Frequency domain presentation of two motor phase currents. The upper one is the waveform **a** and the lower one is the waveform **b**. The red dots indicate the amplitudes of 50 harmonic components. The amplitude of the 7<sup>th</sup> harmonic component is 3.1 %, which is scaled outside the figure.

Fig 2.3 shows that in the DTC at this operating point there is no clear switching frequency in the current spectrum, but a carrier frequency of 4 kHz in the symmetrical two-phase modulation is clearly visible. In the symmetrical two-phase modulation there are also multiples of the

carrier frequency near 8, 12, 16 kHz and so on, which are not shown in the figure. The figure also shows that the THD value does not take into account the current harmonic components in the switching frequency range. The frequency band is even narrower when smaller frequency references are used. The THD values of the signals using 50 first harmonic components are 2.57 % for the DTC converter and 3.44 % for the vector converter. These THD values could result in a misleading assumption that with a 4 kHz carrier frequency the current of the vector converter is more distorted and thus the motor temperature rise is higher than in the case of the DTC converter with a 1 kHz switching frequency. Nevertheless, the temperature rise tests in Chapter 6 show that this assumption is incorrect. The TD values of the currents using Equation (2.4) are 10.25 % for the DTC converter and 7.61 % for the vector converter, which indicates same results as the temperature rise test. The RMS value of the equally sampled current is

$$I_{\text{RMS}} = \sqrt{\frac{1}{N} \sum_{k=0}^N i(t_k)^2}, \quad (2.5)$$

where  $N$  is the number of samples at time instants  $t_k$ . The RMS value of the AC current is equal to the DC current that dissipates the same amount of energy in the resistance. There is a relationship between the THD and the RMS, that is (Holmes and Lipo, 2003),

$$I_{\text{RMS}} = I_{1,\text{RMS}} \sqrt{1 + \text{THD}^2}, \quad (2.6)$$

where  $I_1$  is the fundamental wave component RMS value. For previous current waveforms, the RMS values obtained by Equation (2.5) are a) 68.0 A and b) 68.8 A. If Equation (2.6) is used, the RMS values are a) 67.6 and 68.5 A. If the TD value is used instead of the THD value in (2.6), the RMS values are 68.0 A and 68.8 A. This shows that the TD value gives more information about the current distortion than the THD value.

### 3 LOSSES

A short description of the loss mechanisms in different parts of the drive system is given in the following. Some details of the converter and motor loss mechanisms are discussed, and loss calculation methods included in the simulator used in this thesis are introduced.

#### 3.1 Converter losses

Power electronic converters are used to produce a variable-frequency supply to AC motors, thereby enabling variable-speed operations. Power converters have conduction and switching losses in the power devices and losses in the passive components and the auxiliary cooling systems. The loss is a function of device type, switching frequency, voltage and current level temperature, but in industrial systems, the converter has a typical full-load efficiency, which rises with the power rating from around 80 % below 1 kW to over 97 % at 150 kW (Rooks and Wallace 2004). However, the efficiency levels are rising as new, low-loss, faster-switching devices enter the market. Frequency converters generally have a high level of energy efficiency. For the most common industrial converter type, a low-voltage indirect frequency converter of the voltage source type with an uncontrolled three-phase diode rectifier as line-side converter, IEC (2009) gives the frequency converter loss distribution shown in Table 3.1.

Table 3.1. Typical percentage of losses for passive front-end converters (IEC 2009).

		[%]
Line-rectifier		20–25
Output stage	Switching losses	30–50
	Forward losses	15–20
Internal control circuit		5–20

The factors affecting these losses can be summarized as follows: Line rectifier (including filter) losses are proportional to the line-current. The output stage (IGBT bridge) losses are proportional to the motor current, and in addition, the switching frequency is affecting the switching losses. The internal control circuit losses are nearly constant.

##### 3.1.1 Input inductor losses

The input inductors of the frequency converter dissipate power in their cores and windings. The core losses can be divided into hysteresis losses and eddy current losses (Sousa et al. 1992). Although the exact calculation of these losses can be complicated and difficult, they can be estimated using data sheet parameters available from magnetic component suppliers or – more reliably – they can be defined by measurements. The input inductor losses and their frequency dependency can be modelled with the lumped parameter model, Cauer or Foster equivalent models (Erickson, 1997). In the analysis and calculation, only the inductance at the nominal point, the DC resistance, and total losses at one load point are known for the input inductor. Therefore, lumped parameters cannot be used, and the losses have to be modelled with a single series resistance-inductance model. The total losses of the input inductor can be calculated simply as

$$P_{\text{choke}}(t) = 3i_L^2(t)ESR_L, \quad (3.1)$$

where  $i_L(t)$  is the instantaneous inductor line current and  $ESR_L$  is the equivalent series resistance.  $ESR_L$  is calculated by using the measured current and losses of the input inductor.

### 3.1.2 Diode bridge losses

The power dissipation of a diode in forward conduction and reverse blocking state can be modelled as a function of forward and reverse leakage currents and forward and reverse voltages. Losses in the blocking state are negligible. During turn-off and turn-on the diodes consume energy – these losses are called the switching losses. For a line frequency diode bridge rectifier, the switching losses can, however, be neglected due to their smallness at a low frequency, and only the conduction losses are considered. The conduction losses of a diode can be modelled as a function of average current flowing through the diode. The parameters needed for calculating the diode bridge losses are the forward voltage drop  $U_F$  and the on-state resistance  $R_F$ . The instantaneous conduction losses of the diode are described simply as (Kolar et al. 1991)

$$P_{\text{diode, on}}(t) = U_F i_{\text{diode}}(t) + R_F i_{\text{diode}}^2(t). \quad (3.2)$$

$R_F$  and  $U_F$  can be read in the manufacturers'  $U$ - $I$  characteristics, where  $R_F$  is the average derivative in the on-state. The diode bridge losses are six times the single diode losses.

### 3.1.3 Intermediate circuit losses

If the modelled device contains a DC line reactor, it is converted to the AC side, and the losses of the DC line reactor are calculated as an AC input inductor. Therefore, the intermediate circuit losses consist of the losses in the capacitor bank and discharge resistors and the intermediate circuit resistance. The total energy loss in a capacitor bank is a function of dielectric losses attributed to the polarizing mechanisms of the electric field on the molecular structure of the dielectric, and ohmic losses from electrodes and termination metals. Dissipative losses of the capacitor can be represented by an equivalent series resistance,  $ESR_C$ . The  $ESR_C$  values or a curve of the frequency dependency of the  $ESR_C$  can be found in manufacturers' datasheets. The number of series and parallel capacitors in the bank has to be taken into account to calculate the capacitor-bank losses correctly. The DC link current consists of a DC component  $I_{DC}$ , harmonics produced by the diode rectifier bridge, and the switching harmonics by the IGBT inverter bridge. The DC voltage produced by a three-phase full-bridge rectifier carries large amount of  $n$  times 6<sup>th</sup> order harmonics. The average capacitor losses  $P_C$  can be written

$$P_C = \sum_n I_{C(6n)}^2 ESR_{C(6n)}, \quad (3.3)$$

where  $I_{C(n)}$  is the RMS value of the  $n^{\text{th}}$  order of the capacitor current and  $ESR_{C(n)}$  is the equivalent series resistance of the capacitor for a particular frequency. The  $ESR$  values for five different harmonic frequencies have been used in the loss model. At a 50 Hz line frequency, these harmonic frequencies are 300, 600, 900, 1200 and 3000 Hz. The lower-frequency  $ESR_C$ -values describes the losses at harmonic currents produced by the rectifier bridge and the highest frequency  $ESR_C$  value describes the losses in the switching frequency range. The resistive losses in the discharge resistor, which is parallel to the capacitor, are

$$P_{\text{discharge}} = \frac{U_C^2}{R_{\text{discharge}}}, \quad (3.4)$$

where  $U_C$  is the capacitor RMS voltage. There are, of course, some conduction losses in the intermediate circuit conductors, but they are neglected in this case. Thus, the total intermediate circuit losses are

$$P_{\text{DC-link}} = P_C + P_{\text{discharge}}. \quad (3.5)$$

### 3.1.4 IGBT module losses

The power losses of the PWM converter can be generally divided into conduction and switching losses. The conduction losses are practically the same for different PWM techniques, and they are lower than the switching losses (Malinowski, 2001).

The IGBT module losses comprise the conducting and switching losses of a particular device. The same loss models are used for both semiconductor devices – the IGBT and its antiparallel free-wheeling diode. For the IGBTs and diodes, the instantaneous conducting losses are (Kolar et al. 1991)

$$P_{\text{IGBT, conduct}} = U_{\text{CE0}} i_m(t) + R_{\text{CE0}} i_m^2(t) \quad \text{and} \quad (3.6)$$

$$P_{\text{diode, conduct}} = U_{\text{F0}} i_m(t) + R_{\text{F0}} i_m^2(t), \quad (3.7)$$

where  $i_m(t)$  is the motor instantaneous phase current,  $U_{\text{CE0}}$  is the threshold voltage of the IGBT,  $R_{\text{CE0}}$  is the on-state resistance of the IGBT and  $U_{\text{F0}}$  and  $R_{\text{F0}}$  are the equivalent values of the diode. For the switching losses of the IGBTs and the diodes, the same linear loss model is used (Bierhoff et al. 2000). The average switching losses for a specific period of time are

$$P_{\text{IGBT, sw}} = \frac{U_{\text{DC}}}{U_{\text{rated}}} \frac{I_{\text{motor}}}{I_{\text{rated}}} E_{\text{sw,IGBT}} N_{\text{sw,change}} \quad \text{and} \quad (3.8)$$

$$P_{\text{fw-diode, sw}} = \frac{U_{\text{DC}}}{U_{\text{rated}}} \frac{I_{\text{motor}}}{I_{\text{rated}}} E_{\text{sw, fw-diode}} N_{\text{sw,change}}, \quad (3.9)$$

where  $N_{\text{sw,change}}$  is the number of switchings during a specific time period.  $E_{\text{sw}}$  is the switching loss energy of a particular device given for the reference commutation voltage and current.  $U_{\text{DC}}$  and  $I_{\text{motor}}$  are the actual commutation voltage and current.

### 3.1.5 Inverter extra losses

The extra losses are comprised of the inverter self-usage, for instance microcontroller, internal power supply, display, keyboard, bus-communication, digital and analogue inputs and outputs and the blower and control system power consumption. In this case, these losses are constant. The fan speed is not load dependent. There can also be low current-dependent stray load losses in different constructional parts of the converter and its conductors. Such losses are, however, ignored here. In this thesis, all these losses are included in the extra loss value that is provided by the manufacturer of the frequency converters.

### 3.2 Induction machine losses

An electric motor converts electrical energy into mechanical energy and by doing so incurs losses that are generally described as follows (IEC, 2009)

1. Electrical (stator and rotor) losses vary with load – Currents flowing through the stator and rotor windings produce losses that are proportional to the currents squared multiplied by the winding resistance ( $I^2R$ ). Rotor loss increases the rotor slip.
2. Iron (core) losses are essentially independent of the load. These losses are produced mainly in the laminated core of the stator and to a lesser degree in the rotor. The magnetic field, essential to the production of torque in the motor, causes hysteresis and eddy current losses.
3. Mechanical (friction and windage losses) that are essentially independent of load. Mechanical losses occur in the bearings, fans and seals of the motor. These losses are generally low in low-speed motors, but may be significant in large, high-speed totally enclosed motors.
4. Additional losses (stray-load losses) – the additional fundamental and high-frequency losses in iron; conductor and circulating-current losses in the stator windings, and harmonic losses in the rotor conductors under load. These losses are assumed proportional to the torque squared.

The principal source of loss in an induction machine is the stator winding conduction loss, which comprises the dominant source of loss in small machines. It comprises around 60 % of the total full-load loss in the sub 1 kW range, falling to 25 % at 1 MW and above. Lamination iron loss, caused by hysteresis and eddy currents, accounts for approximately 20 % of the full-load loss. This loss does not generally decrease during operation at a reduced load unless the frequency is changed, thereby giving low efficiency in machines operating at a light load and a rated speed unless the flux level is reduced accordingly. Rotor winding losses, resulting from losses in the aluminium cage rotor are strongly load dependent, and amount to approximately 20 % of the full-load loss. Stray losses, which are due to a number of effects, include induced eddy currents in the stator frame. Stray load losses are load dependent and their amount varies between 0.5 and even 3 per cent of the rated power in induction motors. Stray load losses are insignificant in machines of less than 10 kW but rise to almost 20 % of all losses in induction machines of 1 MW. Friction and windage losses, including bearing loss, which is less than 5 % of the total loss in machines of 10 kW, rise up to 20 % in machines of 1 MW (Mecrow and Jack, 2008).

#### 3.2.1 Simulated motor losses

The simulated losses are divided into four categories: stator copper losses, rotor copper losses, stator iron losses and rotor iron losses. The simulation software takes neither friction and windage nor additional (stray) losses into account, and when the simulated losses are compared with the measured losses, the friction and windage losses as well as stray load losses are added to the simulated losses. This can be explained by the fact that the FEM tool does not, in this case, model the winding eddy currents and the stray losses in the machine construction parts.

### 3.3 Resistive losses

The resistive losses of the stator are calculated from the resistances and the currents of the windings

$$P_{\text{res}}^s = \sum_{i=1}^m R_{si} (i_i^s)^2 \quad (3.10)$$

and the resistive losses in the rotor cage are

$$P_{\text{res}}^r = \int_V -J \cdot \frac{\partial A}{\partial t} dV = \sum_{i=1}^{Q_r} \int_{V_i} \sigma \left[ \left( \frac{\partial A}{\partial t} \right) - \frac{u_i^r}{l} \frac{\partial A^2}{\partial t} \right] dV, \quad (3.11)$$

where  $V_i$  is the volume of the  $i^{\text{th}}$  rotor bar inside the two-dimensional core region. Equation (3.11) also includes the power fed to the ends of the rotor cage.

#### 3.3.1 Iron loss model

The FEM software here uses a comprehensive dynamic loss model that takes into account the loci of the magnetic flux density vector and is able to compute the losses as function of time

#### Eddy-current losses

The classical eddy-current energy dissipation is proportional to the induced currents in the magnetic material. These eddy currents depend on the geometry and conductivity of the material as well as on the rate of change of the magnetic flux density (Bertotti, 1998). For an infinitesimal variation of the magnetic flux density vector  $\partial B$ , the infinitesimal energy dissipation is modelled as

$$\partial \omega_c = k_c \frac{\partial B}{\partial t} \left| \partial B \right|, \quad (3.12)$$

where  $k_c$  is the classical eddy-current loss coefficient that depends on the thickness and conductivity of the material (Bertotti, 1998).

#### Hysteresis, excess and rotational losses

The energy dissipation resulting from the domain wall motion can be separated into a quasi-static hysteresis part and a dynamic part, which is conventionally called excess loss (Bertotti, 1998). The excess and hysteresis losses caused by the rotational magnetic field are different from these owing to the alternating magnetic fields. Because of the alternating part or amplitude of the magnetic flux density vector, the modelling of these phenomena requires separation of the losses caused by the rotation of the vector. The excess losses caused by the rotation of the magnetic flux density vector are included in the quasi-static hysteresis losses. These rotational losses all together with the alternating quasi-static hysteresis losses are modelled as

$$\partial\omega_h = k_h \mathbf{B} |\partial\mathbf{B}| + k_r \frac{1 - \frac{|\mathbf{B}|}{B_s}}{1 + b \left(1 - \frac{|\mathbf{B}|}{B_s}\right)^2} |\mathbf{B}| \partial\theta, \quad (3.12)$$

where  $\theta = \arctan(B_y/B_x)$  is the phase angle of the flux density vector with respect to some fixed axis (here the x-axis),  $\partial\theta$  is the infinitesimal variation of this angle,  $k_h$  and  $k_r$  are hysteresis and rotational loss coefficients, respectively,  $B_s$  is the saturation flux density and  $b$  is a constant parameter related to the texture and grain size of the material. The first part of Equation (3.12) describes the dissipation caused by a purely alternating magnetic flux density and the second part describes the dissipation caused by a purely rotating magnetic flux density. With arbitrary loci of the magnetic flux density vector, the dissipation is the sum of these two terms.

### 3.4 Drive system losses

The frequency converter produces additional losses to the motor. These losses are of utmost importance from the perspective of this work. A lot of effort is put into analysing the effects of the PWM signals on the laminations and rotor windings of a frequency-converter-supplied drive. Stator winding excess losses are excluded from the study as round enamelled wires are too difficult to model in the FEM model intended for this kind of combined simulation.

Most converters have rated efficiencies varying from 95 to 98 %, and high efficiencies even at relatively small loads. The average drive efficiency is about 2 % units lower than the grid-connected motor efficiency. Between the various drive combinations of the same power rating, differences in the average efficiency up to 4 % are found. However, there is no general rule at hand, as to which converters suit best for a particular motor (Slaets et al. 2000).

#### Additional motor losses when operated on a frequency converter

The harmonics of voltage and current in a cage-induction motor supplied from a frequency converter cause additional iron and  $I^2R$  winding losses in the stator and rotor. The total value of these losses is essentially independent of the load. These additional losses decrease with the increasing switching frequency in the converter. In adverse circumstances, the additional losses in the motor caused by the frequency converter can increase the total motor losses up to 15–20 % compared with the grid operation (IEC, 2009). The additional losses generated by the PWM and loss distribution have been widely studied in the literature. For example Hildebrand and Roehrdanz (2001) investigated the losses in 5.5 kW three-phase induction machines fed by a PWM converter and found out that the harmonic losses increase generally with higher pulse frequencies, and the increase is pronounced at low fundamental frequencies. Boglietti et al. (2007) have studied the efficiency of a 2 hp (1.5 kW) induction motor under different loadings and supply conditions. Boglietti et al. (2007) stated that the induction motor losses are a function of fundamental waveform, load condition and switching conditions.

The IEC (2003) gives the induction motor losses for a frame size 315 for a sinusoidal voltage and a PWM supply with an optimized pulse pattern (pulse frequency 3 kHz).

Table 3.1. 315 frame size induction motor losses according to IEC (2003).

	<b>Sinusoidal</b>	<b>Additional losses caused by PWM harmonics</b>
Stator winding losses	41 %	0.5 %
Rotor winding losses	26 %	2 %
Iron losses	25 %	12 %
Additional load losses	2 %	0.5 %
Frictional	6 %	-
<b>Total</b>	<b>100 %</b>	<b>117%</b>

### **Loadability of an induction motor in the frequency converter use**

As mentioned above, the PWM operation of the frequency converter produces additional harmonics to the system; harmonics generate additional losses, which result in a higher operating temperature of the motor, the most important issue in sizing of the motor thus being the temperature. Hence, in the VSD, the loadability of the motor is lower than in the direct-on-line use. This means that the motor reaches the design temperature with a lower load (torque) than in the DOL use. Consequently, the motors must be derated in the frequency converter use. For AC motor inverter operation, the motor power derating due to PWM loss varies from 0 to 20 % (Haring, 2000). For example ABB provides loadability curves for different frame sizes of the motors with DTC (ACS800) and vector controlled (ACS550) frequency converters.

## 4 SIMULATION MODELS

The simulator used in this thesis consists of two parts. The first part is a C-language platform that simulates the frequency converter operation, the process model and the analytical motor model, and it also handles system initialization and saves routines. The second part is the FEM motor model. Between these two parts the information is exchanged through a dynamic link library (DLL) at given sample times. The overview of the simulator is shown in Fig. 4.1.

In the initializations files, the simulation parameters are given, for example if the motor model used in the simulation is an analytical or a FEM model, load torque, a switching frequency reference and a speed reference.

### 4.1 Overview of the simulator

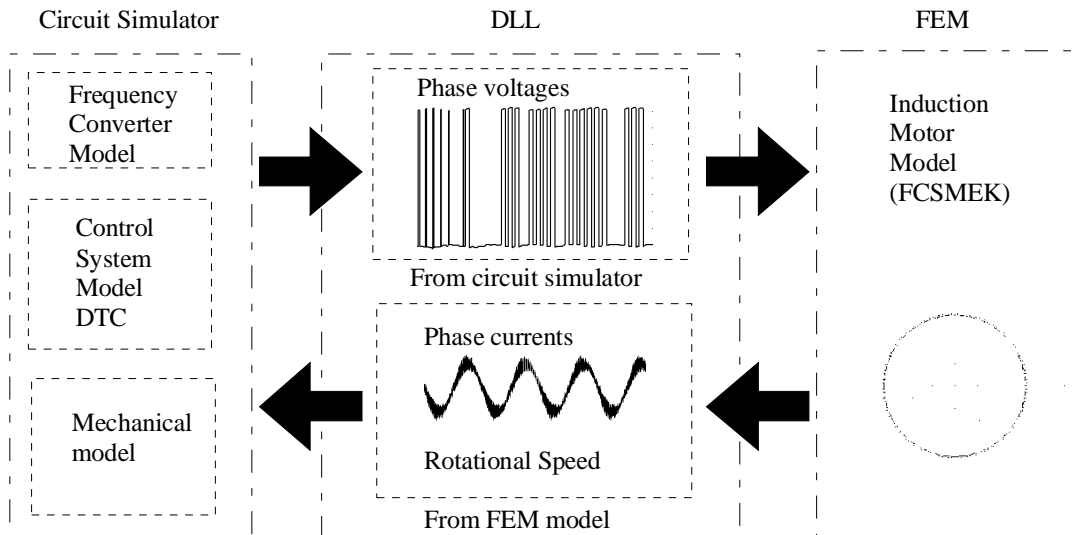


Fig 4.1. Block diagram and the signal connections of the simulator.

### Assumptions in the simulator design

All electric equivalent circuit parameters of the motor and the frequency converter are constant. There is no temperature dependence in resistances, and inductances have no saturation. The on-voltage drop in the diodes is taken into account, and the diode can only conduct in forward direction. The inverter model includes resistive and junction on-voltage drops by both the diode and the transistor. The switch can change its state at infinite speed; however, the dead time has been modelled so that the upper and lower IGBTs in the same leg cannot be switched on and off simultaneously. The motor cable is assumed to be ideal. The FEM motor model is initialized in a constant temperature of 80 °C. The semiconductor devices are assumed to be in a constant temperature of 125 °C, and the capacitor bank temperature is assumed to be 80 °C.

## 4.2 Frequency converter model

The frequency converter model is divided into two modules. The first module contains a model for the diode bridge and the intermediate circuit. The second module models the inverter bridge.

### 4.2.1 Diode bridge and intermediate circuit

The network is modelled as an ideal 50 Hz sinusoidal voltage supply. Between the ideal voltage supply and the diode bridge, there is an inductance  $L_{s-c}$ , which represents the short-circuit inductance of the supplying network. In this thesis, for the supplying network, a short-circuit ratio SCR=100 is used in the simulations. As inputs to the diode bridge there are three-phase network voltages and the intermediate circuit DC current. As the output of the module there is the intermediate circuit voltage  $U_{DC}$ . A line-commutated diode bridge is used as a rectifier. The group of two differential equations describes the behaviour of the diode bridge, the intermediate circuit and the short-circuit inductance. The indices in the equations vary depending on the state of the bridge. For the conducting state the equations can be written as

$$\frac{di_{uc}}{dt} = \frac{di_{dd}}{dt}, \quad (4.1)$$

$$\frac{di_{lc}}{dt} = -\frac{di_{dd}}{dt}, \quad (4.2)$$

$$\frac{di_{nc}}{dt} = 0, \quad (4.3)$$

$$\frac{di_{dd}}{dt} = \frac{u_{uc} - u_{lc} - u_C - i_{dd}R_{DC}}{2L_{s-c} + L_{DC}}, \quad (4.4)$$

$$\frac{du_C}{dt} = \frac{C_K}{i_c}, \quad (4.5)$$

where the subscripts denote the phases: uc – conducting upper phase, lc – conducting lower phase and nc – phase not conducting. The rectifier bridge connections in the conducting state are presented in Fig 4.2.

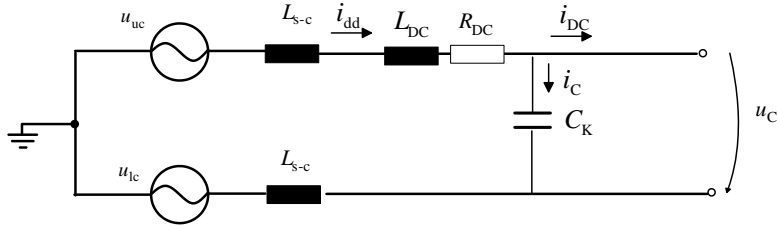


Fig 4.2. Rectifier bridge connections in the conducting state.

When the intermediate circuit (capacitor) voltage  $u_c$  rises over the voltage potential of the upper DC bus, the derivatives of the currents are set to zero. This prevents the negative current from flowing through the diodes. The behaviour of the bridge during commutation is described by equations

$$\frac{di_-}{dt} = \frac{1}{(2L_{DC} + 3L_{s-c})} \left[ u_- - (u_+ - u_-) \left( \frac{L_{DC} + L_{s-c}}{L_{s-c}} \right) - u_c m i_{dd} r_{dc} - u_c \right], \quad (4.6)$$

$$\frac{di_+}{dt} = \frac{u_+ - u_-}{L_{s-c}} - \frac{di_-}{dt}, \quad (4.7)$$

$$\frac{di_{dd}}{dt} = \pm \left( \frac{di_+}{dt} + \frac{di_-}{dt} \right), \quad (4.8)$$

$$\frac{di_c}{dt} = m \frac{di_{dd}}{dt}, \quad (4.9)$$

$$\frac{dU_C}{dt} = \frac{i_C}{C}, \quad (4.10)$$

where the subscripts denote the phases:  $c$  – conducting phase,  $-$  phase where the current decreases,  $+$  the phase where current is rising. In Equations (4.6)–(4.10), the upper sign denotes the upper branch commutation and the lower sign the lower branch. The rectifier bridge connections during the commutation of the upper phases are presented in Fig 4.3.

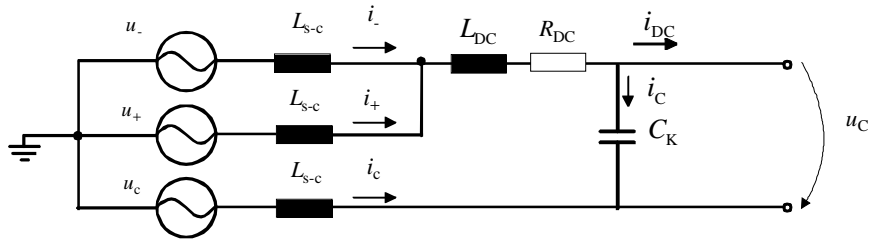


Fig 4.3. Rectifier bridge connections during the commutation of the upper phases.

#### 4.2.2 Inverter model

The three-phase inverter model consists of six transistors and free-wheeling diodes. The six IGBT transistors of the bridge are modelled as ideal switches with on-state resistances and threshold voltages. In Fig 4.4, the model of one switching device is illustrated. The forward slope resistance  $R_{CE0}$  and the threshold voltage  $U_{CE0}$  describe the on-state losses, while  $R_{F0}$  and  $U_{F0}$  describe the on-state resistance and the threshold voltage, respectively, of the free-wheeling diode.

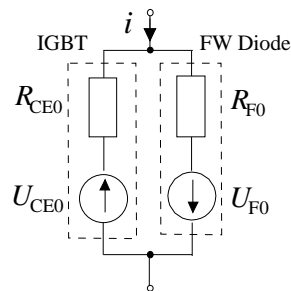


Fig 4.4. Model of one switching device. The current direction determines which component in an IGBT free-wheeling diode pair is conducting.

### 4.3 Frequency converter nonidealities

Usually, in the simulation of variable speed drives, some simplifications are made. The current measurements are assumed to be exact and without delay. Furthermore, the intermediate circuit voltage is assumed constant and the dead time is assumed zero; in this simulator, these phenomena are taken into account and the effects of these nonidealities are studied.

#### 4.3.1 Current measurement delay and A/D conversion

In modern AC drives, the control is performed with digital signal processors. The control system calculates the measured DC link voltage and stator currents to obtain information of the motor state. Stator currents are normally measured using Hall-effect-based sensors, the current

is low-pass-filtered to remove the switching noise, and an A/D converter is used to digitize the current. The nonlinearity of the Hall sensors, the thermal drift of the analogue elements, and the nonlinearity of the A/D converter cause errors in the current value. Each processing step adds delay, and thus, the current seen by the control system is always a delayed value of the motor current, Fig 4.5.

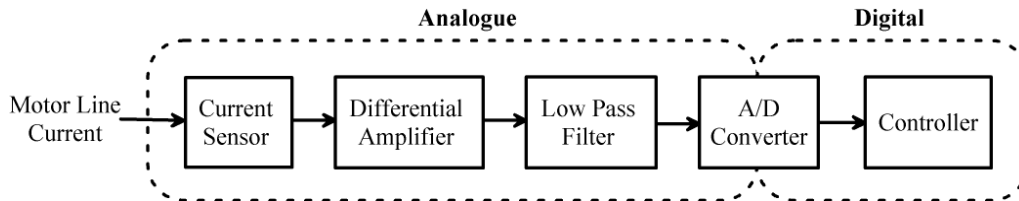


Fig 4.5. Principle of the current measurement.

The A/D conversion of the phase currents and the DC link voltage adds error to the current. For example: a 12 bit A/D converter is used to digitize the 200 A RMS phase current and the DC voltage. Let us assume that the maximum value of the voltage is 1000 V and the maximum value of the peak value of the phase current is 500 A. In the current conversion, one bit is used for the sign of the current, and as a resolution for the current, we get  $500 \text{ A} / 11^2 = 0.24 \text{ A}$ . The DC voltage cannot be negative, and thus, the resolution of voltage is  $1000 \text{ V} / 12^2 = 0.24 \text{ V}$ . Although the effect of A/D conversion was studied during the work of this thesis and this is one feature in the simulator, the results are not presented here, because they are negligible from the energy efficiency point of view in the VSDs.

#### 4.3.2 Dead time

Because of the finite turn-off and turn-on times of the power switches, the upper and lower IGBTs in the same leg cannot be switched on and off simultaneously to avoid short circuits, but there has to be a time delay between the switching commands. In the literature, this delay is referred to as dead time or blanking time. The effect of dead time on the phase voltage is presented in Fig 4.6. The value of the dead time varies depending on the size and type of the power switches. Basically, the value of the dead time increases with the capability of handling larger powers. The dead time induces harmonic distortion of the voltage waveforms by an increased low-level harmonic content of the third, fifth and seventh harmonics of the fundamental frequency. The distortion owing to the dead-time effects is problematic in closed-loop control systems, such as high-performance AC motor drives, as the voltage loss degrades the quality of flux, torque or speed estimation algorithms.

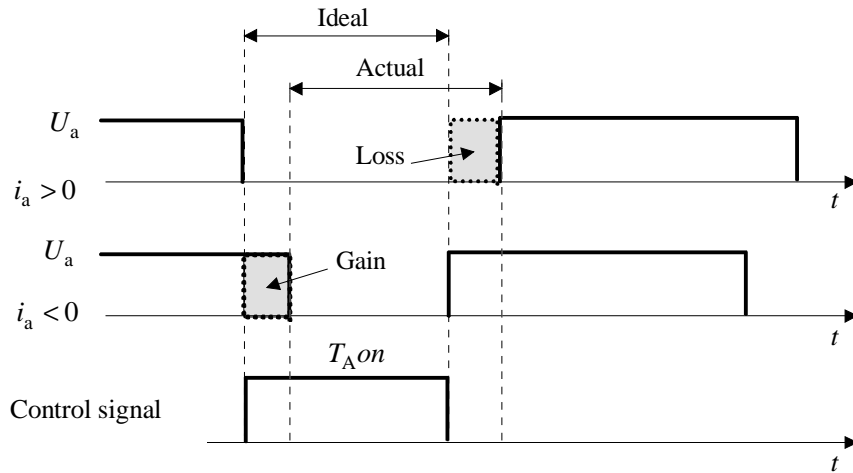


Fig 4.6. Effect of dead time on the phase voltage.

Since both the switches in the inverter leg are off during the dead time, the phase voltage depends on the direction of the phase current  $i_a$ .

#### 4.4 Motor models

The machine models that are needed to design control loops are very different from those used for designing the machine. Machine designers have to apply tolerance levels (e.g. for power levels) that are less than 1 %, while the control system designs are only rough approximations, where even a 10 % error can be considered acceptable. This is because every control scheme must absorb the changes in the plant parameters, which are due to the changes in the temperature, supply, nonlinearity and so on (Vas, 1998). The control system designer uses the models that are based on analytical equations.

##### 4.4.1 Analytical motor models

Mathematically, the dynamic behaviour of an induction motor is described by using complex-valued space vectors. The following equations are written in the stator reference frame. In the inverse  $\Gamma$ -equivalent circuit, all leakage inductance is located in the stator side; this is not physically correct, but it simplifies the rotor-side equations. In the numerical calculation of the inverse  $\Gamma$ -equivalent circuit, there is no need for coordinate transformations from stator to rotor coordinates or vice versa. Thus, the differential equations that describe the motor behaviour can be numerically integrated into the stator coordinates.

##### T-equivalent circuit

The equivalent circuit of the induction motor presented in Fig 4.7. is described with five parameters: stator resistance  $R_s$ , rotor resistance  $R_r$ , stator leakage inductance  $L_{s\sigma}$ , rotor leakage inductance  $L_{r\sigma}$ , and magnetizing inductance  $L_m$ . The equivalent circuit parameters can be obtained with a short-circuit and locked-rotor test.

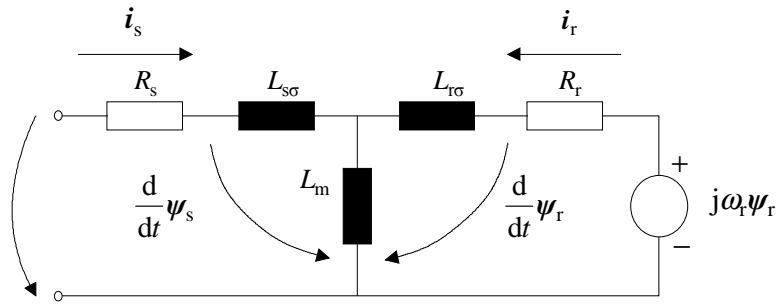


Fig 4.7. Dynamic T-equivalent circuit of the induction motor.

### Inverse $\Gamma$ -equivalent

The analytical motor model is illustrated in Fig 4.8 (De Donker and Novotny, 1994). The circuit is expressed in the stationary reference frame and it is determined by four parameters: stator resistance  $R_s$ , rotor resistance  $R_R$ , total leakage inductance  $L_\sigma$  and magnetizing inductance  $L_M$ . The inverse  $\Gamma$ -equivalent circuit parameters can be obtained using conventional T-circuit parameters as follows. The rotor resistance

$$R_R = \left( \frac{L_m}{L_m + L_{r\sigma}} \right)^2 R_r, \quad (4.11)$$

the magnetizing inductance

$$L_M = \frac{L_m^2}{L_m + L_{r\sigma}}, \quad (4.12)$$

and the total leakage inductance

$$L_\sigma = L_{s\sigma} \frac{L_m L_{r\sigma}}{L_m + L_{r\sigma}}. \quad (4.13)$$

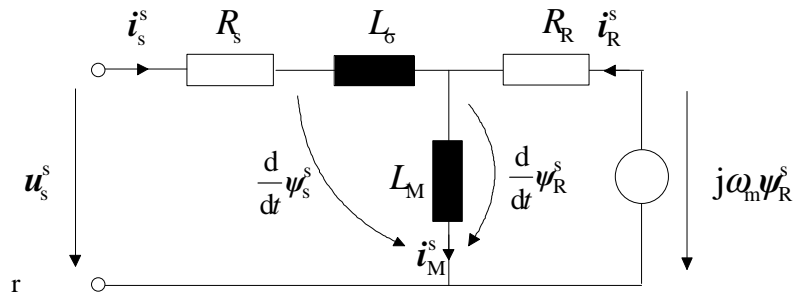


Fig 4.8. Dynamic  $\Gamma$ -equivalent circuit for a squirrel cage induction motor.

The voltage equations for the stator and rotor side can be written as

$$\mathbf{u}_s = R_s \mathbf{i}_s + \frac{d\boldsymbol{\Psi}_s}{dt} \text{ and} \quad (4.14)$$

$$0 = R_R \mathbf{i}_R + \frac{d\boldsymbol{\Psi}_R}{dt} - j\omega_r \boldsymbol{\Psi}_R . \quad (4.15)$$

Equations for the stator and rotor flux linkages can be written from Fig 4.8

$$\boldsymbol{\Psi}_s = L_\sigma \mathbf{i}_s + L_M (\mathbf{i}_s + \mathbf{i}_R) \text{ and} \quad (4.16)$$

$$\boldsymbol{\Psi}_R = L_M (\mathbf{i}_s + \mathbf{i}_R) . \quad (4.17)$$

The stator and rotor current can be written with the help of flux linkages

$$\mathbf{i}_s = \frac{\boldsymbol{\Psi}_s - \boldsymbol{\Psi}_R}{L_\sigma} \text{ and} \quad (4.18)$$

$$\mathbf{i}_R = \frac{L_\sigma + L_M}{L_M L_\sigma} \boldsymbol{\Psi}_R - \frac{1}{L_\sigma} \boldsymbol{\Psi}_s . \quad (4.19)$$

By substituting (4.16)–(4.19) into (4.14) and (4.15) and rearranging the terms results in a system of equations, where the flux linkages are represented as state variables that describe the induction motor behaviour

$$\begin{bmatrix} \frac{d\boldsymbol{\Psi}_s}{dt} \\ \frac{d\boldsymbol{\Psi}_R}{dt} \end{bmatrix} = \begin{bmatrix} -\frac{R_s}{L_\sigma} & \frac{R_s}{L_\sigma} \\ \frac{R_R}{L_\sigma} & j\omega_r - \frac{R_R(L_\sigma + L_M)}{L_\sigma L_M} \end{bmatrix} \begin{bmatrix} \boldsymbol{\Psi}_s \\ \boldsymbol{\Psi}_R \end{bmatrix} + \begin{bmatrix} 1 \\ 0 \end{bmatrix} \mathbf{U}_s . \quad (4.20)$$

#### 4.4.2 FEM model

The FEM model of the motor is based on the two-dimensional finite element method and circuit equation of the windings (Arkkio 1987). The magnetic field in the core region is calculated using a magnetic vector potential formulation, in which the vector potential and current density have only z-axis components. The phase windings in the stator or rotor are modelled as filamentary conductors with a uniformly distributed current flowing through all the coils that belong to the same phase. The rotor bars are modelled as solid conductors, in which the current density varies according to eddy currents. The sources of the magnetic field are the phase currents, the voltage drop in the rotor bars and the magnetic force of the permanent magnet, depending on the type and construction of the machine.

The relations between voltage and current are determined in the circuit equations of the stator and rotor windings, which also include the end-winding impedances and the short-circuit rings.

As a result, only phase voltages are needed as an electrical input for the FEM model. The electromagnetic torque is calculated by virtual work principle, and the movement of the rotor is determined from the equation of motion. At each time step, a new position is calculated for the rotor and the air-gap mesh is redefined (Kanerva et al., 2005).

#### 4.5 Coupled simulation

Babak et al. (2009) exhaustively address the coupling of 2-D FEM equations with external circuit equations. The main application of these techniques is the simulation of electrical drives, transformers and actuators. Babak et al. (2009) also review, analyze and classify different coupling methods, and the main features and problems of different techniques are summarized.

In this thesis, the coupling method referred to as “current output approach” in Kanerva (2005) is applied. The magnetic field in the electrical machine is modelled by the two-dimensional FEM and solved together with the circuit equations of the windings. In the current output approach, the phase currents of the electrical machine are solved together with the magnetic field, when the supply voltages are given as inputs.

#### 4.6 Process model

As a process model, a single equation of motion is used. The derivative of speed is

$$\frac{d\omega}{dt} = \frac{p}{J} (T_e - T_{Load}), \quad (4.21)$$

where  $\omega$  is the angular speed,  $p$  is the number of pole pairs,  $J$  is the rotor inertia,  $T_e$  is the electrical torque and  $T_{Load}$  is the load torque.

#### 4.7 Model of the control system

In the simulator, two different frequency converter control systems have been modelled, and in this thesis, their operation has been verified. The first control system uses the direct torque control, and the second control system is a rotor-flux-oriented current control that uses symmetrical two-phase modulation.

##### 4.7.1 Model of the direct torque control system

In the following sections, the focus is on the model of the direct torque control system applied in this thesis. The control system model contains four parts: speed/frequency control, torque and flux control, hysteresis control and flux correction. The speed/frequency control is a traditional PI controller with an option to use the motor model speed or frequency calculated from the flux estimate speed as feedback information.

##### Torque and flux control

The torque and flux control is the core of the DTC. In each control cycle, the stator voltage x- and y-components are estimated using the switch combinations of the IGBT bridge and the filtered DC voltage. The flux integral is calculated using measured stator currents and estimated stator voltages (from the switch states and the measured DC link voltage), Equation (1.20). The flux integral equation is corrected with the flux losses resulting from the voltage losses of the semiconductors and the stator resistance. The flux sector is determined. The torque estimate is

calculated by using Equation (1.21), the absolute value of flux is compared with the reference values, and the error signals are generated. Simple control bits are created that give information where the flux and torque estimates lie, that is, whether they are within or outside the hysteresis limits. The modulator chooses the next switch combination according to the control bits; the voltage vector selection is presented in Table 4.1.

Table 4.1. Voltage vector selection according to the flux sector and the desired change in torque and flux.

Flux sector		1	2	3	4	5	6
Torque bit	Flux bit						
1	0	$u_3$	$u_4$	$u_5$	$u_6$	$u_1$	$u_2$
	1	$u_2$	$u_3$	$u_4$	$u_5$	$u_6$	$u_1$
0	-	$u_0$	$u_0$	$u_0$	$u_0$	$u_0$	$u_0$
-1	0	$u_5$	$u_6$	$u_1$	$u_2$	$u_3$	$u_4$
	1	$u_6$	$u_1$	$u_2$	$u_3$	$u_4$	$u_5$

### Hysteresis control

In the DTC, even though the hysteresis bands are set to be constant, the switching frequency varies according to the operation conditions such as motor speed, flux level and output torque. The switching frequency is controlled with a PI controller, the inputs of which are the low-pass-filtered value of the current switching frequency and the switching frequency reference. The flux and torque hysteresis ratios are chosen to obtain a low torque and current ripple in every motor operating condition. The switching frequency calculation obtains the switch states from the modulator, which controls the power switches. The switch states have two binary values in every three phases: zero or one. If the current switch state is different from the previous value, a switching has taken place. The PI controller keeps the switching frequency constant in the steady state even though the switching frequency can burst in transient operation. The losses in the power switches are calculated and the thermal behaviour of the switches is modelled. The maximum switching frequency is limited by hardware thermal restrictions.

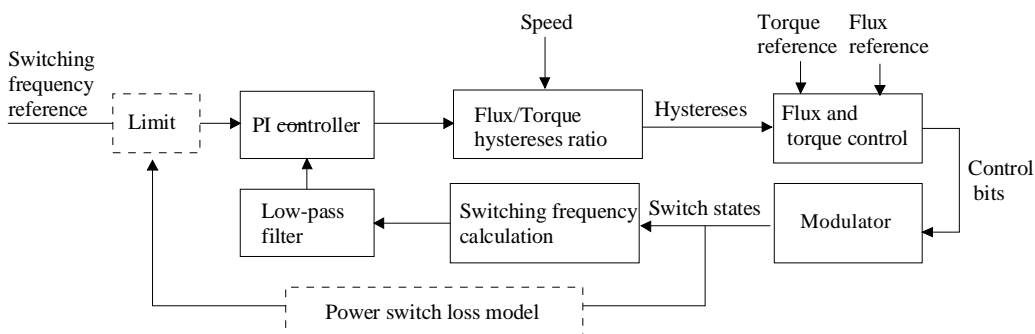


Fig 4.9. Principle of the hysteresis control used in the DTC modelling in this thesis. The boxes with the dashed line are not modelled even though they exist in an actual control system.

## Flux correction

Especially at low speed in the DTC, the integral equation (1.20) is too erroneous, and the motor stator flux linkage drifts so that its rotation is no longer origin centred. One method to solve this problem is to use a rotor-oriented traditional motor model that prevents the motor stator flux linkage from drifting. This traditional model of the motor will be referred to as ‘the current model’ of the motor as usually in the literature. The combination of the voltage model and the supervising current model is used to keep the flux on an origin-centred trajectory. The voltage model operates as the main model, and it is calculated with a very fast sampling time. The current model is calculated with a much slower sampling rate. The stator flux linkage estimate is corrected by using the difference between the stator flux linkage calculated from the current model and the stator flux linkage calculated from the voltage model. Stator flux correction is weighted by a weighting the coefficient  $w_{cm}$ . The following equation gives the principle of this correction (Niemelä, 1999),

$$\psi_{s,est} = \psi_{s,vm} + w_{cm} (\psi_{s,cm} - \psi_{s,vm}) \quad (4.22)$$

the value of the weighting coefficient depends on the operation point of the motor (Kaukonen, 1999). When using a current model, an inductance model of the motor and a speed signal are needed. In the simulator, the speed signal is not a problem, because it is an output of the FEM motor model and can therefore be used directly. When simulating a motor that has not yet been constructed, or a motor the inductances of which are not known beforehand, the flux correction method could be a problem. This simulation problem can be solved by designing the identification procedure similar to an actual DTC converter in the simulation program or to use the FEM program flux instead of the current model flux.

$$\psi_{s,est} = \psi_{s,vm} + w_{cm} (\psi_{s,cm} - \psi_{s,FCSMEK}) \quad (4.23)$$

In the following simulation, the results obtained with the current model flux linkage and the FEM flux linkages are compared. The stator flux linkage is shown in Fig. 4.10 and the spectra of the simulated currents are shown in Fig. 4.11.

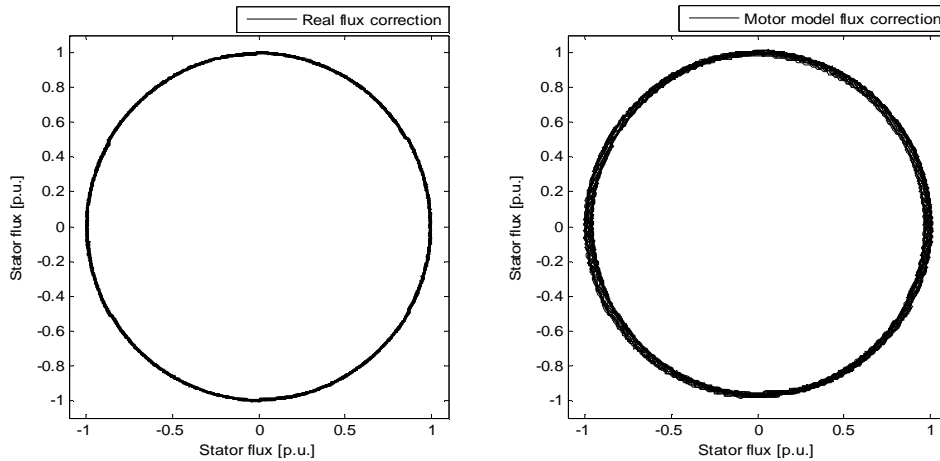


Fig 4.10. FEM motor model stator flux linkage for a 1 second time period. The stator flux linkage is more eccentric, when the analytical motor model is used for flux correction.

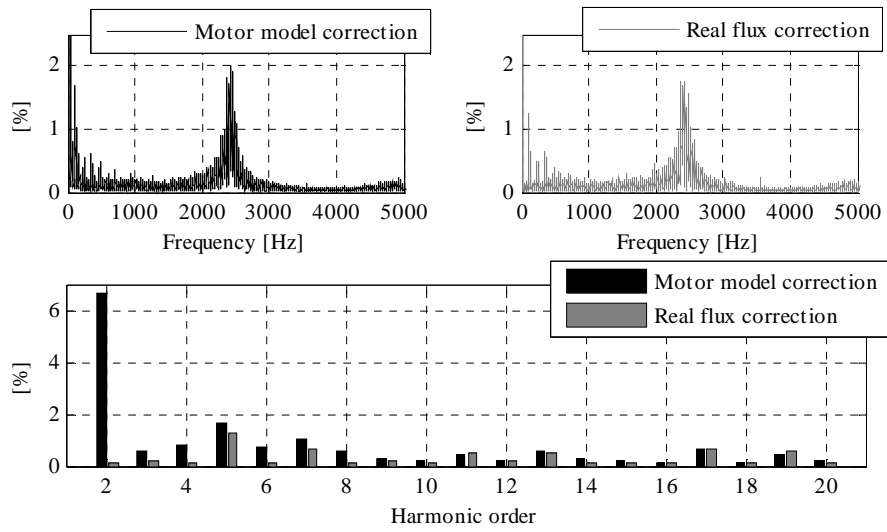


Fig 4.11. Spectra of the simulated phase currents of a 200 kW induction motor. The only difference in the simulation results is the 2<sup>nd</sup> harmonic component. The fundamental wave component is exactly the same in both simulations.

In the results, the current spectra are almost equal. The main difference is the 2<sup>nd</sup> harmonic component of the stator current. The simulation results with this flux correction method could be improved with some kind of an adaptive motor model with variable inductances. Although this is one way to correct the voltage integral, we can assume that the method used in the commercial DTC converter is far more sophisticated and can actually keep the flux origin centred, and the absolute value of the flux linkage is optimal in the motor operating condition.

#### 4.7.2 Model of the rotor-flux-oriented current control

The simulation model of the rotor-flux-oriented current control uses actual values of the stator currents  $i_{sd}$  and  $i_{sq}$  in the rotor-flux-oriented reference frame and contains a closed-loop control of speed, torque, rotor flux and currents. The schematic of the rotor-flux-oriented current control is shown in Fig. 4.12. The control system is calculated at the beginning of the modulation sequence. The speed, torque, flux and current controllers are simple PI controllers.

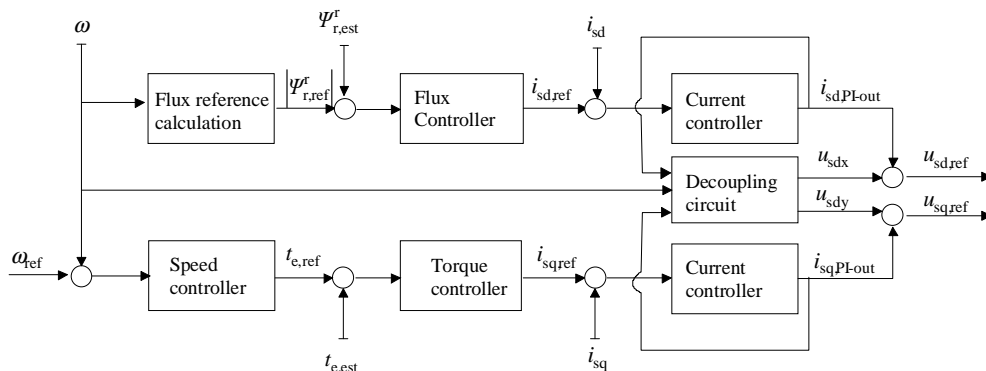


Fig 4.12. Schematic of the rotor-flux-oriented control of a voltage-source-inverter-fed induction machine.

### Decoupling circuit

Without a decoupling circuit, there is an unwanted coupling between the stator circuits on two axes. To control the flux linkage (direct-axis stator current) and torque (quadrature-axis stator current component) independently, there is a need to use a decoupling circuit. Various implementations of the necessary decoupling circuit have been presented in the literature; here, a straightforward method presented in (Vas, 1998) is used. The direct-axis voltage decoupling is thus written as

$$u_{sdx} = -\omega_r i_{sq} \left( L_s \frac{L_m^2}{L_r} \right) \quad (4.24)$$

and the quadrature-axis decoupling

$$u_{sdy} = \omega_r i_{sd} \left( L_s - \frac{L_m^2}{L_r} \right) + \omega_r |i_{mr}| \frac{L_m^2}{L_r}, \quad (4.25)$$

where  $i_{mr}$  is the magnetizing current in rotor flux coordinates. The decoupling circuit outputs are added to the current controller outputs.

### Flux reference calculation

The stator flux linkage reference value is given as an input variable by the user. The rotor flux linkage nominal value is calculated, and the rotor flux reference used by the control system is the stator flux linkage times the rotor flux linkage nominal value. To obtain field weakening operation, the stator flux linkage is

$$\psi_{s,ref} = \psi_{s,ref} \frac{U_{max}}{\omega_{ref}}, \quad (4.26)$$

if  $\omega > U_{max}$ , where

$$U_{max} = \frac{U_{dc,flt}}{\sqrt{3}}. \quad (4.27)$$

The most problematic part of the rotor-flux oriented vector control can be bypassed, since the rotor flux linkage angle can be easily calculated, and because the stator flux linkage components and the stator currents are outputs of the FEM motor model and known for each time step. The voltage reference is transformed into stator coordinates, and its angle and magnitude are defined. The switching durations of the active voltage vectors are determined similarly as in the space vector modulation presented earlier in Table 1.1. Here, the unit circle is divided into 12 sectors instead of 6 in the space vector modulation, Fig 4.13. The modulator chooses the voltage vector according to the sector and modulation sequence presented in Table 4.2. The minimum pulse length is limited so that if the active vector time  $t_1$  or the zero vector time  $t_0$  is shorter than the minimum pulse length, the time is added to the active vector time  $t_2$ .

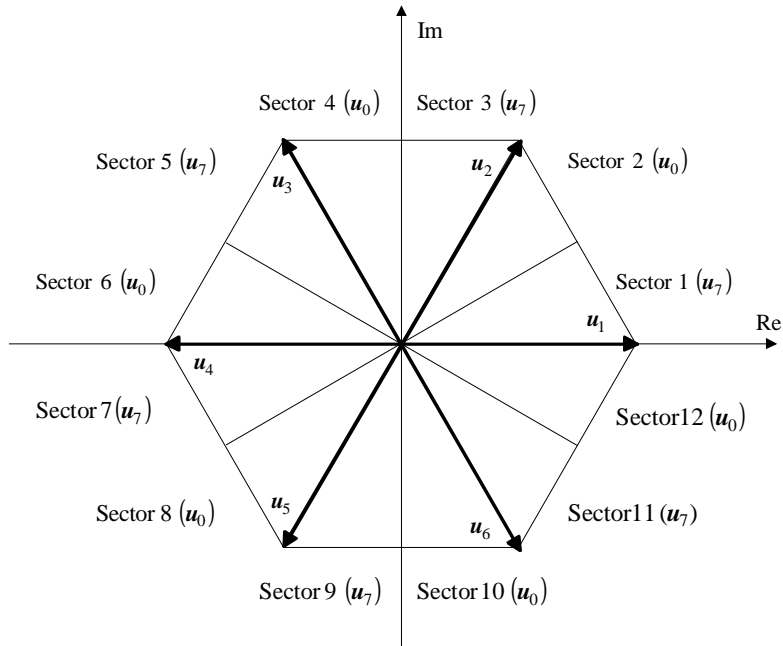


Fig 4.13. Unit circle, divided into 12 sectors in the symmetrical two-phase modulation. The modulator uses the two nearest active vectors and the zero vector  $u_0$  or  $u_7$  for modulation.

Table 4.2. Switching table of the symmetrical two-phase modulation.

<b>Sector</b>	<b>1</b>	<b>2</b>	<b>3</b>	<b>4</b>	<b>5</b>	<b>6</b>
<b>1</b>	$u_1$	$u_2$	$u_7$	$u_7$	$u_2$	$u_1$
<b>2</b>	$u_0$	$u_1$	$u_2$	$u_2$	$u_1$	$u_0$
<b>3</b>	$u_0$	$u_3$	$u_2$	$u_2$	$u_3$	$u_0$
<b>4</b>	$u_3$	$u_2$	$u_7$	$u_7$	$u_2$	$u_3$
<b>5</b>	$u_3$	$u_4$	$u_7$	$u_7$	$u_4$	$u_3$
<b>6</b>	$u_0$	$u_3$	$u_4$	$u_4$	$u_3$	$u_0$
<b>7</b>	$u_0$	$u_5$	$u_4$	$u_4$	$u_5$	$u_0$
<b>8</b>	$u_5$	$u_4$	$u_7$	$u_7$	$u_4$	$u_5$
<b>9</b>	$u_5$	$u_6$	$u_7$	$u_7$	$u_6$	$u_5$
<b>10</b>	$u_0$	$u_5$	$u_6$	$u_6$	$u_5$	$u_0$
<b>11</b>	$u_0$	$u_1$	$u_6$	$u_6$	$u_1$	$u_0$
<b>12</b>	$u_1$	$u_6$	$u_7$	$u_7$	$u_6$	$u_1$

## 5 ANALYSIS OF MEASUREMENTS AND SIMULATION RESULTS

In this thesis, a lot of effort has been put to reach the correct inverter output current spectra, in particular in the DTC control. In the electric drive, the fundamental wave is transferring most of the electric power to the motor and further via the air gap to the motor shaft. The different control systems similarly as the same control system with different controller parameters have different voltage and current spectra, and therefore the electric power flowing through the drive can be in different frequency ranges. Figures 5.1–5.3 have been compiled so that the results of current and voltage DFTs are multiplied by each other. 100 per cent power represents the result of the DFT under 20 kHz.

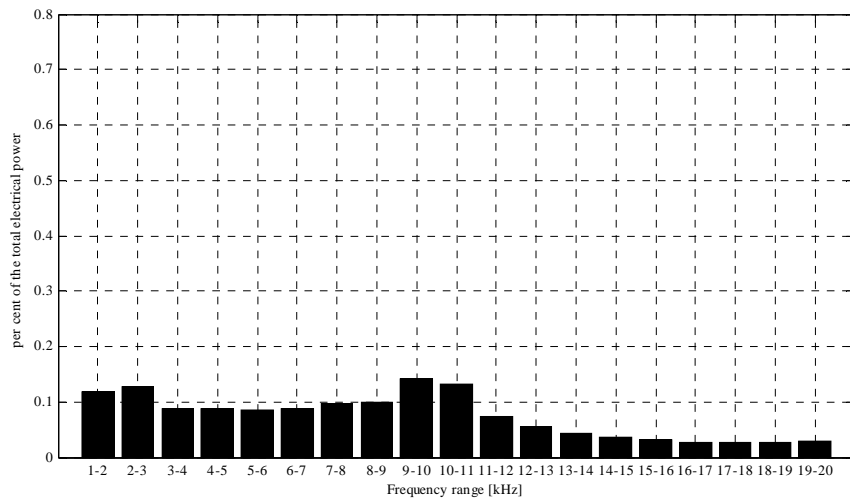


Fig 5.1. DTC inverter-fed induction motor electrical power as a function of frequency. The measured results are obtained with a 37 kW motor driven with a 50 Hz frequency reference. In the measurements, the average switching frequency is 2 kHz and the load torque is 90 per cent of the nominal load. The fundamental wave frequency carries 97.5 %, and the rest of the harmonic components under 1 kHz carry 0.4 % of the total power under 20 kHz. In the frequencies above 10 kHz, only 0.28 % of the total power is flowing through the drive.

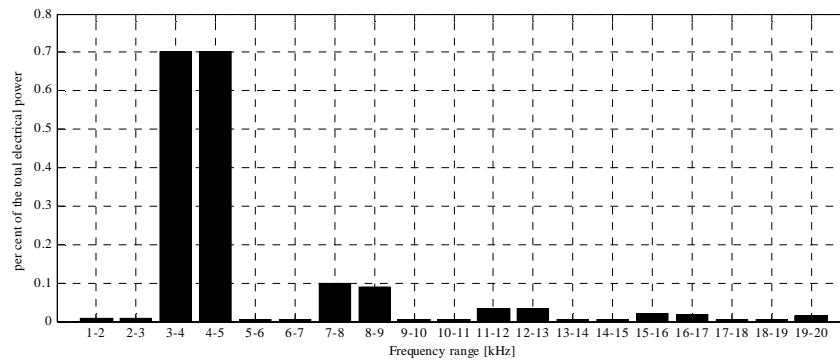


Fig 5.2. Vector-controlled inverter-fed induction motor electrical power as a function of frequency. The measured results are obtained with a 37 kW motor driven with a 50 Hz frequency reference. In the measurements, the switching frequency is set to 4 kHz and the load torque is 92 per cent of the nominal load. The fundamental wave frequency carries 98.0 %, and the rest of the harmonic components under 1 kHz carry 0.26 % of the total power under 20 kHz.

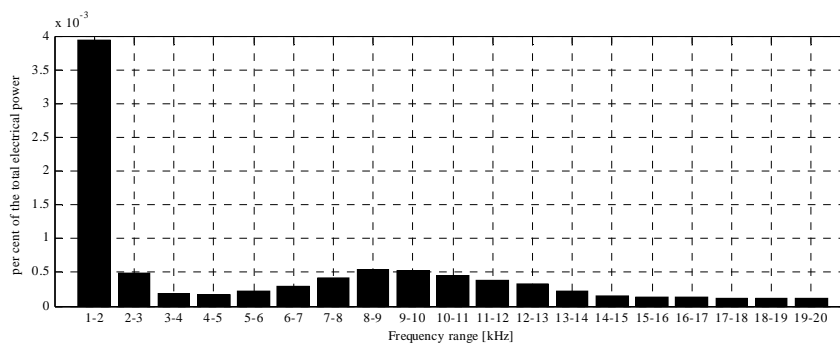


Fig 5.3. Electrical power as a function of frequency with a sinusoidal supply. The fundamental wave power is 99.669 % and the power of the rest of the harmonic components under 1 kHz is 0.322 %. The power of all the measured signals above 1 kHz is under 0.01 %. It should be noted that the y-axis scale is  $10^{-3}$  per cent.

Figures 5.1–5.3 show that the electrical power distribution is different with different PWM supply conditions, and naturally with a sinusoidal supply. The carrier frequency is clearly visible in the case of the DPWM, but the switching frequency of the DTC cannot be seen from the figure.

### 5.1 Spectra in the DTC

In the DTC, the average switching frequency is controlled by varying the flux linkage and torque hysteresis bands. The hysteresis bands are controlled by the reference switching frequency to achieve the desired average value. In the DTC, there is neither a predetermined switching pattern nor a priori knowledge of the harmonic contents of the voltages. The switching pattern is unique for different average switching frequencies, and in practice, for every possible case. The nonlinear control loops of the DTC make the harmonic analysis of the drive very complex compared with the classical PWM-controlled drives. Kaboli et al. (2006) introduced a probabilistic voltage harmonic analysis of a direct-torque-controlled drive, where

the probabilistic method is used to study the voltage spectrum of a DTC induction motor drive. However, their paper does not mention the different switching frequencies used in the analysis and there is no control of the switching frequency. In Casadei et al. (1994), the THD has been used to describe the harmonic behaviour of the stator current of the direct-torque-controlled induction motor.

The flux and torque estimate slopes can be analytically investigated, if the cycle time  $\Delta t$  of the control system is short enough, and we can assume that the differential of the stator flux linkage  $d\Psi_s/dt$  and the differential of the rotor flux linkage  $d\Psi_r/dt$  are constants during a cycle time. The stator and rotor flux linkages at a sampling instant  $t(k+1)$  are given by the following equations (Casadei et al., 1997)

$$\psi_s(k+1) = \psi_s(k) + \left( -\frac{R_s}{\sigma L_s} \psi_s(k) + \frac{R_s L_m}{\sigma L_s L_r} \psi_r(k) + U_s(k) \right) \Delta t \quad (5.1)$$

$$\psi_r(k+1) = \psi_r(k) + \left( \frac{R_r L_m}{\sigma L_s L_r} \psi_s(k) + \left( j\omega_m - \frac{R_r}{\sigma L_r} \right) \psi_r(k) \right) \Delta t \quad (5.2)$$

By rearranging (5.1) and (5.2), the following relationships are obtained

$$\psi_s(k+1) = \psi_s(k) \left( 1 - \frac{R_s}{\sigma L_s} \Delta t \right) + \psi_r(k) \left( \frac{R_s L_m}{\sigma L_s L_r} \right) \Delta t + U_s \Delta t \quad (5.3)$$

$$\psi_r(k+1) = \psi_r(k) \left[ 1 + \left( j\omega_m - \frac{R_r}{\sigma L_r} \right) \Delta t \right] + \psi_s(k) \frac{R_r L_m}{\sigma L_s L_r} \Delta t \quad (5.4)$$

Equations (5.3) and (5.4) are the induction machine equations in the state-variable form, and they are valid for small values of  $\Delta t$ . The stator-side equation (5.3) shows that the stator flux linkage variation is dependent on the machine parameters, the applied voltage vector and the operating condition of the motor. The operating condition effects are due to the variation of the rotor flux linkage and machine parameters (e.g. temperature and slip). If the stator resistance effects are neglected, (5.3) reduces to

$$\psi_s(k+1) = \psi_s(k) + U_s \Delta t \quad (5.5)$$

The electromagnetic torque of the induction machine at the  $(k+1)^{\text{th}}$  sampling instant can be written as

$$T_e(k+1) = p \frac{L_m}{\sigma L_r L_s} [\psi_s(k+1) \cdot j \psi_r(k+1)] \quad (5.6)$$

Substituting (5.3) and (5.4) into (5.6) and neglecting the terms proportional to the square of  $\Delta t$ , Equation (5.6) can be rewritten as

$$T_e(k+1) = T_e(k) - T_k(k) \left( \frac{1}{\sigma L_s L_r} + \frac{1}{\sigma L_s L_r} \right) \frac{\Delta t}{2} + p \frac{L_m}{\sigma L_s L_r} [(U_s(k) - j\omega_m \psi_s(k)) \cdot j\psi_r(k)] \Delta t \quad (5.7)$$

Equation (5.7) can be divided into two parts; the first part is due to the machine parameters and it is always negative, reducing the absolute value of the torque. The first part is independent of the motor speed and the stator voltage. The second part represents the effect of the applied stator voltage to the electromagnetic torque and it is dependent on the operating condition of the motor. The ascending and descending torque slopes during an active vector can be approximated by Equation (5.7). In Kang and Sul (2001), it is shown that the first part of Equation (5.7) is negligibly small, and the ascending torque slope can be given as

$$S_T^+ = p \frac{L_m}{\sigma L_s L_r} [(U_s(k) - j\omega_m \psi_s(k)) \cdot j\psi_r(k)] \Delta t, \quad (5.8)$$

and the descending torque slope

$$S_T^- = p \frac{L_m}{\sigma L_s L_r} [j\omega_m (\psi_s(k) \cdot j\psi_r(k))] \Delta t. \quad (5.9)$$

The ascending and descending flux slopes can be solved from (5.5), (Kang and Sul, 2001)

$$S_F^+ = \frac{\Psi_s(k+1) - \Psi_s(k)}{\Delta t} = \frac{+\Delta \Psi_s(k)}{\Delta t} \quad \text{and} \quad (5.10)$$

$$S_F^- = \frac{\Psi_s(k+1) - \Psi_s(k)}{\Delta t} = \frac{-\Delta \Psi_s(k)}{\Delta t}. \quad (5.11)$$

The flux slopes are dependent on the stator flux linkage location. The analytical investigation leads to sinusoidal functions with respect to the stator flux linkage angle, and the behaviour of the flux linkage is highly nonlinear (Kang and Sul, 2001). This analytical investigation shows that the voltage spectrum of the DTC is affected by the following: the desired average switching frequency, the torque and flux hysteresis controller bands, the operating condition of the machine (speed and load), the machine parameters and the intermediate circuit DC link voltage. In the analytical investigations, we have to assume for instance that the flux linkage or torque slopes are constant and they are travelling between the hysteresis bands, the sample time is infinitesimally small, and the machine parameters are constant and independent of the operating condition of the motor. In Fig 5.4 typical waveforms of the estimated electric torque (not the mechanical torque on the axis) and flux linkage in the DTC control are shown. The waveforms in Fig 5.4 are obtained by simulation at a 25 Hz operating point, and it can be clearly seen that these assumptions are not correct.

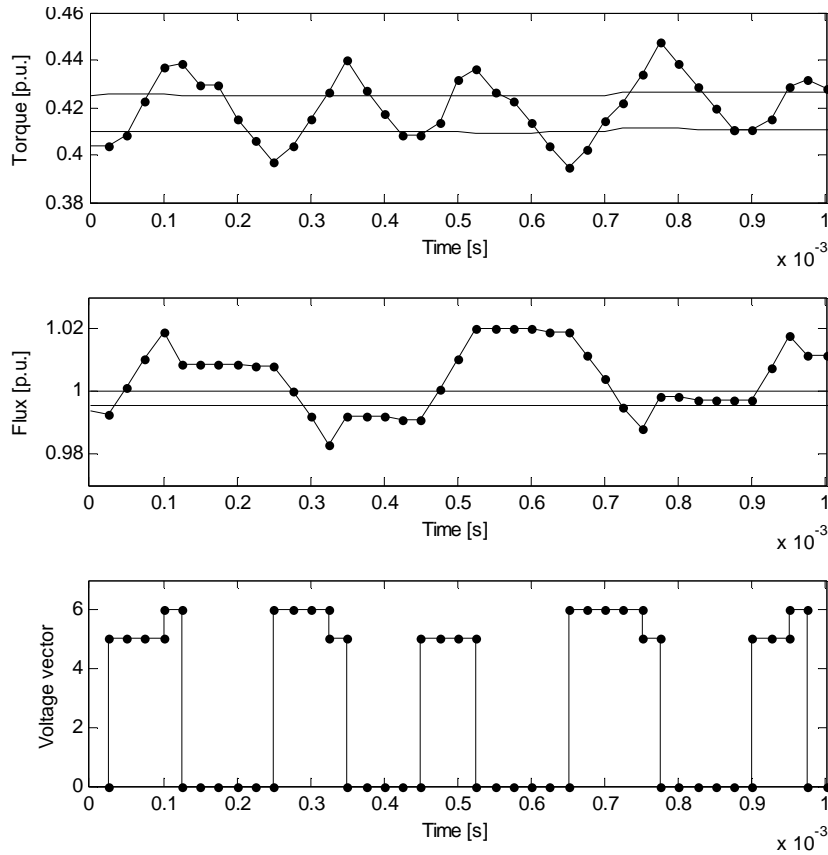


Fig 5.4. Typical waveforms of the estimated torque and the estimated flux travelling between the hysteresis limits in the DTC-controlled induction motor. The estimated stator flux linkage vector lies in sector 3.

From the control engineering point of view, an electrical machine is a voltage-controlled current source. The losses of the motor are dependent on the amplitude and frequency of the current components. The voltage coupled to the machine terminal produces the current through the machine impedance. The different voltage waveforms produce different current waveforms, and the best way to analyse the current is its spectrum. In the DTC, the current spectrum is different depending on the combinations of the torque and flux hysteresis bands, while the average switching frequency is kept constant. The inverter switching frequency must be controlled to keep it in the desired and safe range. A low switching frequency produces distorted current, which in turn produces extra losses in the motor but low converter losses. A high switching frequency raises the temperature of the switching component to an undesired level. The switching frequency of the commercial PWM inverters can be as high as 20 kHz, but the factory default is in the range of 2 to 6 kHz. The rated currents of the commercial frequency converters are achieved only when the switching frequency is equal to or less than the factory default. Thus, the choice of high switching frequency leads to a larger, more expensive frequency converter.

The inverter switching frequency can be controlled to adjust the flux and torque hysteresis bands. The hysteresis bands must be chosen carefully to obtain the desired switching frequency and as low current distortion as possible. The desired average switching frequency can be

obtained with several torque and flux hysteresis bands ratios. Figures 5.5–5.7 illustrate three different cases of the effects of hystereses on the current spectra in the DTC.

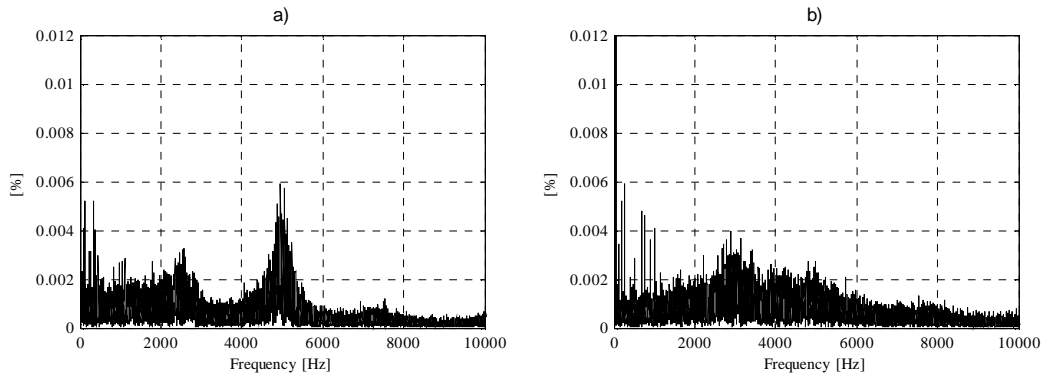


Fig 5.5. Simulated current spectra obtained with different rotational speeds and the same torque and flux linkage hysteresis bands. The fundamental wave amplitude is scaled outside of the figure. The torque hysteresis is set to 5 % of the nominal torque and the flux hysteresis is 1 % of the square of the nominal flux linkage. In a) the frequency reference is set to 20 Hz and in b) 40 Hz, respectively. The load torque is set to 50 per cent of the nominal load in both simulations. The average switching frequency for one-second period is 2206 Hz in **a** and 2246 in **b**.

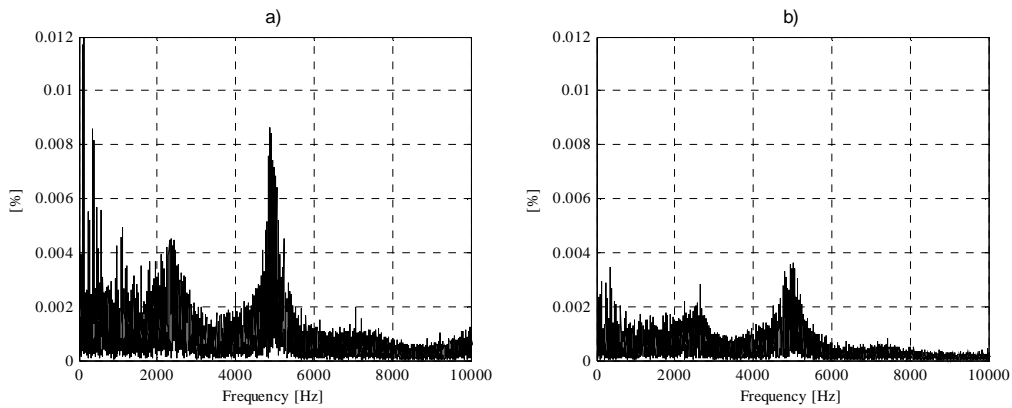


Fig 5.6. Simulated current spectra obtained with different load torques and the same torque and flux linkage hysteresis bands. The torque hysteresis is set to 5 % of the nominal torque and the flux hysteresis is 1 % of the square of the nominal flux linkage. The load torque is 20 and 80 per cent of the nominal load in a and b, respectively. The fundamental wave amplitude is scaled outside of the figure, the fundamental wave amplitude is 0.396 p.u. in **a** and 0.767 p.u. in **b**. The average switching frequency for one-second period is 2250 Hz in both cases.

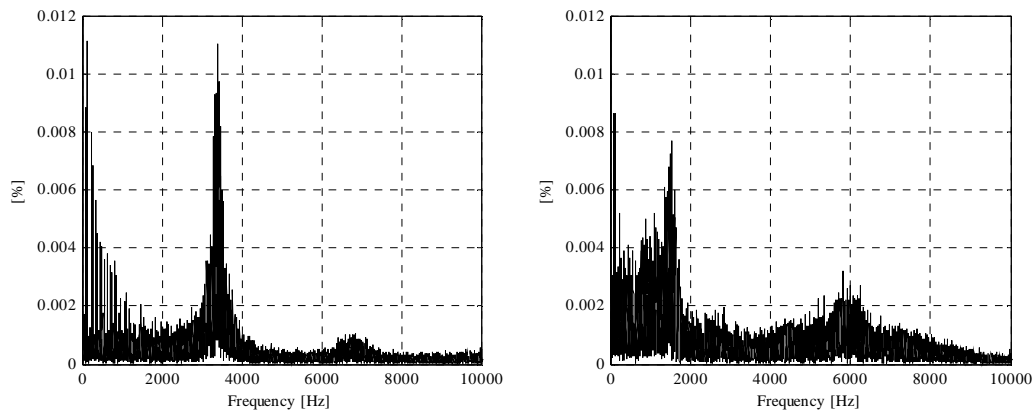


Fig 5.7. Simulated current spectra obtained with different torque and flux linkage hysteresis ratios. The fundamental wave amplitude (0.555 p.u.) is scaled outside of the figure. The average switching frequency is 2500 Hz in both simulations. In a) the torque hysteresis is set to 10 % of the nominal torque and the flux linkage hysteresis is zero, and in b) the torque hysteresis is 3 % and the flux linkage hysteresis is 2 % of the square of the nominal flux linkage. The operation points of the 37 kW motor in simulations were 20 Hz and 50 per cent of the nominal load. a)  $TD_{20000} = 7.12\%$  ( $THD_{50} = 1.64\%$ ), b)  $TD_{20000} = 7.51\%$  ( $THD_{50} = 1.42\%$ ).

## 5.2 Effect of current measurement delay in the DTC

In a direct-torque-controlled drive, the current measurement delay affects strongly the current harmonics distribution in the switching frequency range. As noted earlier, in the DTC the average switching frequency is controlled by flux and torque hysteresis bands. The hysteresis bands are controlled by the reference switching frequency to achieve the desired average value. The effects of the current measurement delay on the current spectrum are illustrated in Fig 5.8. The simulation results in Fig 5.8 show how the current harmonic spike originating from the switching frequency, which is at higher frequency than the average switching frequency, moves to lower frequencies as the current measurement delay gets longer.

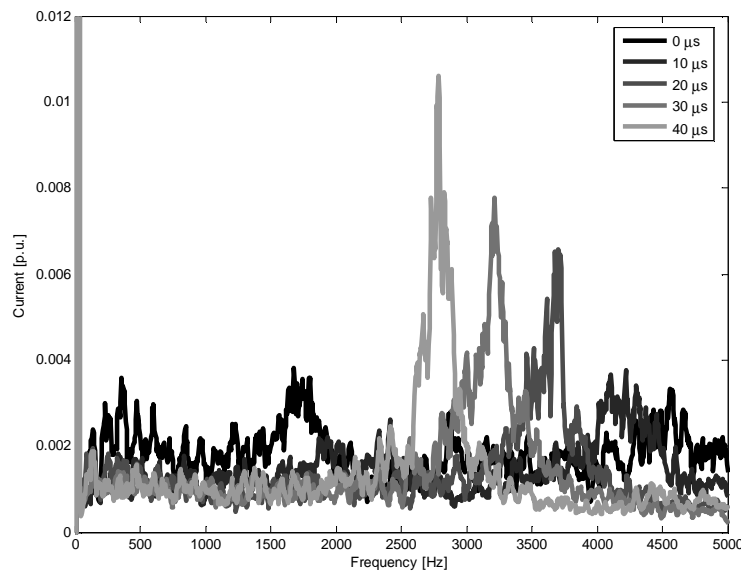


Fig 5.8. Effect of the current measurement delay on the phase current spectra. The simulation results are obtained with the analytical motor model. The frequency reference of the converter is 20 Hz and the average switching frequency is 2000 Hz. The fundamental current component is 0.69 p.u.

The shift in the current spectrum spike originating from the switching frequency results from the fact that the current used to calculate the estimate of the torque is delayed. In Fig 5.9 the behaviour of the torque estimate is shown with different current measurement delays. In all simulations, the torque hysteresis is set to zero, and the flux linkage hysteresis is 2 % of the square of the nominal flux linkage to get a practical value for the average switching frequency.

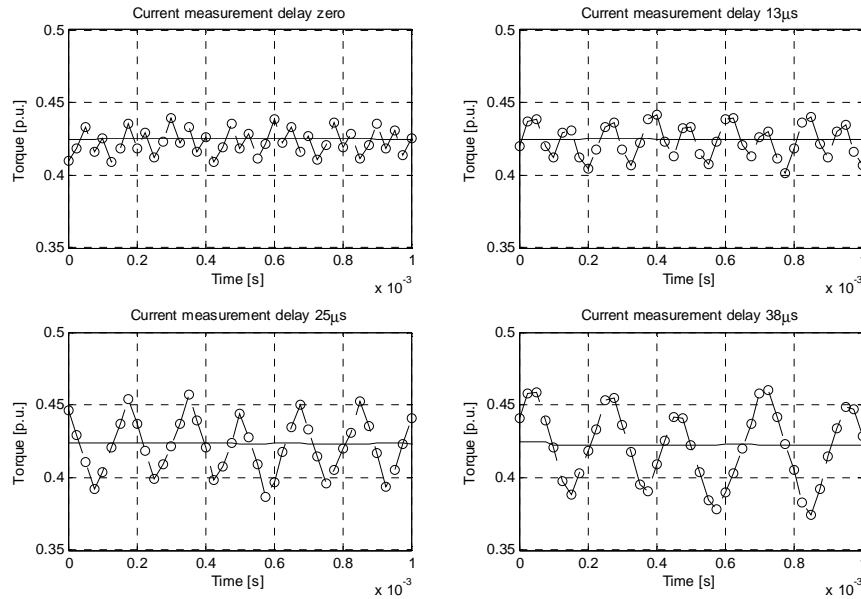


Fig 5.9 Behaviour of the torque estimate with different current measurement delays. With constant hystereses, the current measurement delay determines the switching frequency. When the current measurement delay is zero, the switching frequency is 5.4 kHz; with a 13  $\mu\text{s}$  delay the switching frequency is 3.5 kHz, with a 25  $\mu\text{s}$  the switching frequency is 2.5 kHz, and finally, with a 38  $\mu\text{s}$  the delay is 2 kHz. The torque reference is also shown in the figure.

When the current measurement delay is zero, the torque estimate changes the direction instantly after crossing the hysteresis line. When the current delay gets longer, the torque estimate continues to travel in a wrong direction even though the hysteresis has been crossed. When the hysteresis line is crossed, the control system is using zero vectors to reduce the torque and to keep it within the hysteresis limits. The torque estimate is travelling in the wrong direction because of the delayed current that the control system is using to calculate the torque estimate, despite the fact that the real current in motor is decreasing due to the zero vectors. The hysteresis control is selecting the optimal value for the torque and flux bands, and this error in the current measurement forces the hysteresis control to tighten the torque hysteresis band to achieve the desired average switching frequency. This results in different torque and flux linkage hysteresis band ratios and changes the frequency of the current spectrum spike originating from the switching frequency.

### Switching frequency limitation

In addition to the fact that the current measurement delay changes the spectrum of the DTC, it also limits the maximum switching frequency of the DTC converter. The maximum average switching frequency reference of the DTC converter used here is 4 kHz. When the hystereses are set to a zero level, the current measurement delay is limiting the maximum switching frequency that can be met. The simulated and measured maximum average switching frequencies of the 37 kW motor are shown in Fig 5.10. The motor load has almost no effect on the maximum average switching frequency. The measurement shows that from 900 to 1350  $\text{min}^{-1}$  the drive can reach the requested switching frequency, but when the motor rotational speed is 1500  $\text{min}^{-1}$  or less than 750  $\text{min}^{-1}$ , the requested switching frequency cannot be

achieved. The simulation results are shown with different current measurement delays. It can be seen in Fig 5.10 that in the simulation, similar behaviour of the maximum switching frequency can be obtained with a current measurement delay of about 30  $\mu\text{s}$ .

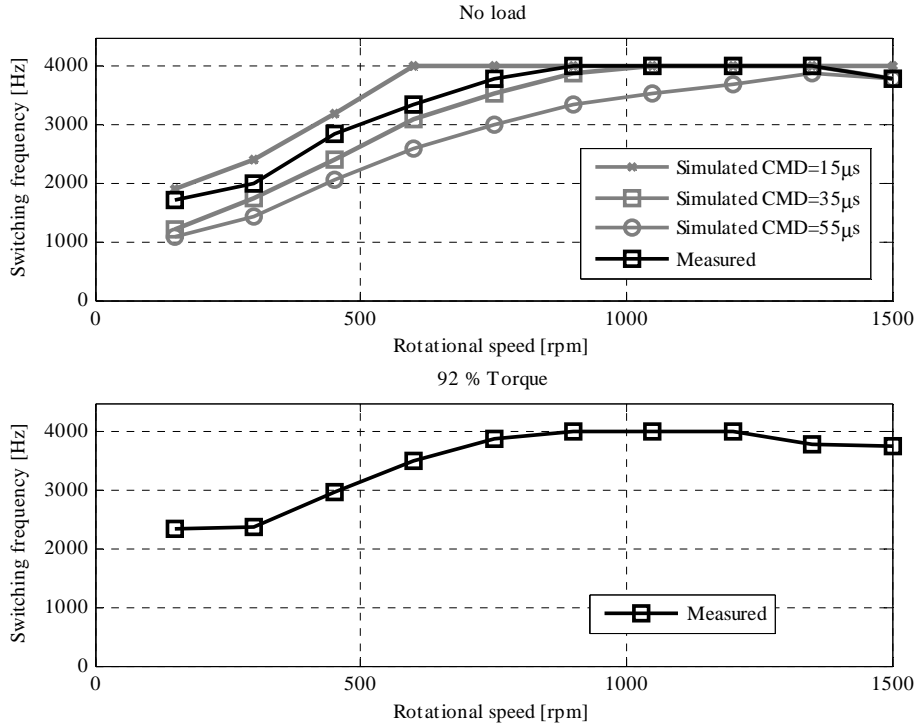


Fig 5.10 Maximum average switching frequency of the DTC converter as a function of motor rotational speed. The motor load has almost no effect on the maximum switching frequency.

### 5.3 Analysis of the measured data

The measurements for spectra comparisons were made with a 1  $\mu\text{s}$  sample time and one second record length, thus resulting in one million data points for each phase voltage and current. From the measured voltage, the common-mode voltage is removed before performing the DFT to reduce the noise produced by the measuring system and the fluctuation of the neutral point. The common-mode voltage can be calculated as

$$u(t)_{\text{common}} = \frac{u_u(t) + u_v(t) + u_w(t)}{3}, \quad (5.12)$$

where  $u_u$ ,  $u_v$  and  $u_w$  are the measured phase voltages at the motor terminals. Figure 5.11 illustrates the measured phase voltage and the same phase voltage after the common-mode voltage has been removed. The DFT analyses have been made with data decimated with a 25  $\mu\text{s}$  interval. The decimation point of the phase voltage is carefully placed in the middle of the voltage pulse to remove the high-frequency switching transients from the voltage before the

analysis. The same decimation points are used also for the currents to obtain a low-distorted current for the analysis.

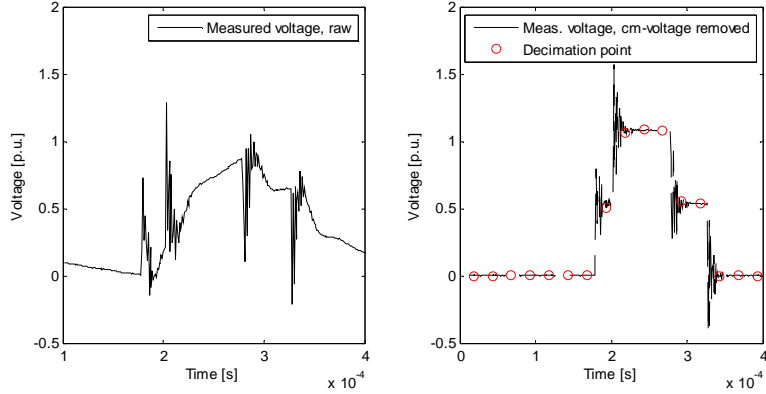


Fig 5.11. Measured voltage waveform as a function of time (left). Measured voltage after removing the common-mode voltage and the decimation points at a 25  $\mu$ s interval (right).

#### 5.4 Calculating the switching frequency and voltage vectors

In the classical PWM or in the space vector modulation, the switching frequency is determined by the carrier frequency. The switching frequency can be calculated analytically as in the case of the symmetrical two-phase modulation ( $f_{sw} = 2/3 f_{carrier}$ ), but this is not always the correct value. The major difference between the analytical value and the real value is found when the switching frequency and rotational speed of the motor are high. As mentioned above, the switching frequency is the easiest part in a frequency converter to adjust both the converter and the drive system losses. In this thesis work, the switching frequency was calculated from the measured voltages to obtain an exactly correct value. After the switch states are solved, the exact voltage vectors that the modulator has been using during the measurement are determined. After that, the simulator modulator can be compared with the actual modulator. This paragraph demonstrates how the switching frequency is calculated from the measured three-phase voltages. The same 1 second 1 $\mu$ s data were used as in the spectra analysis.

##### Switching frequency

One leg of the inverter can be connected either to the upper DC bus or the lower DC bus. If these states are denoted  $S = 1$  and  $S = 0$ , respectively, one switching instant is

$$S(k+1) \neq S(k)$$

This means that two power devices have changed their states. If all switching instants in three phases are averaged over a time period and divided by the number of power devices, we get the average value of the switching frequency for one of the inverter power devices. The value of the switching frequency describes the real amount of switching instants over a time period, and it is independent of the modulation method used.

In the DTC, the switching frequency has an active control, and the actual switching frequency is very close to the reference. The instantaneous switching frequency can vary depending on the location of the flux linkage (estimate) in the sector, Fig 5.12 and during transients, but in a continuous state the average switching frequency is constant. If the value of the switching reference is set too high, it may not be reached and the actual switching frequency is lower than the reference.

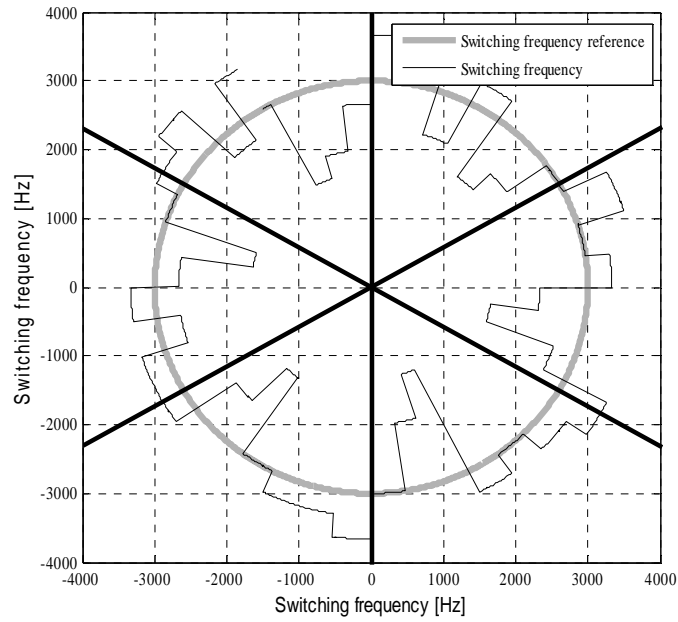


Fig 5.12. Switching frequency of the DTC plotted against the stator flux estimate angle (distance from the origin). The switching frequency in the figure is calculated in 1 ms time windows. The switching frequency reference is set to 3000 Hz in this case.

Traditionally in the PWM, there is no control over the switching frequency, and the switching frequency  $f_{sw}$  is inversely proportional to the sample time  $T_s$  of the modulator

$$f_{sw} = \frac{1}{2T_s} . \quad (5.13)$$

Therefore, the switching frequency is constant. At very low or high speeds and close to the sector borders, the minimum pulse length affects the switching frequency. In normal conditions, the modulator changes the state of one throw-over switch at a time. Thus, dropping one active vector (or zero vector) out of the modulation sequence leads to a double switching and the switching frequency remains unchanged. If the minimum pulse limitation cancels out two of the three vectors (or two of the four, depending on the modulation pattern), the switching frequency is changed lower.

The switching frequency can be calculated using the measured three-phase voltages. First, the common-mode voltage has to be removed. The switching noise can be removed by filtering the

voltage. A low-pass filter for instance with a cut-off frequency of 20 kHz can be used. After removing the common-mode-voltage and low-pass filtering the voltage, the switch states are clearly visible in the measured voltage. Using the stator coordinate voltages instead of phase voltages, the comparable data reduce from three to two vectors, Fig 5.13. Comparing the voltage levels of the  $x$ - and  $y$ -components, the voltage vectors at different time instants can be solved. Because the measurement device is not synchronized to the modulation period, during the time instants, when the switch state is changed, there are also voltage values that do not present any of the seven discrete voltage vectors that can be produced with a two-level inverter bridge. The amount and duration of these voltage values are very limited, and they can be set to present the previous voltage vector that is recognized, without affecting the switching frequency. If there is a desire to use the switch states in a VSD simulation, the transient states should be analysed more carefully. The zero voltage can be produced with a switch combination where all the inverter legs are connected to the lower DC bus, the voltage vector  $\mathbf{u}_0$  (0, 0, 0) or the upper DC bus, the voltage vector  $\mathbf{u}_7$  (1, 1, 1). The zero vectors can be detected examining the common-mode-voltage level, Fig 5.14. It is clearly seen that during the zero vector  $\mathbf{u}_7$ , the average value of the measured common-mode voltage is over zero, and during the zero vector  $\mathbf{u}_0$ , the common mode voltage is below zero volts. The common mode voltage depicted in Fig 5.14 is measured against the motor ground.

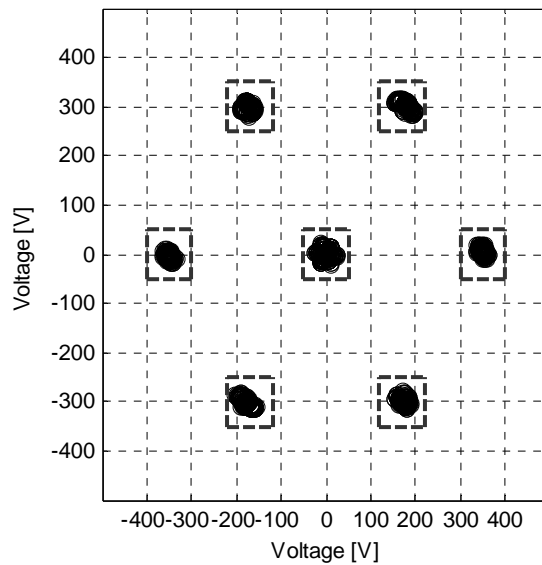


Fig 5.13. Measured voltage waveform in stationary coordinates after removing the common-mode voltage and switching noise. The rectangles represent the acceptable variation in the voltage levels of the recognizable voltage vectors.

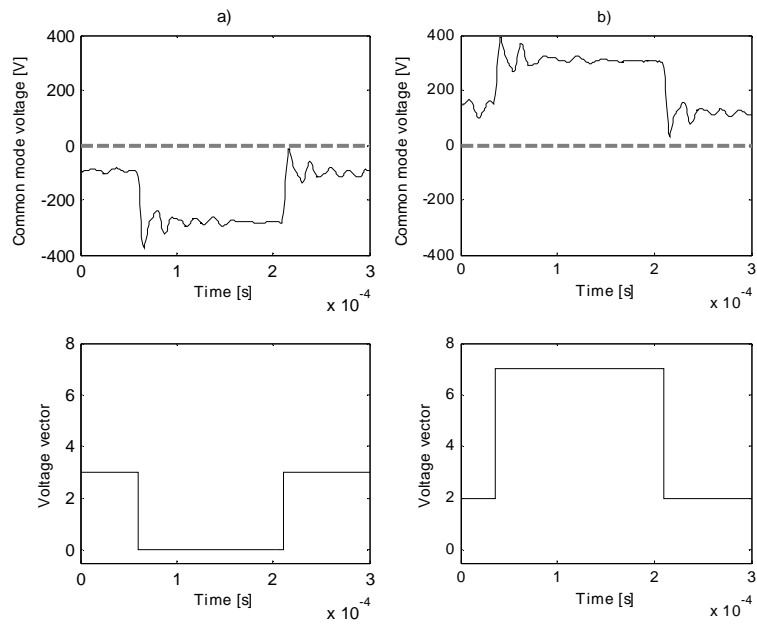


Fig 5.14. Measured common-mode voltages during zero vectors. a) Voltage vector  $\mathbf{u}_0$  (0, 0, 0) and b) voltage vector  $\mathbf{u}_7$  (1, 1, 1)

### 5.5 Spectrum analysis with the analytical and the FEM motor model

The spectra figures with different switching frequencies at the 25 Hz operating point with a load equal to 92 % of the nominal torque of the 37 kW induction motor are given in Appendix C. Here, the results are discussed, and the reference switching frequency spectra are illustrated in Fig 5.15–5.18.

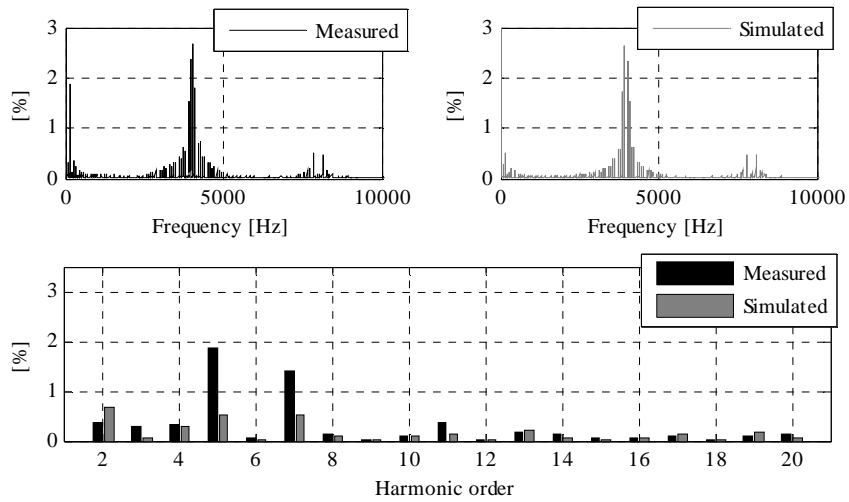


Fig 5.15. Spectra of the measured motor phase currents of the 37 kW induction motor and simulated with the analytical model. The vector control carrier frequency is set to 4000 Hz. The fundamental wave (25 Hz) is scaled outside the figure.

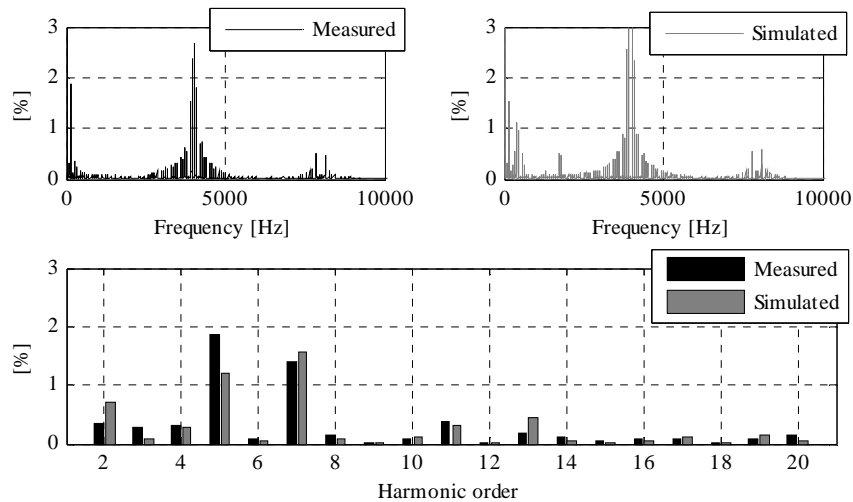


Fig 5.16. Spectra of the measured motor phase currents of the 37 kW induction motor and simulated with the FEM. The vector control carrier frequency is set to 4000 Hz. The fundamental wave (25 Hz) is scaled outside the figure.

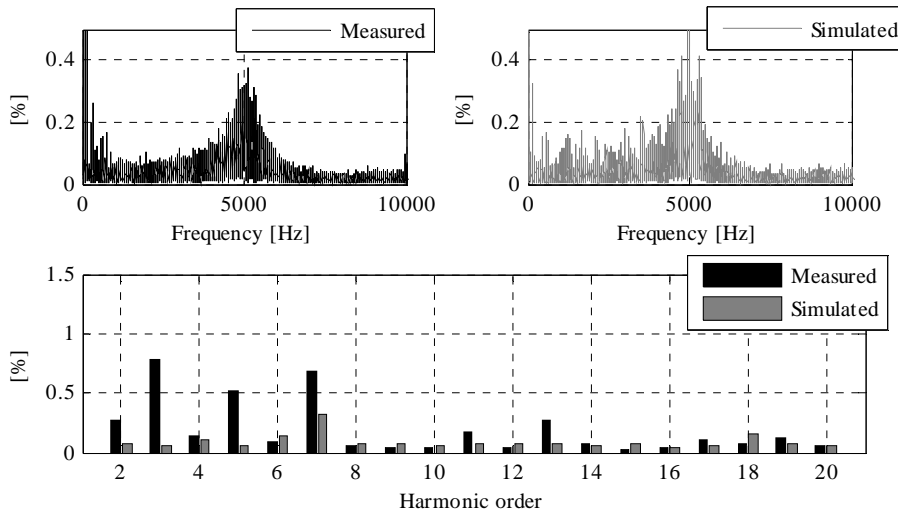


Fig 5.17. Spectra of the measured motor phase currents of the 37 kW induction motor and simulated with the analytical model. The switching frequency reference of DTC is set to 3000 Hz. The fundamental wave (25 Hz) is scaled outside the figure.

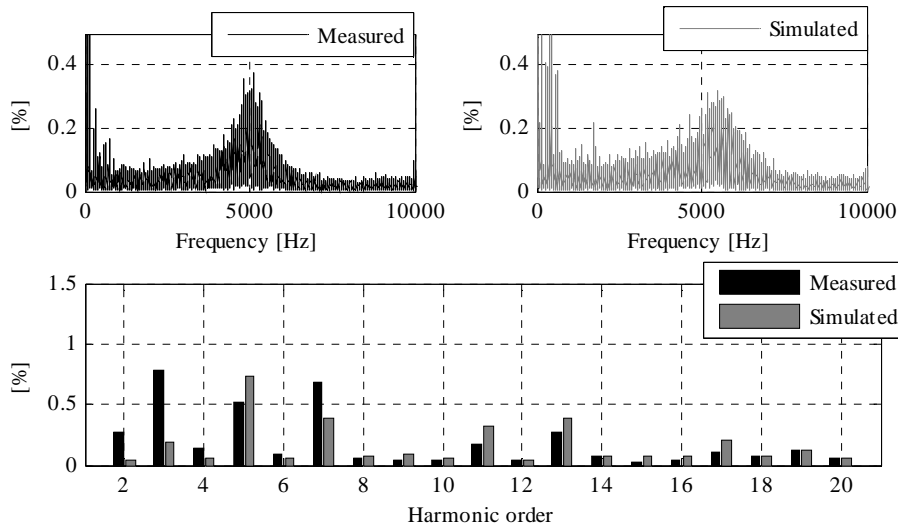


Fig 5.18. Spectra of the measured motor phase currents of the 37 kW induction motor and simulated with the FEM motor model. The switching frequency reference of DTC is set to 3000 Hz. The fundamental wave (25 Hz) is scaled outside the figure.

The Fig 5.15-5.18 shows that both motor models can be used in the simulations to obtain current spectra that are comparable to the measured ones. The motor model based on FEM program models the harmonics produced by machine construction. The 5<sup>th</sup>, 7<sup>th</sup>, 11<sup>th</sup> and 13<sup>th</sup> current harmonic component amplitudes are close to measured ones in FEM simulations. When analytical motor model is used, the amplitudes of these current harmonic components are too small.

In Figs 5.19–5.22, the measured current spectra are compared with the simulated current spectra with average switching frequencies of 1000, 1500, 2000 and 2500 Hz. A 200 kW commercial DTC converter is driven with a 25 Hz frequency reference. The load torque was set to 64 % of the nominal load torque of the motor. The details of the 200 kW test setup are given in Appendix A. The FEM-model-based simulations have been carried out with 25 $\mu$ s time steps, which is the same as the control system cycle time in this thesis.

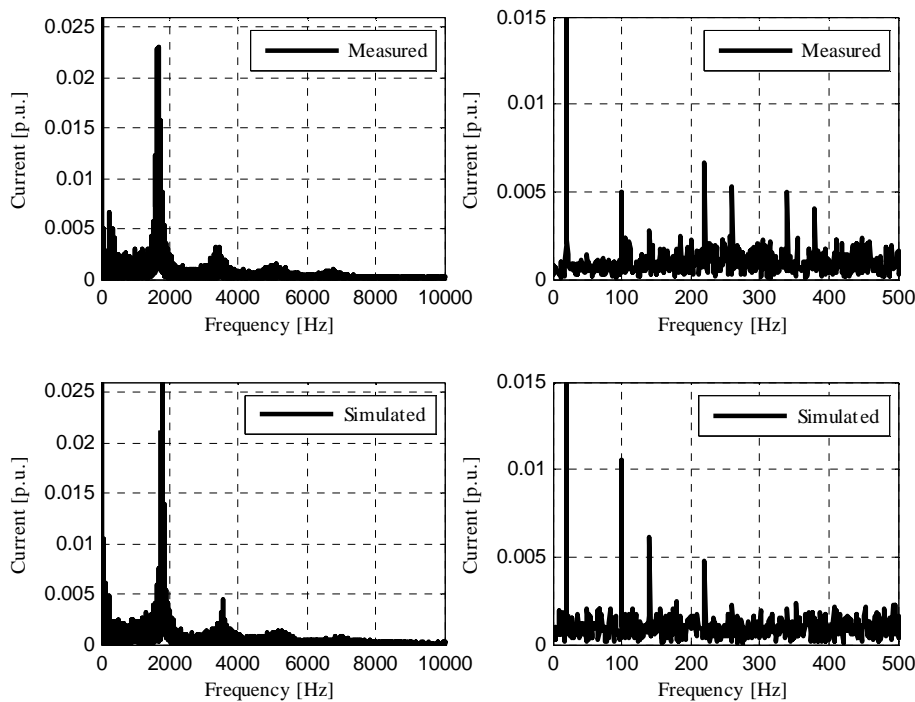


Fig 5.19. Spectra of the simulated and measured motor phase currents of the 200 kW induction motor used in the tests. The switching frequency reference is set to 1000 Hz. The fundamental wave (20 Hz) is scaled outside the figure.

With a 1000 Hz average switching frequency, the fundamental wave amplitudes are 0.699 p.u. for the simulated and 0.695 p.u. for the measured currents, respectively. The simulated current spectrum has a correct shape in the frequency domain (left side of the Fig. 5.19). When the lower-frequency harmonic content is examined (right side of the Fig. 5.19.), in the simulated results, the 5<sup>th</sup> (100 Hz) and the 7<sup>th</sup> (140 Hz) harmonic amplitudes are larger than the measured ones. The 11<sup>th</sup> (220 Hz) harmonic amplitude is smaller in the simulated results than in the measured ones. In the simulated results, the 13<sup>th</sup> (260 Hz), 17<sup>th</sup> (340 Hz) and 19<sup>th</sup> (380 Hz) harmonics are almost totally missing, although they are clearly visible in the measured results. When the switching frequency reference is set to 1500 Hz, in the simulated current spectrum, the spike originating from the switching frequency is at the correct frequency but has a lower amplitude than in the measured ones (left side of the figure). In the simulated results, the 5<sup>th</sup> (100 Hz) and the 7<sup>th</sup> (140 Hz) harmonic amplitudes are larger than in the measured ones. The

11<sup>th</sup> (220 Hz) and 13<sup>th</sup> (260 Hz) harmonic amplitudes are smaller in the simulated results than in the measured ones. The 17<sup>th</sup> (340 Hz) and 19<sup>th</sup> (380 Hz) correspond well to the measurements.

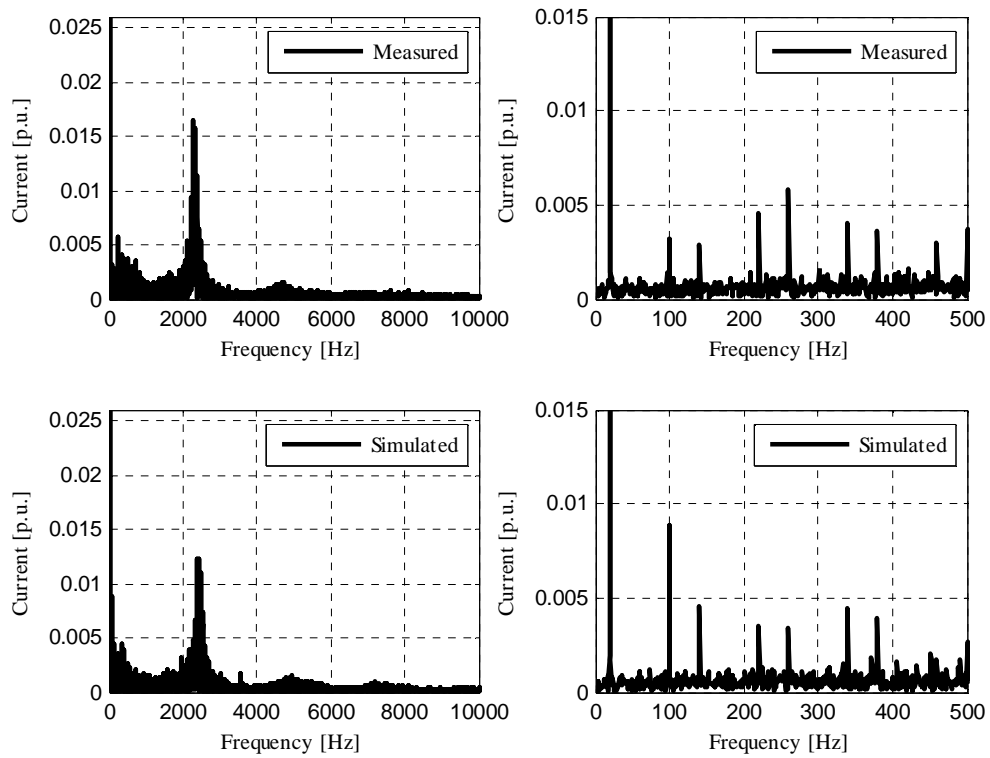


Fig 5.20. Spectra of the simulated and measured motor phase currents of the 200 kW induction motor. The switching frequency reference is set to 1500 Hz. The fundamental wave (20 Hz) is scaled outside the figure, the fundamental wave amplitudes are 0.700 p.u. for the simulated and 0.695 p.u. for the measured current, respectively.

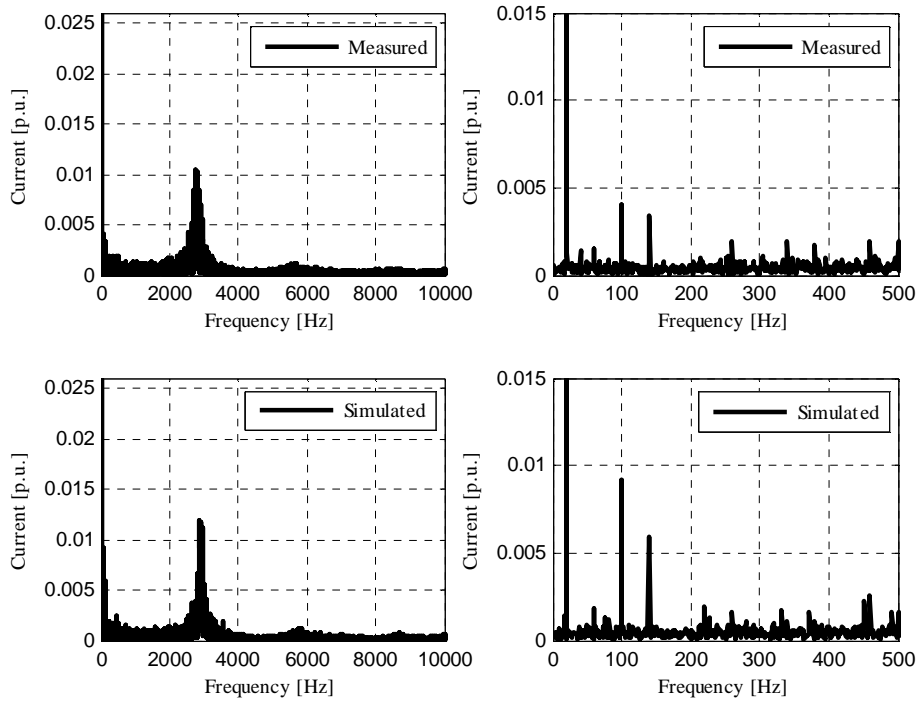


Fig 5.21. Spectra of the simulated and measured motor phase currents of the 200 kW induction motor. The switching frequency reference is set to 2000 Hz. The fundamental wave (20 Hz) is scaled outside the figure, the fundamental wave amplitudes are 0.700 p.u. for the simulated and 0.695 p.u. for the measured current, respectively.

In the simulated current spectrum, the spike originating from the switching frequency is at the correct frequency (left side of Fig 5.21). In the simulated results, the 5<sup>th</sup> (100 Hz) and 7<sup>th</sup> (140 Hz) harmonic amplitudes are larger than the measured ones. The 11<sup>th</sup> (220 Hz), 13<sup>th</sup> (260 Hz), 17<sup>th</sup> (340 Hz) and 19<sup>th</sup> (380 Hz) harmonic amplitudes are low both in the simulated and measured results.

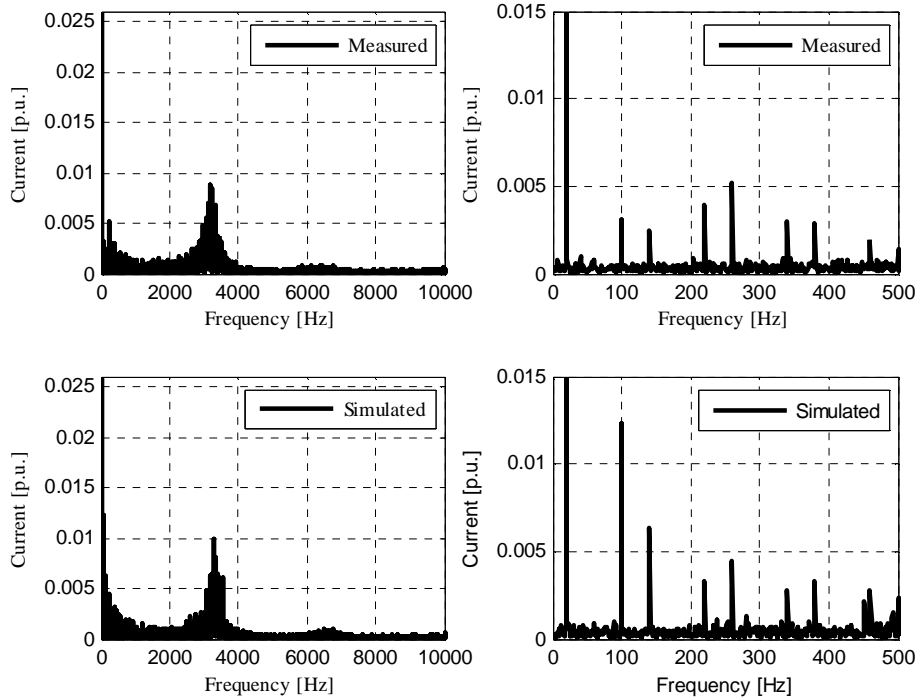


Fig 5.22. Spectra of the simulated and measured motor phase currents of the 200 kW induction motor. The switching frequency reference is set to 2500 Hz. The fundamental wave (20 Hz) is scaled outside the figure. The fundamental wave amplitudes are 0.700 p.u. for the simulated and 0.695 p.u. for the measured current, respectively.

In Fig 5.22, in the simulated current spectrum, the spike originating from the switching frequency is at the correct frequency (left side of the figure). In the simulated results, the 5<sup>th</sup> (100 Hz) and 7<sup>th</sup> (140 Hz) harmonic amplitudes are larger than the measured ones. The 11<sup>th</sup> (220 Hz), 13<sup>th</sup> (260 Hz), 17<sup>th</sup> (340 Hz) and 19<sup>th</sup> (380 Hz) harmonics correspond well to the measured results.

## 5.6 Effect of the time step length in the FEA of the frequency-converter fed IM

One problem in the finite element analysis is the calculation time. Here, the effect of the time step length in the FEA is examined. The calculation time analysis is performed with a standard desktop PC equipped with a 3.33 GHz Intel Core 2 Duo processor and 4 gigabytes of RAM. The simulation efficiency is given as

$$\text{Simulation efficiency} = \frac{\text{Real time of simulation} \left[ \frac{\text{r(s)}}{\text{s(s)}} \right]}{\text{Simulation time} \left[ \frac{\text{r(s)}}{\text{s(s)}} \right]} \quad (5.14)$$

First in this section, the calculation times of the FEM simulations with different time steps are examined and the simulation results are analysed. Then, the results obtained with the FEM are

compared with the hybrid calculation, where the analytical motor model is used between the FEM time steps. The stator current magnitudes in the frequency domain, the harmonic distortion of the currents, and the FEM losses are taken as indicators of correct simulation results.

### Hybrid calculation

In the hybrid calculation, the analytical motor model is used between the FEM calculation time steps to calculate the simulated currents. The parameters for the analytical model are given in Appendix A. The FEM program returns the values of the stator flux and current components as well as the rotor angle in each time step. At the end of each time step, the analytical motor flux linkage and current components can set to be equal to the FEM quantities

$$\begin{aligned}
 \Psi_{s\alpha,an}(t_k) &= \Psi_{s\alpha,FEM}(t_k) \\
 \Psi_{s\beta,an}(t_k) &= \Psi_{s\beta,FEM}(t_k) \\
 i_{s\alpha,an}(t_k) &= i_{s\alpha,FEM}(t_k) \\
 i_{s\beta,an}(t_k) &= i_{s\beta,FEM}(t_k)
 \end{aligned} \tag{5.15}$$

The rotor flux components of the inverse  $\Gamma$ -equivalent circuit at a time instant  $t_k$  are

$$\begin{aligned}
 \Psi_{R\alpha}(t_k) &= \Psi_{s\alpha}(t_k) - i_{s\alpha}(t_k)\sigma L_s \\
 \Psi_{R\beta}(t_k) &= \Psi_{s\beta}(t_k) - i_{s\beta}(t_k)\sigma L_s,
 \end{aligned}$$

because the rotational speed of the motor is known, the system of equations (4.20) that describes the induction motor can be used to calculate the flux linkages and currents at the next time step  $t_{k+1}$ . Fig 5.23 shows the behaviour of the flux linkages and the  $\alpha$ -components of the currents in the hybrid calculation.

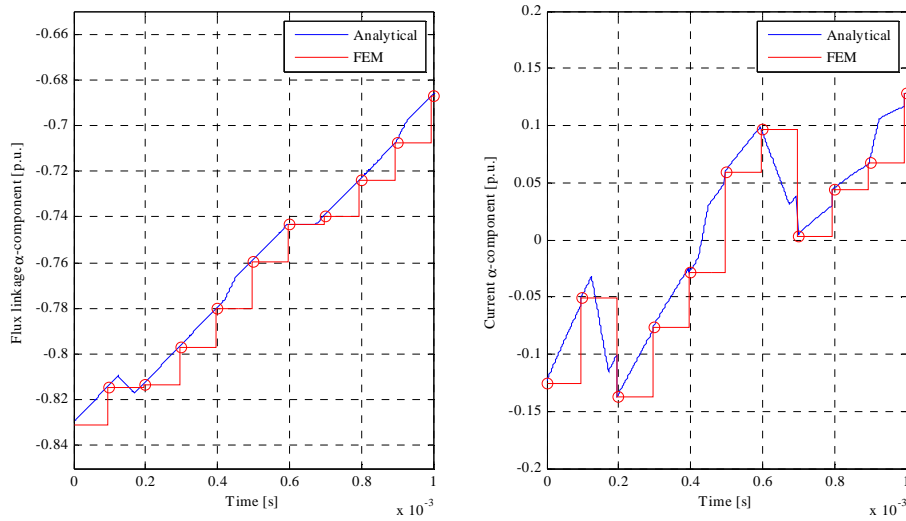


Fig 5.23. Behaviour of the  $\alpha$ -components of the current and flux linkages when the hybrid calculation method is used. The FEM motor model is calculated with  $100 \mu\text{s}$  time steps and the analytical motor model with  $1 \mu\text{s}$  time steps. The circles illustrate the points when analytical motor model quantities are set equal to the FEM quantities.

Fig 5.23 shows that the rates of change of the analytical model flux linkages and currents are similar to the FEM quantities. The changes in the analytical model currents between the FEM time steps are due to the fact that the voltage vectors are changing at a  $25 \mu\text{s}$  interval.

### 37 kW motor

As a case study, a 37 kW induction motor at an operating point with a 25 Hz frequency reference and 92 % load of the nominal torque was studied. The switching frequency reference was set to 3 kHz. In Fig 5.24, the current spectra of the simulations are compared. The current spectrum and losses obtained with a  $25 \mu\text{s}$  time step are fully comparable with the measured ones. When the FEM motor model is calculated with  $100 \mu\text{s}$  alone, it should be noted that this time the current remains at a stationary value until the next FEM calculation is carried out.

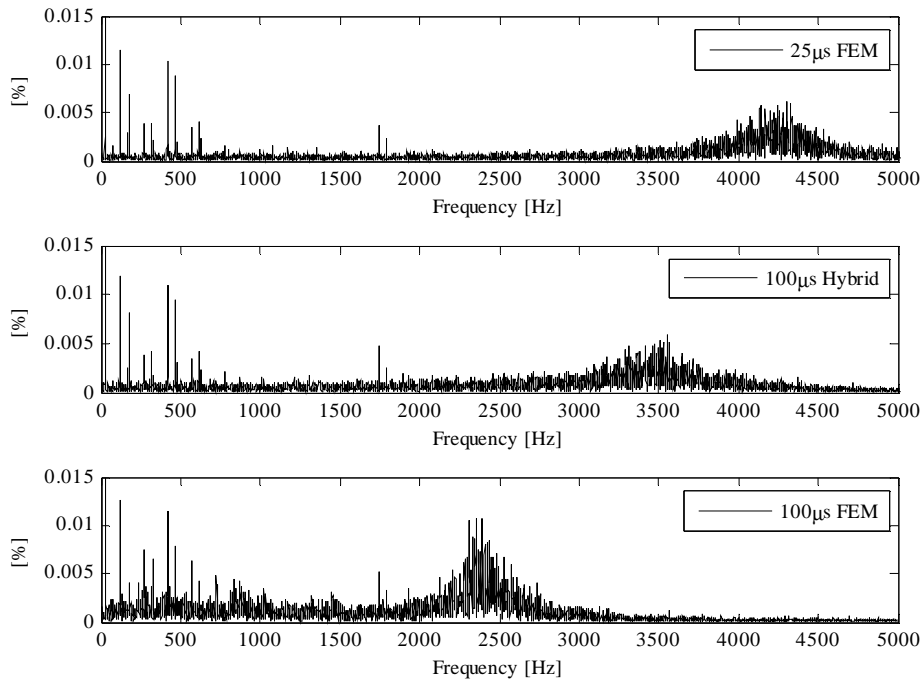


Fig 5.24. Simulated phase current spectra of the 37 kW induction motor when a 3 kHz DTC supply is used. The operation point of the motor is 25 Hz and 92 % of the nominal load.

The current spectra in Fig 5.24 show that the hybrid calculation improves the simulation accuracy compared with the pure 100  $\mu$ s FEM simulation. When the position of the spike originating from the switching frequency is moved from 4250 Hz to 3500 Hz, the difference with the pure 100  $\mu$ s FEM calculation is even more significant. The low-level harmonic amplitudes such as the 5<sup>th</sup>, 7<sup>th</sup>, 11<sup>th</sup>, 13<sup>th</sup>, 17<sup>th</sup> and 19<sup>th</sup> remain unchanged when the hybrid calculation is used. In the pure 100  $\mu$ s FEM simulation, the 7<sup>th</sup> current harmonic amplitude is only 50 % and the 11<sup>th</sup> and 13<sup>th</sup> current harmonic amplitudes are 100 % larger compared with the 25  $\mu$ s calculation. The simulation efficiency is 1800 r(s)/s(s) for the 25  $\mu$ s time steps and 480 r(s)/s(s) for the 100  $\mu$ s calculation, and the analytical model calculation has no effect on the calculation efficiency. The THD values of the phase currents and the simulated motor losses are listed in Table 5.1. The THD values show that the pure FEM calculation gives a more distorted current than the hybrid calculation. This is also visible in the simulated copper losses in the rotor. In Fig 5.25, the current spectra of the simulations with a 200  $\mu$ s calculation time step are compared. The maximum frequency that can be analysed with the DFT is now 2.5 kHz ( $1/(2 \times 200 \times 10^{-6})$ ).

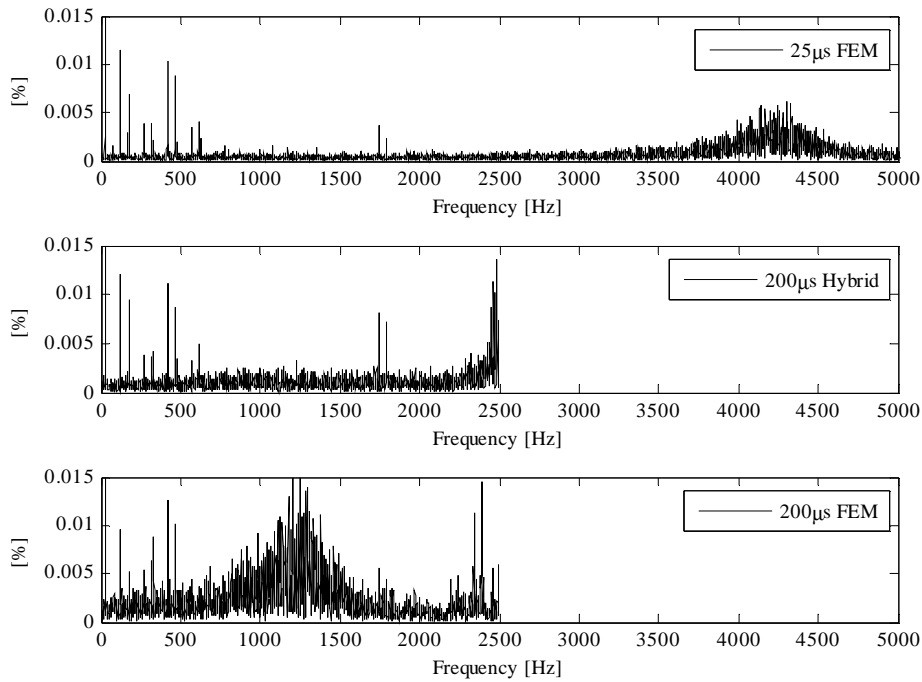


Fig 5.25. Simulated phase current spectra of the 37 kW induction motor when a 3 kHz DTC supply is used. The operation point of the motor is 25 Hz and 92 % of the nominal load torque.

The simulation efficiency is 210 r(s)/s(s) for the 200  $\mu$ s time step simulation. The DFT analysis cuts the frequency band to 2.5 kHz, and thus, in the hybrid calculation the switching frequency phenomena are no longer visible. The part of the current spectra that can be analysed is more correct in the hybrid calculation than with the pure FEM calculation. The loss results and the THD values of the phase currents with 200  $\mu$ s are given in Table 5.1.

Table 5.1. Losses obtained with different FEM motor model calculation time steps. H denotes hybrid calculation.

Quantity	25 $\mu$ s	100 $\mu$ s	100 $\mu$ s (H)	200 $\mu$ s	200 $\mu$ s (H)
Stator Copper Losses [W]	593	594	590	599	588
Stator Iron Losses [W]	349	264	263	248	228
Rotor Copper Losses [W]	480	472	430	479	400
Rotor Iron Losses [W]	142	97	96	86	76
Total loss [W]	1564	1427	1380	1412	1291
THD	1.51	2.11	1.64	2.83	1.92

The simulated motor losses in Table 5.1 seem to be closer to real losses without the hybrid calculation; even the current of the simulation is closer to real one with the hybrid calculation.

### 5.7 Effect of dead time in the simulation results

In a three-phase PWM inverter, the dead time phenomenon results in an increase in low-order harmonics such as the third, fifth, seventh and so on. The effect of the inverter dead time was studied using a 25 Hz frequency reference and the load torque was set to 92 % of the nominal load. The DTC converter switching frequency reference was set to 3 kHz and the carrier frequency of the VC converter was set to 4 kHz. The inverter dead time was varied from zero to 5  $\mu\text{s}$ . The inverter dead time does not affect the spectra in the switching frequency range in the case of the DTC, but the spectra shapes remain stationary when the dead time varies. In the simulation study, the most significant changes in the harmonic amplitudes of the 5<sup>th</sup> and 7<sup>th</sup> current harmonics were found. The 5<sup>th</sup> and 7<sup>th</sup> current harmonic amplitudes in the case of the VC converter are illustrated in Fig 5.26 and the respective results in the case of the DTC are depicted in Fig 5.27. The harmonic amplitudes are shown as a percentage of fundamental waves. There is no dead time compensation method in the simulator available at present.

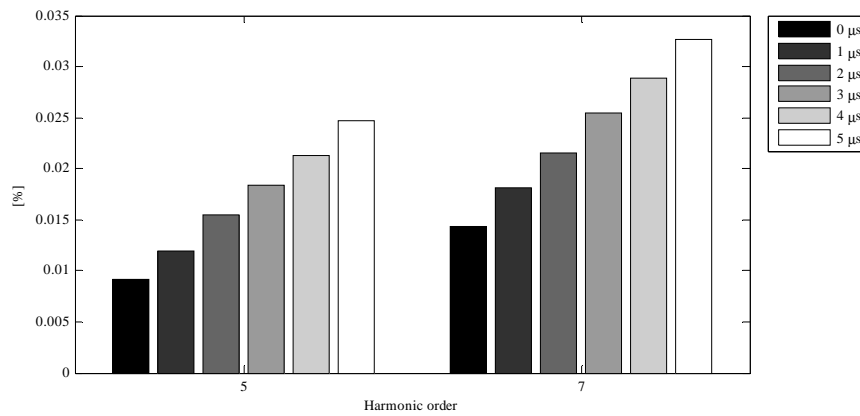


Fig 5.26. Simulated 5<sup>th</sup> and 7<sup>th</sup> harmonic amplitudes of the 37 kW induction motor with vector control. The inverter dead time was varied from 0 to 5  $\mu\text{s}$ .

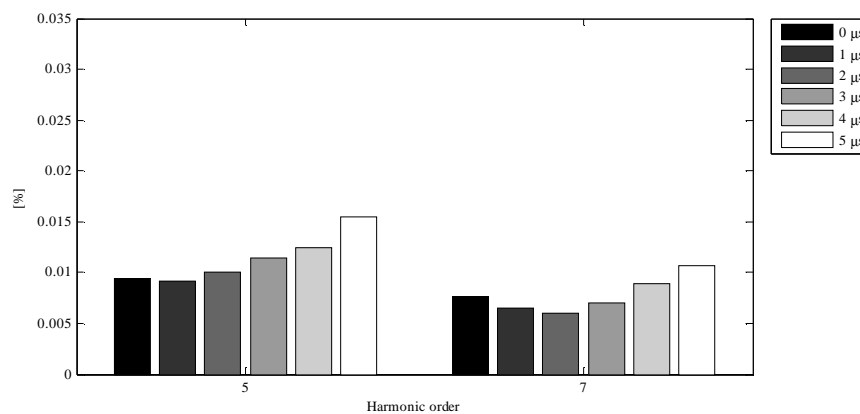


Fig 5.27. Simulated 5<sup>th</sup> and 7<sup>th</sup> harmonic amplitudes of the 37 kW induction motor with the DTC control. The inverter dead time was varied from 0 to 5  $\mu\text{s}$ .

In the case of the vector control, the results are clear. The 5<sup>th</sup> and 7<sup>th</sup> current harmonic amplitudes rise by 0.003–0.004 %, when the dead time is increased by 1  $\mu\text{s}$ . When the DTC control is used, the results are not so clear; the 5<sup>th</sup> harmonic amplitude is slightly lower with the 1  $\mu\text{s}$  dead time than with the zero dead time. With the dead times higher than 3  $\mu\text{s}$ , the 5<sup>th</sup> harmonic amplitude is increasing. Furthermore, the amplitude of the 7<sup>th</sup> harmonic is decreasing when the dead time is increased from zero to 1 or 2  $\mu\text{s}$ . The 7<sup>th</sup> harmonic amplitude is increasing linearly from 2  $\mu\text{s}$  to 5  $\mu\text{s}$ , although its amplitude is smaller with the 3  $\mu\text{s}$  dead time than with the zero dead time. The 5<sup>th</sup> harmonic amplitudes are almost equal in both cases with the zero dead time, 0.009 % of the fundamental. When the dead time is increased to 5  $\mu\text{s}$ , the amplitude of 5<sup>th</sup> harmonic is increased by 170 % in the vector control and only by 65 % in the DTC. The increase in the 7<sup>th</sup> current harmonics is 128 % and 41 %, respectively. This shows the difference in the control systems topologies; in the DTC, every voltage vector is selected independently using a fast 25  $\mu\text{s}$  control cycle, but in the vector control, the length of one modulation period is ten times as long, 250  $\mu\text{s}$  (4 kHz carrier). Although no dead time compensation methods are used here, the DTC has a natural ability to affect the harmonic content of the currents. The inverter dead time has an effect on the low-order harmonics, but its influence on the overall motor losses is almost negligible but detectable. The simulated copper losses, the THD and the TD values are shown in Table 5.2 and Table 5.3.

Table 5.2. Simulated stator and rotor copper losses and current distortion values with the vector control as a function of dead time.

Dead time	0	1	2	3	4	5
Copper loss stator [W]	614	614	614	615	615	616
Copper loss rotor [W]	506	508	509	511	513	515
THD [%]	1.43	1.69	2.07	2.39	2.72	3.09
TD [%]	8.71	8.93	9.13	9.42	9.69	10.07

Table 5.3. Simulated stator and rotor copper losses and current distortion values with the DTC control as a function of dead time.

Dead time	0	1	2	3	4	5
Copper loss stator [W]	591	592	592	593	594	594
Copper loss rotor [W]	477	478	478	480	481	483
THD [%]	1.35	1.32	1.32	1.49	1.72	2.02
TD [%]	7.51	7.60	7.57	7.69	7.71	7.90

The copper loss in the stator increases by 2 W when using the vector control, and by 3 W when the DTC control is used and the dead time is increased from zero to 5  $\mu\text{s}$ . The change in the copper losses of the rotor is more significant, 9 W in the vector control and 6 W in the DTC simulations. The THD and TD values indicate how much the value describing current distortion will rise when the amplitudes of the most significant harmonic components are changed. Because the amount of loss change is small, the effect of this kind of phenomena is difficult to show by measurements. This shows the usefulness of simulations when the VSD energy efficiency is studied.

### 5.8 Comparison of simulation results and measurements at the nominal point with a sinusoidal supply

The losses of the 37 kW induction motor under test were measured according to IEC 60034-2-1 standard (IEC, 2007). The figures of the results of the no-load-test and the rated load test are given in Appendix B. The efficiency measurements were made to investigate the loss accuracy of the FEM motor model at the nominal point. In the simulations, the FEM motor model was calculated with 25  $\mu$ s time steps, with a voltage and a current supply. The measured and simulated losses are given in Table 5.4.

Table 5.4. Measured losses from the efficiency measurements IEC60210-2-1 and simulated losses with a 50 Hz sinusoidal supply at the nominal point.

	Measured losses [W]	Simulated losses [W] Voltage	Simulated losses [W] Current
Friction and windage	338	(338)	(338)
Copper loss stator	973	680	679
Copper loss rotor	501	599	583
Iron loss stator	-	631	626
Iron loss rotor	-	258	237
Total iron loss	693	889	864
Additional loss	171	(171)	(171)
Total losses	2676	2677	2635

The friction, windage and additional losses are added to the simulated losses. The loss differences between the voltage and the current supply are negligible. The total simulated loss corresponds well to the measured losses, although the simulated losses take place in wrong parts of the machine. In the voltage supply simulation, the stator current RMS value was 68.7 A and the rotational speed of the motor was 1486  $\text{min}^{-1}$ . The smaller losses of the rotor parts in the current input simulation can be explained by the rotor. In the measurements, the corresponding values were 69 A (nominal current) and 1480  $\text{min}^{-1}$  (nominal rotational speed).

## 6 COMPARISON OF THE MEASURED AND SIMULATED LOSSES

Heat run tests performed on electrical machines are extremely important both for manufacturers and users. A manufacturer would like to have an optimally designed machine so that the product is competitive, while a user wants to be sure that the motor temperature at full load does not exceed the thermal limits of the insulation and thus have a negative impact on the motor lifetime (Mihalcea et al., 2001). A 37 kW industrial totally enclosed fan-cooled (TEFC) class 130 (B) temperature rise induction motor was used in the tests. The frame size of the motor is 225. The catalogue value of the efficiency for this motor is 93.6 % with a full load and 93.4 % with a 75 % load in a sinusoidal supply. Two equal-power frequency converters were used in the test, an ACS800 with the DTC and an ACS550 with the vector control.

In the temperature test measurement, the motor temperature with a sinusoidal supply and with a frequency converter supply was recorded. With the sinusoidal supply, the electrical input power of the motor, the rotational speed and the shaft torque were recorded by a 500 Nm Magtrol torque transducer TM H5 313/111. In the frequency converter use, the electrical input and output power of the converter were recorded by two Yokogawa PZ4000 power analysers. In these measurements, a 10 second record length with 1 million samples at a 1 minute interval was used. At each operating point, the motor was running 540 minutes (eight hours) to obtain thermal equilibrium and correct slip. The electrical powers shown here are an average value of the last 30 samples. At the end of the measurement, the current and voltage were recorded with a 1 second time interval and a 1  $\mu$ s sample time to perform the DFT analysis to obtain the fundamental voltage and current as well as to calculate the distortion.

The sinusoidal supply tests were carried out with 25 Hz, 40 Hz and 50 Hz frequencies. A synchronous generator was used to supply the motor with 25 Hz and 40 Hz sinusoidal voltages. The ACS800 converter was driven with a frequency reference. The ACS550 was measured with the scalar control and with the vector control. When measuring the ACS550 with the sensorless vector control, the speed reference was set to the desired level to obtain the correct output frequency, because in the ACS550, there is no option to drive the motor vector controlled with a frequency reference.

### 6.1 25 Hz operating point

The input (terminal) phase voltage of the frequency converter was set to an RMS value of 230 V with a transformer. As a load, a DTC-controlled induction machine was used. The nominal load of the 37 kW induction machine is 239 Nm, the load value was set to 220 Nm resulting in 92 per cent of the nominal load torque. The temperature rises in Fig 6.1 are the average values of the three Pt-100 sensors located in the stator windings. The laboratory temperature was recorded with a Pt-100 sensor and it was subtracted from the results. During the temperature tests, the laboratory temperature varied between 25–28°C.

The numerical results of the measurements are given in Table 6.1 and Table 6.2. Both the THD and TD values provided in the tables are calculated from the current. For the vector-controlled ACS550, the fundamental component of the voltage decreases, when the switching frequency is increasing. Thus, more fundamental wave power is needed to produce the required torque and speed. Although the fundamental voltage is decreasing, the fundamental current component is increasing, and thus, the voltage and current distortions decrease as the switching frequency is increased. The slip of the motor is at its highest value when the switching frequency is low and losses are high. This shows that the motor is behaving logically in the measurements.

Table 6.1. Numerical results of the measurements at the 25 Hz operation point with the sinusoidal and vector controlled supply.

	<b>Sinusoidal</b>	<b>Vector</b>	<b>Vector</b>	<b>Vector</b>
$f_{sw}$ [kHz]	-	1	4	8
$U_{fund}$ [p.u.]	0.477	0.499	0.498	0.497
$I_{fund}$ [p.u.]	0.933	0.931	0.935	0.936
$I_{RMS}$ [A]	64.47	66.01	64.70	64.74
$n$ [rpm]	729*	731	734	733
$T$ [Nm]	219.7	220.4	220.2	220.3
$P_{mech}$ [kW]	16.66	16.87	16.93	16.91
$P_{out}$ [kW]	18.30	19.18	18.70	18.71
$P_{in}$ [kW]	-	19.63	19.24	19.42
THD <sub>50</sub> [%]	1.34	21.7	2.48	2.36
TD <sub>20000</sub> [%]	2.68	23.4	7.63	5.87

\*supply frequency 24.84 Hz

Table 6.2. Numerical results of the measurements at the 25 Hz operating point with the DTC converter supply.

	<b>DTC</b>	<b>DTC</b>	<b>DTC</b>	<b>DTC</b>
$f_{sw}$ [kHz]	1	2	3	3.75
$U_{fund}$ [p.u.]	0.515	0.514	0.514	0.513
$I_{fund}$ [p.u.]	0.918	0.925	0.919	0.919
$I_{RMS}$ [A]	63.92	63.95	63.50	63.60
$n$ [rpm]	732	733	733	734
$T$ [Nm]	220.7	221.7	220.1	219.9
$P_{mech}$ [kW]	16.94	17.02	16.92	16.90
$P_{out}$ [kW]	18.82	18.79	18.62	18.61
$P_{in}$ [kW]	19.41	19.46	19.36	19.42
THD <sub>50</sub> [%]	1.96	1.58	1.08	1.52
TD <sub>20000</sub> [%]	14.36	7.98	5.93	5.58

The THD values show considerable distortion when the vector converter is used with a 1 kHz carrier frequency. The differences in the amount of harmonic components between 4 kHz and 8 kHz carrier frequencies are not significant. The DTC converter has a less distorted current than the vector controlled converter. The temperature rises of the 37 kW induction motor are shown in Fig 6.1.

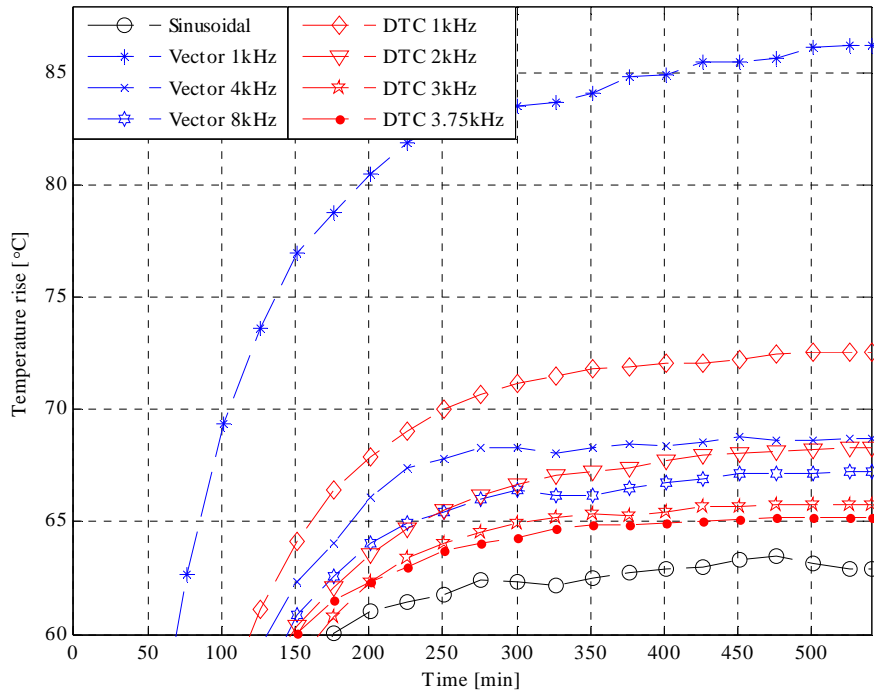


Fig 6.1. Temperature rise curves of the 37 kW induction motor with the sinusoidal, vector (ACS550) and DTC (ACS800) supply. The load torque is set to 92 % of the motor nominal torque.

The temperature rises in Fig 6.1 show that the differences between the motor temperature rises with different switching frequencies are smaller with high switching frequencies. Nevertheless, there is a clear difference in the temperature rises between all switching frequencies. The above results also show that the influences of the switching frequency on current distortion, motor temperature rise and motor losses diverge when different control systems are used. The temperature rise using a 25 Hz sinusoidal supply and 92 per cent of the nominal load is 62.7 °C and the measured losses 1529 W. In Fig 6.2, the measured temperature rise and loss changes in the frequency converter use are shown as a function of inverter switching frequency.

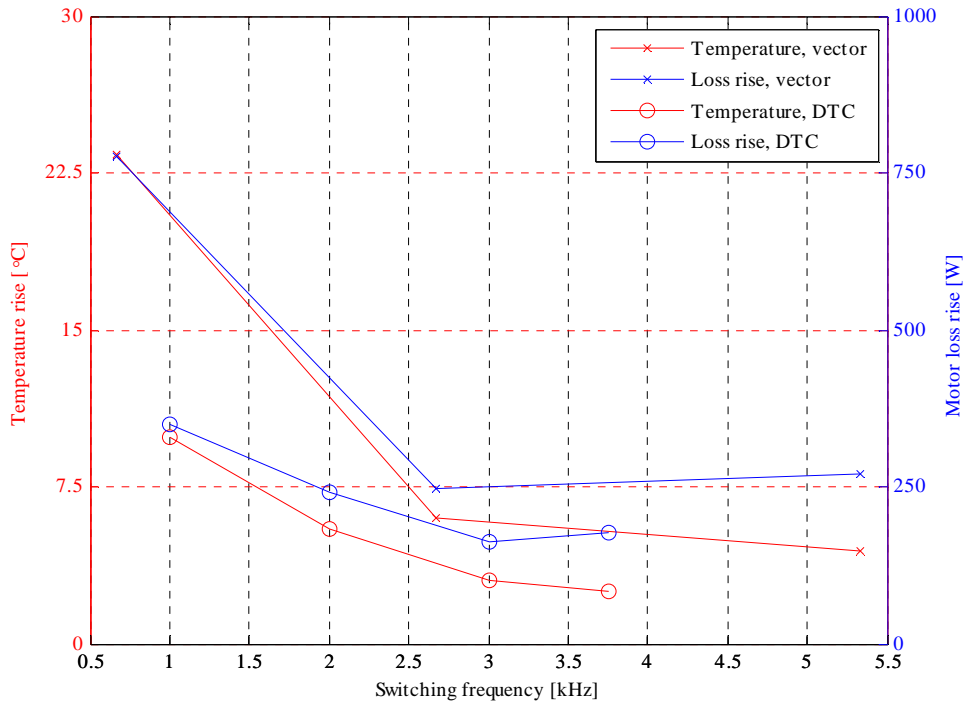


Fig 6.2. Temperature rise and loss changes compared with the 25 Hz sinusoidal supply as a function of switching frequency. The load torque is set to 92 % of the motor nominal load.

The additional temperature rise and additional motor losses produced by a frequency converter are at their highest values when the switching frequency is low. The losses of the motor rise from 200 W up to 760 W depending on the switching frequency and the converter used. The temperature rise and loss curves do not exactly match in Fig 6.2. The temperature rise curves can be assumed to be a more reliable indicator of the motor losses than the direct power measurement. If we assume that the correct value of the measured torque is 220 Nm and the correct rotational speed is 732 rpm, the losses vary by 77 W, when the torque measurement has an error of 1 Nm and 100 W if the speed has an error of 1 rpm, respectively. The total motor losses at this operation point are around 1800 W, and consequently, the relative loss error can be very large. The largest difference in the additional losses produced by two different converters can be assumed to be the voltage fundamental wave amplitude. A higher voltage means a smaller current, and therefore, dominating resistive losses will decrease.

The simulator was used to calculate the drive losses at the motor operating points in the measurements. The simulation software does not take friction and windage or all additional (stray) losses into account, and when the simulated losses are compared with the measured losses, these losses are added to the simulated losses. The simulation results of the motor losses are given in Table 6.3 and Table 6.4.

Additional losses are proportional to the square of the load current and to the power of 1.5 of the frequency, that is, (Pyrhönen et al., 2009)

$$P_{\text{ad}} \approx I^2 f^{1.5}. \quad (6.1)$$

The additional losses in the following tables are scaled loss values obtained by efficiency measurements at the nominal point. Friction losses of the motor are directly proportional to the speed, and windage losses are proportional to the third power of speed. Because the ratio of the friction and windage losses is not known, the total friction and windage losses are here assumed to be proportional to the square of speed.

Table 6.3. Simulated and measured motor losses with a sinusoidal supply and the vector controlled frequency converter.

	<b>Sinusoidal</b>	<b>1 kHz</b>	<b>4 kHz</b>	<b>8 kHz</b>
Copper loss stator [W]	595	648	614	613
Iron loss stator [W]	214	344	328	307
Copper loss rotor [W]	414	849	506	468
Iron loss rotor [W]	76	145	124	110
Additional loss [W]	52	52	52	52
Friction and windage [W]	85	85	85	85
Total simulated [W]	1436	2123	1708	1634
Total measured [W]	1640	2306	1775	1798

Table 6.4. Simulated and measured motor losses with the DTC frequency converter.

	<b>1 kHz</b>	<b>2 kHz</b>	<b>3 kHz</b>	<b>3.75 kHz</b>
Copper loss stator [W]	605	593	593	593
Iron loss stator [W]	350	349	349	349
Copper loss rotor [W]	621	509	480	471
Iron loss rotor [W]	150	145	142	140
Additional loss [W]	52	52	52	52
Friction and windage [W]	84.5	84.5	84.5	84.5
Total simulated [W]	1863	1733	1700	1690
Total measured [W]	1880	1770	1700	1710

The absolute values of the simulated losses with the vector controlled frequency converter do not match the measured losses, but the simulated losses with the DTC correspond well to the measured losses. The effect of the switching frequency on motor losses in the vector controlled simulations is correct; the total simulated losses and the measured losses are 500 W higher when a 8 kHz carrier frequency is used compared with a 1 kHz carrier frequency. At 3.75 kHz switching frequency (DTC), the measured losses may have an erroneous loss value, because the

motor temperature rise at this point is lower than at the 3 kHz point, but the measured losses are higher. Tables 6.5 and 6.6 show the simulation results for the frequency converter losses. The frequency converter loss calculation parameters are given in Appendix A.

Table 6.5. Simulated and measured frequency converter losses with the vector controlled frequency converter.

	<b>1 kHz</b>	<b>4kHz</b>	<b>8 kHz</b>
Input inductor	29	29	29
Diode bridge	62	62	62
DC link	23	23	23
IGBT bridge	270	384	534
Extra	70	70	70
Total simulated	455	568	719
Total measured	449	544	715

Table 6.6. Simulated and measured frequency converter losses with the DTC frequency converter.

	<b>1 kHz</b>	<b>2 kHz</b>	<b>3 kHz</b>	<b>3.75 kHz</b>
Input inductor	49	48	48	48
Diode bridge	70	69	69	69
DC link	31	30	30	31
IGBT bridge	322	372	423	450
Extra	120	120	120	120
Total simulated	592	639	690	718
Total measured	590	670	740	810

Naturally, the inverter switching frequency affects only the IGBT module losses. The same power flowing through the converter produces the same losses. In the simulated losses, the rate of change as a function of inverter switching frequency is not correct. One source of the error is the extra losses, as a higher switching frequency means more losses and more ventilation is required to cool down the power devices. Here, the cooling losses are assumed constant. The simulated vector controlled frequency converter losses follow the measured losses well, when the switching frequency is increased.

## 6.2 40 Hz operating point

At the 40 Hz operating point, the frequency converters are functioning in the normal operating range, and the motor power is 74 % of the nominal power. The sinusoidal voltage was produced by a synchronous generator. The THD<sub>50</sub> value of the grid voltage is 0.65 % measured at the motor terminals. The numerical results of the measurements are given in Table 6.7 and Table 6.8. The vector controlled frequency converter was driven with the sensorless control, and the speed reference was set to 1189 min<sup>-1</sup> to achieve a 40 Hz output voltage frequency. The DTC converter was driven with the frequency reference set to 40 Hz without slip compensation.

Table 6.7. Numerical results of the measurements at the 40 Hz operation point with the sinusoidal and vector controlled supply.

	<b>Sinusoidal</b>	<b>Vector</b>	<b>Vector</b>	<b>Vector</b>
$f_{sw}$ [kHz]	-	1	4	8
$U_{fund}$ [p.u.]	0.795	0.795	0.793	0.792
$I_{fund}$ [p.u.]	0.938	0.935	0.941	0.940
$I_{RMS}$ [A]	64.8	65.6	65.0	65.2
$n$ [rpm]	1185	1183	1183	1183
$T$ [Nm]	219.0	219.1	218.9	219.2
$P_{mech}$ [kW]	27.18	27.14	27.12	27.16
$P_{out}$ [kW]	29.28	29.79	29.47	29.47
$P_{in}$ [kW]	-	30.31	30.09	30.28
THD <sub>50</sub> [%]	0.80	18.03	3.33	3.38
TD <sub>20000</sub> [%]	2.12	23.17	7.63	5.82

Table 6.8. Numerical results of the measurements at the 40 Hz operating point with the DTC converter supply.

	<b>DTC</b>	<b>DTC</b>	<b>DTC</b>	<b>DTC</b>
$f_{sw}$ [kHz]	1	2	3	3.75
$U_{fund}$ [p.u.]	0.818	0.822	0.822	0.817
$I_{fund}$ [p.u.]	0.925	0.925	0.927	0.927
$I_{RMS}$ [A]	64.1	64.0	64.0	64.0
$n$ [rpm]	1184	1184	1184	1184
$T$ [Nm]	219.0	219.2	219.0	219.0
$P_{mech}$ [kW]	27.15	27.18	27.15	27.15
$P_{out}$ [kW]	29.55	29.43	29.39	29.38
$P_{in}$ [kW]	30.23	30.20	30.23	30.27
THD <sub>50</sub> [%]	2.77	1.68	1.30	1.74
TD <sub>20000</sub> [%]	14.98	8.61	6.24	6.23

The numerical results show that the slip of the motor remains constant with all switching frequencies for both converters. When the motor is driven with the DTC, the slip of the motor is  $1 \text{ min}^{-1}$  smaller than when using the vector control. The current distortion shows that the DTC modulation is capable of producing less distorted current than the symmetrical two-phase modulation. Similarly as at the 25 Hz operating point, the DTC is driving the motor with a higher voltage than the vector control. The less distorted, smaller current results in lower motor losses. The simulated and measured losses with the sinusoidal, vector and DTC supply are given in Table 6.9 and 6.10.

Table 6.9. Simulated and measured motor losses with the sinusoidal supply and the vector controlled frequency converter.

	<b>Sinusoidal</b>	<b>1 kHz</b>	<b>4 kHz</b>	<b>8 kHz</b>
Copper loss stator	591	634	613	611
Iron loss stator	602	549	539	506
Copper loss rotor	525	801	549	515
Iron loss rotor	250	242	217	200
Additional loss	109	109	109	109
Friction and windage	216	216	216	216
<b>Total simulated</b>	<b>2293</b>	<b>2551</b>	<b>2233</b>	<b>2157</b>
<b>Total measured</b>	<b>2100</b>	<b>2650</b>	<b>2348</b>	<b>2318</b>

The simulated losses do not match the measured ones. The simulated current THD<sub>50</sub> values are 21.18 %, 2.63 % and 4.91 %, and RMS values are 66.6 A, 65.0 A and 65.0 A with 1 kHz, 4 kHz and 8 kHz carrier frequencies, respectively. The RMS values of the simulated currents are larger than the measured ones, but still, the losses are smaller. This is disappointing, because the simulated motor losses using the DTC match almost perfectly.

Table 6.10. Simulated and measured motor losses with the DTC frequency converter.

	<b>1 kHz</b>	<b>2 kHz</b>	<b>3 kHz</b>	<b>3.75 kHz</b>
Copper loss stator	600	594	593	594
Iron loss stator	547	544	542	542
Copper loss rotor	632	551	536	532
Iron loss rotor	244	239	235	233
Additional loss	109	109	109	109
Friction and windage	216	216	216	216
<b>Total simulated</b>	<b>2348</b>	<b>2253</b>	<b>2231</b>	<b>2226</b>
<b>Total measured</b>	<b>2396</b>	<b>2253</b>	<b>2241</b>	<b>2225</b>

The simulated losses of the motor with both the converters presented above behave as assumed. A larger switching frequency reduces rotor losses. The simulated and measured frequency converter losses are presented in Table 6.11 and Table 6.12.

Table 6.11. Simulated and measured frequency converter losses with the vector controlled frequency converter at the 40 Hz point.

	<b>1 kHz</b>	<b>4kHz</b>	<b>8 kHz</b>
Input inductor	45	45	63
Diode bridge	89	89	103
DC link	22	21	22
IGBT bridge	280	396	546
Extra	70	70	70
<b>Total simulated</b>	<b>506</b>	<b>611</b>	<b>804</b>
<b>Total measured</b>	<b>514</b>	<b>619</b>	<b>803</b>

Table 6.12. Simulated and measured frequency converter losses with the DTC frequency converter at the 40 Hz point.

	<b>1 kHz</b>	<b>2 kHz</b>	<b>3 kHz</b>	<b>3.75 kHz</b>
Input inductor	81	104	105	105
Diode bridge	94	115	116	116
DC link	28	28	28	28
IGBT bridge	326	375	425	455
Extra	120	120	120	120
<b>Total simulated</b>	<b>649</b>	<b>742</b>	<b>794</b>	<b>824</b>
<b>Total measured</b>	<b>686</b>	<b>770</b>	<b>836</b>	<b>896</b>

The frequency converter losses increase with an increasing switching frequency. The simulator slightly underestimates the DTC converter losses, and the largest differences in the DTC frequency converter losses are when the highest 3.75 kHz switching frequency is used. On the other hand, the simulated losses with vector controlled converter are very close to the measured losses. The temperature rise curves of the motor at the 40 Hz operating point are shown in Fig. 6.3.

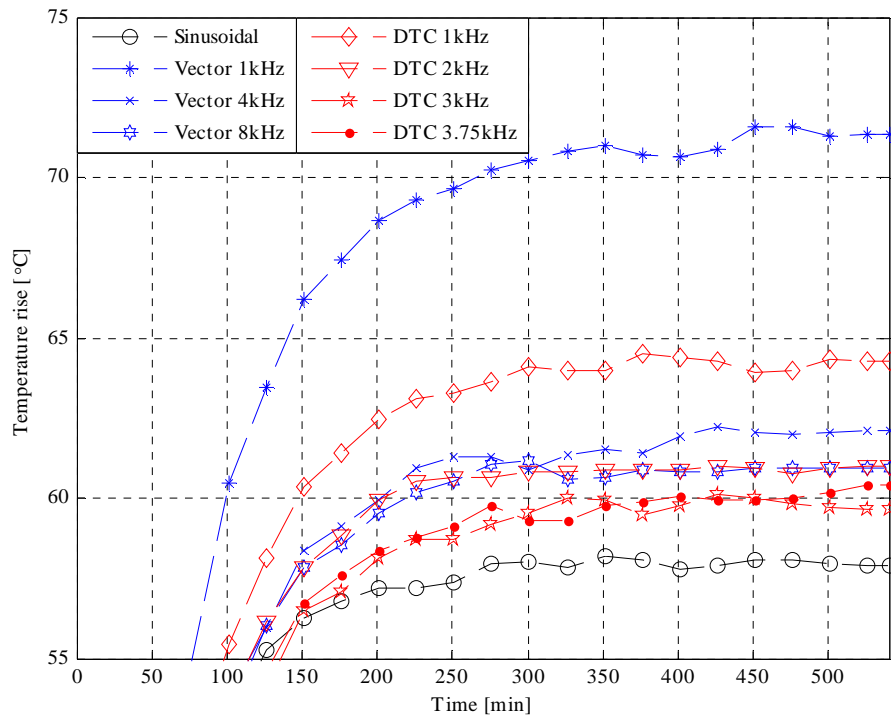


Fig. 6.3. Temperature rises at the 40 Hz point with 92 % torque using the sinusoidal (generator), vector (ACS550) and DTC (ACS800) supply for the 37 kW induction motor.

The temperature rise curves in Fig. 6.3 are not in an order that was assumed. The temperature rise of the motor fed by the DTC converter with 3 kHz is smaller than the temperature rise with the 3.75 kHz switching frequency. The results above support the results obtained at the 25 Hz operating point; the temperature rises of the motor are smaller when the DTC converter is used instead of the vector controlled converter. The temperature rise and loss changes compared with the 40 Hz sinusoidal supply as a function of switching frequency are shown in Fig 6.4.

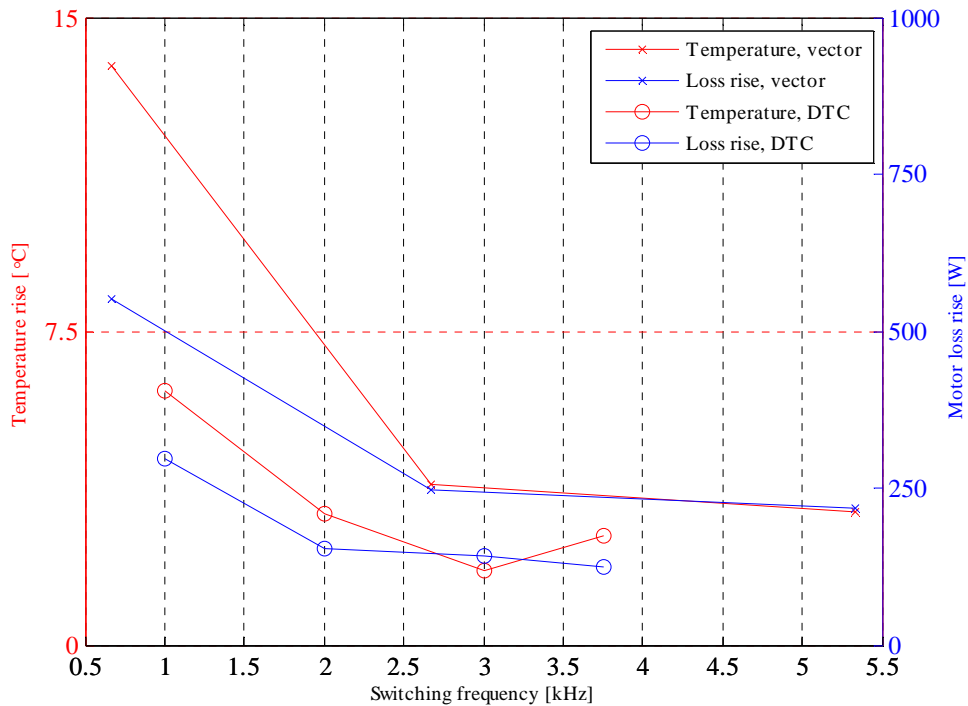


Fig 6.4. Temperature rise and loss changes compared with the 40 Hz sinusoidal supply as a function of switching frequency with 92 % torque.

The motor losses with the sinusoidal supply are 2100 W and the temperature rise is 58.0°C. The motor losses at the 40 Hz point increase from 120 W to 600 W and the temperature rises from 3 to 14 degrees Celsius. Both quantities show that the loss increase produced by the frequency converter is slightly less than at the 25 Hz operating point. At the 40 Hz point, the motor is running cooler than at the 25 Hz point, because the cooling of motor is significantly increased.

### 6.3 50 Hz operating point

The 50 Hz point is interesting because both converters can use overmodulation or field weakening at this point. Further, the minimum pulse length is affecting the real switching frequency of the ACS550 (vector control) converter. The simulations have been carried out only in the field weakening mode. The measured voltages and currents are shown in Fig 6.5 in stator coordinates.

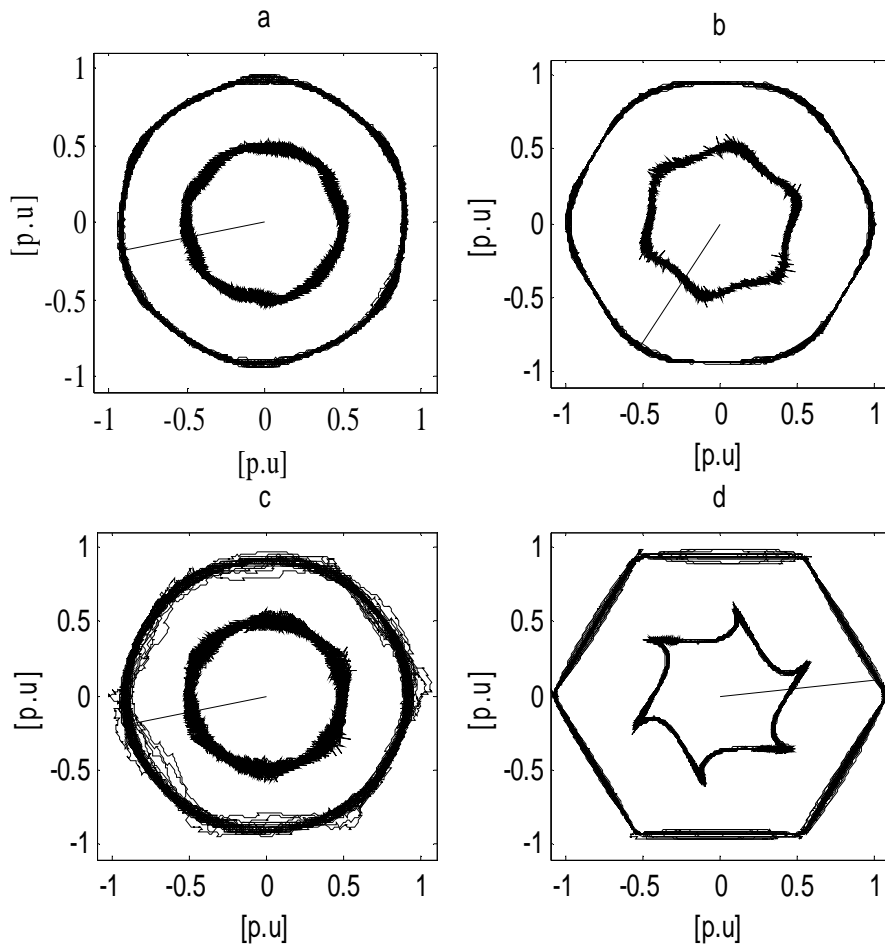


Fig 6.5. Stator voltage and current in the 50 Hz operation point. The measured voltage (averaged to 1 ms), and the current in stator coordinates scaled to 0.5. a) ACS550 with the vector control, b) ACS550 with the scalar control, c) ACS800 in the normal operating mode, d) ACS800 when the Hex-field-weakening parameter is turned on.

Fig 6.5 shows that the scalar-controlled ACS550 is in the overmodulation range. Neither the voltage nor the current are sinusoidal. The ACS800 in the normal operating mode is reducing the flux linkage reference and keeps the voltage almost sinusoidal operating at the edge of the overmodulation range. When the Hex-Field-Weakening is turned on, the ACS800 is even deeper in the overmodulation region than the scalar-controlled 550. This can be explained by structural differences in the frequency converters leading to different DC link voltages. The switching frequency reference of the ACS800 is 3 kHz in both cases, and the theoretical switching frequency of the ACS550 is 2.66 kHz. The calculated switching frequencies of the converters are a) 2138 Hz, b) 1492 Hz, c) 3000 Hz and d) 2400 Hz.

An accurate temperature test at the 50 Hz point requires a stationary grid voltage level. As shown in Fig 6.6 the motor phase current tracks the changes in the grid voltage; when the grid voltage decreases, the motor current increases, and vice versa.

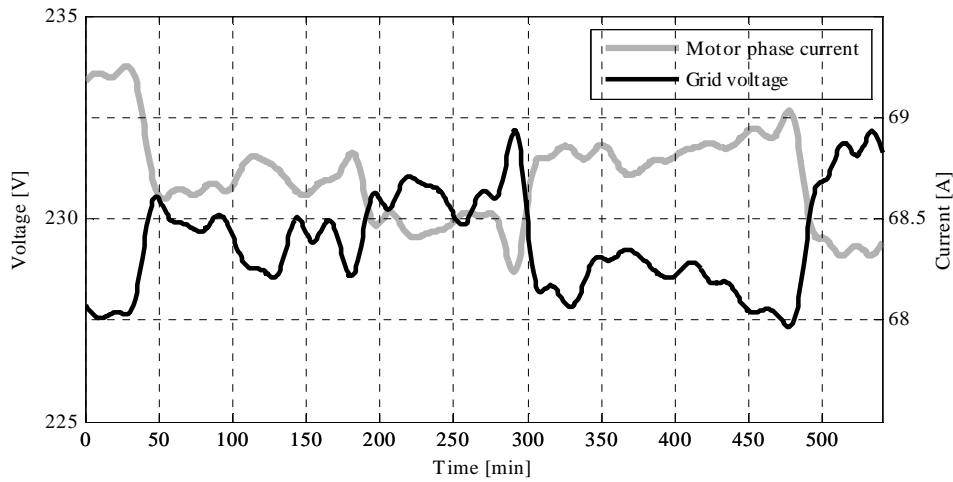


Fig 6.6. Grid voltage and motor phase current during a temperature rise test. The voltage and current curves are from the temperature rise test carried out with the 3 kHz average switching frequency.

At the 50 Hz operating point, the same load and switching frequencies were used as at the 25 Hz and 40 Hz points. The grid voltage with the THD<sub>50</sub> value of 1.24 % was used instead of the generator. The numerical results of the measurements are given in Table 6.13 and Table 6.14.

Table 6.13. Numerical results of the measurements at the 50 Hz operation point with the sinusoidal and ACS550 supply.

	<b>Sinusoidal</b>	<b>Vector</b>	<b>Vector</b>	<b>Vector</b>	<b>Scalar (ACS550)</b>
$f_{sw}$ [kHz]	-	1	4	8	4
$U_{fund}$ [p.u.]	0.999	0.926	0.919	0.922	0.965
$I_{fund}$ [p.u.]	0.937	0.978	0.988	0.990	0.958
$I_{RMS}$ [A]	64.9	68.5	68.4	68.2	66.3
$n$ [rpm]	1484	1479	1482	1480	1481
$T$ [Nm]	219.7	219.5	219.5	219.9	220.4
$P_{mech}$ [kW]	34.14	34.00	34.07	34.08	34.10
$P_{out}$ [kW]	36.46	36.94	36.85	36.77	36.93
$P_{in}$ [kW]	-	37.51	37.53	37.59	37.50
THD <sub>50</sub> [%]	2.52	15.47	3.44	3.77	3.80
TD <sub>20000</sub> [%]	5.60	17.48	7.61	4.97	8.08

Table 6.14. Numerical results of the measurements at the 50 Hz operating point with the DTC supply.

	<b>DTC</b>	<b>DTC</b>	<b>DTC</b>	<b>DTC</b>	<b>DTC Hex</b>
$f_{sw}$ [kHz]	1	2	3	3.75	2.4
$U_{fund}$ [p.u.]	0.922	0.914	0.906	0.914	0.999
$I_{fund}$ [p.u.]	0.983	0.987	0.995	0.989	0.937
$I_{RMS}$ [A]	68.4	68.3	68.9	68.7	66.0
$n$ [rpm]	1479	1480	1479	1479	1482
$T$ [Nm]	218.9	218.6	218.6	218.2	220.3
$P_{mech}$ [kW]	33.90	33.88	33.85	33.80	34.19
$P_{out}$ [kW]	36.68	36.62	36.60	36.54	36.92
$P_{in}$ [kW]	37.46	37.47	37.54	37.45	37.83
THD <sub>50</sub> [%]	2.57	2.70	2.34	2.99	18.50
TD <sub>20000</sub> [%]	10.25	7.36	6.28	6.57	18.69

At the 50 Hz operating point, the amplitude of the fundamental wave voltage of the vector-controlled converter is larger than the one that the DTC converter is using to drive the motor. At the 25 Hz and 40 Hz operating points, the situation with the fundamental wave amplitude is the opposite. The current distortion of the DTC converter still remains smaller than the one obtained with the vector controlled converter. The ACS550 in the scalar mode is using more voltage than in the vector mode, which results in a lower RMS, but a more distorted current. The slip of the motor in the scalar control is decreased by  $1 \text{ min}^{-1}$  compared with the vector control with the same carrier frequency. Similar results are obtained with the ACS800 when the Hex-field-weakening is turned on. In this case, the current distortion level is high. The motor loss simulation results at 50 Hz operating point are given in Table 6.15 and Table 6.16.

Table 6.15. Simulated and measured motor losses with the sinusoidal supply and the vector controlled frequency converter at 50 Hz and 92 % torque

	<b>Sinusoidal</b>	<b>1 kHz</b>	<b>4 kHz</b>	<b>8 kHz</b>
Copper loss stator	591	682	679	665
Iron loss stator	602	712	696	674
Copper loss rotor	525	798	644	599
Iron loss rotor	250	302	284	272
Additional loss	147	147	147	147
Friction and windage	338	338	338	338
Total simulated	2453	2979	2788	2695
Total measured	2316	2940	2788	2688

Table 6.16. Simulated and measured motor losses with the ACS800 frequency converter at 50 Hz and 92 % torque.

	<b>1 kHz</b>	<b>2 kHz</b>	<b>3 kHz</b>	<b>3.75 kHz</b>
Copper loss stator	656	651	649	649
Iron loss stator	706	704	699	699
Copper loss rotor	658	614	601	597
Iron loss rotor	300	296	293	291
Additional loss	147	147	147	147
Friction and windage	338	338	338	338
Total simulated	2805	2750	2727	2721
Total measured	2774	2740	2745	2745

At the 50 Hz point, the simulated motor losses are almost identical to the measured losses with both frequency converters. In the case of the DTC converter, the effect of the switching frequency on motor losses is smaller than in the measured ones, but the loss simulation accuracy is at a very good level. The simulated and measured frequency converter losses at the 50 Hz operating point are given in Table 6.17 and Table 6.18.

Table 6.17. Simulated and measured frequency converter losses with the vector controlled frequency converter at 50 Hz and 92 % torque

	<b>1 kHz</b>	<b>4kHz</b>	<b>8 kHz</b>
Input inductor	69	68	68
Diode bridge	105	102	104
DC link	20	19	19
IGBT bridge	304	424	577
Extra	70	70	70
Total simulated	567	682	870
Total measured	576	677	824

Table 6.18. Simulated and measured frequency converter losses with the DTC frequency converter at 50 Hz and 92 % torque.

	<b>1 kHz</b>	<b>2 kHz</b>	<b>3 kHz</b>	<b>3.75 kHz</b>
Input inductor	157	167	163	163
Diode bridge	137	138	138	138
DC link	26	26	25	25
IGBT bridge	343	391	431	463
Extra	120	120	120	120
Total simulated	784	837	879	908
Total measured	783	853	941	906

Unlike the simulated losses, the measured losses do not behave logically in the case of the DTC converter. In the measured losses, with the highest switching frequency (3.75 kHz), the measured losses are smaller than with the 3 kHz switching frequency. This result cannot be correct. The error in the frequency converter losses can be in the measurements made with the 3 kHz switching frequency, because the simulated losses at this point are far from the measured losses even though they are close to each other at all other tested points. The results of the temperature rise tests at the 50 Hz point are illustrated in Fig 6.7.

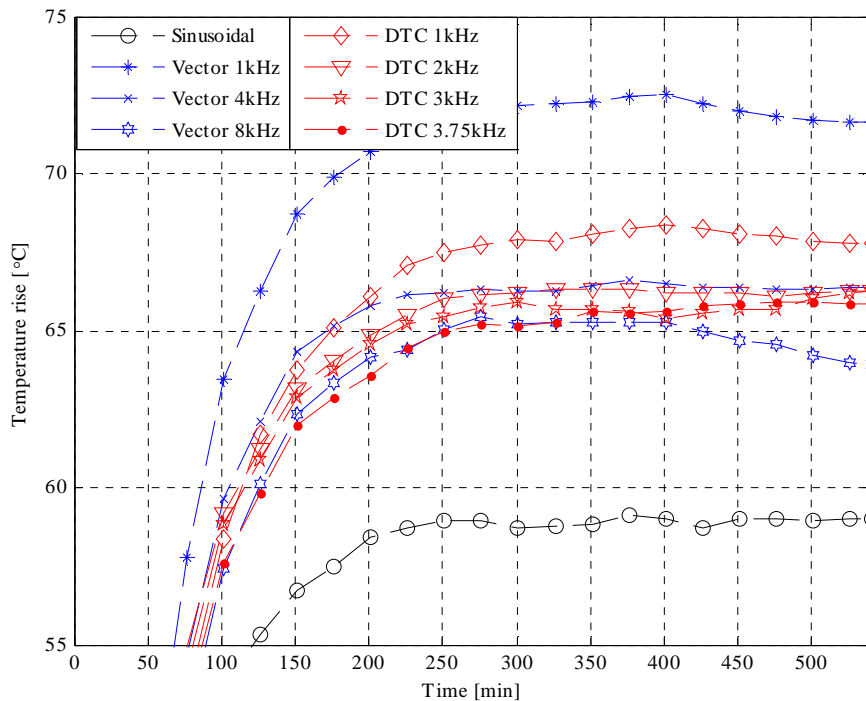


Fig 6.7. Temperature rises at the 50 Hz point using the sinusoidal (grid), VC converter (ACS550) and DTC converter (ACS800) supply for the 37 kW induction motor at 92 % torque.

The temperature rise curves in Fig 6.7 are not smooth. The most crucial temperature rise change is around 410 minutes of the vector controlled converter temperature test with the 8 kHz (also 1 kHz) carrier frequency; at this time, the phase voltage of the grid is rapidly rising from 230 V to 233 V. This shows that even small voltage changes in the supply voltage have an enormous effect on the motor losses at the 50 Hz operating point. Nevertheless, a clear difference between different switching frequencies can be seen in the motor temperature rises. The DTC converter with 2, 3 and 3.75 kHz switching frequencies demonstrates similar temperature rises. The temperature rise of the ACS550 with the 4 kHz carrier frequency reaches 67.2°C when the scalar control is used and 66.4°C in the vector control.

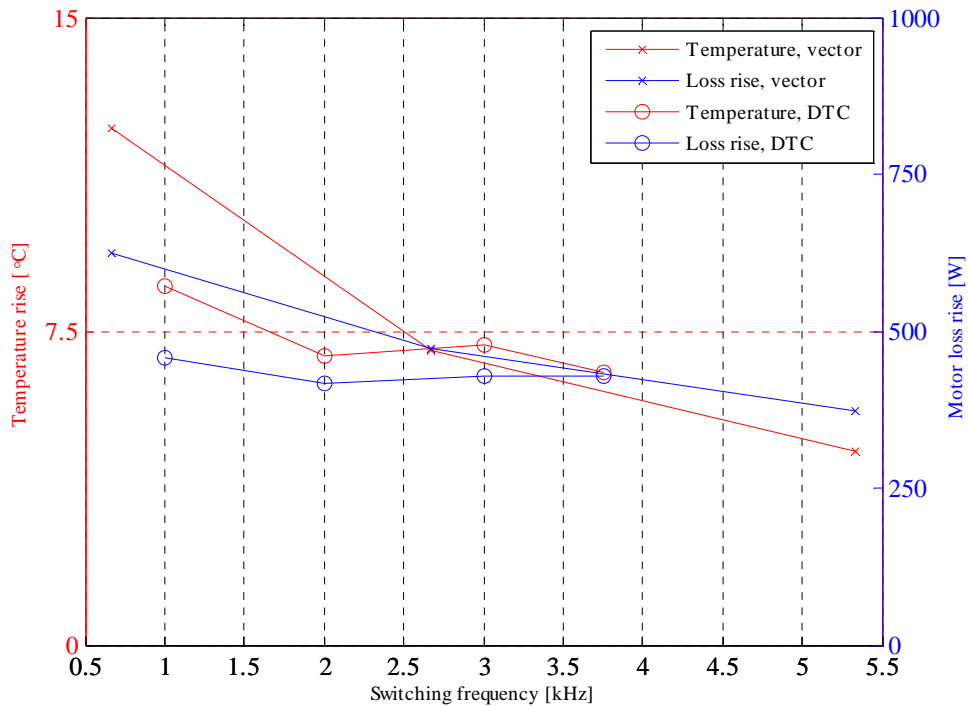


Fig 6.8. Temperature rise and loss changes compared with the 50 Hz sinusoidal supply as a function of switching frequency at 92 % torque.

The motor losses with the sinusoidal supply are 2316 W and the temperature rise is 58.3°C. The motor losses at the 50 Hz point increase from 380 W to 620 W and the temperature rises from 5 to 13 degrees Celsius. As given in Table 6.14, the fundamental wave voltage is slightly higher, when the switching frequency is low and the fundamental voltage is decreasing from the switching frequency 1 kHz to 3 kHz (ACS800). The higher fundamental wave voltage leads to a lower current and the dominating resistive losses become smaller. This distorts the impact of the switching frequency on the motor losses. At the 50 Hz point, the motor is running even cooler than at the 40 Hz point, but the field weakening operation is increasing the losses.

#### 6.4 Concluding remarks

The objective of this study was to estimate the drive system losses with a reasonable accuracy. This chapter compared the measured losses of the 37 kW induction motor with the simulated losses. Figures 6.9–6.14 illustrate the converter losses, motor losses and drive system losses as a function of switching frequency and carrier frequency.

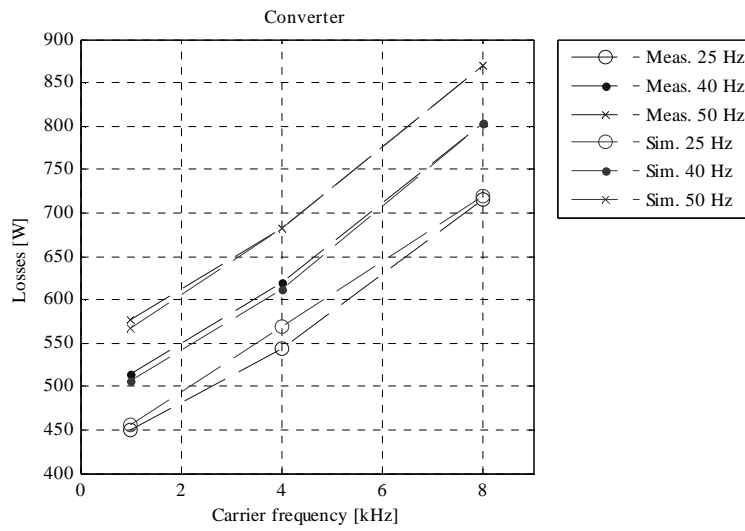


Fig 6.9. Simulated and measured VC converter (ACS550) losses as a function of carrier frequency at 92 % torque.

The simulated converter losses are very close to the measured ones. Small loss differences in the converter losses at the 25 Hz and 40 Hz curves can be detected, but the simulation accuracy is at a very good level and the loss values can be used to predict the frequency converter losses at different operation points.

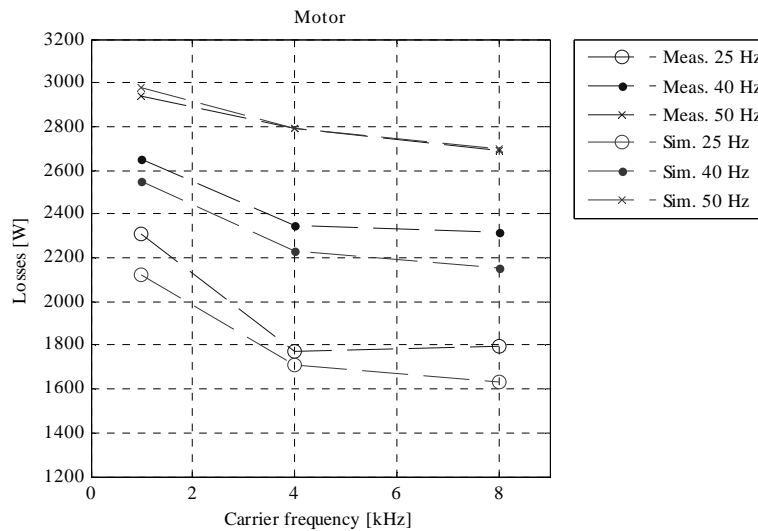


Fig 6.10. Simulated and measured 37 kW induction motor losses at 92 % torque as a function of carrier frequency when the VC converter is used.

The simulated motor losses at the 50 Hz point are equal to the measured ones. At partial speeds, the loss curves have a correct shape, but there is a loss level difference of approximately 150 W.

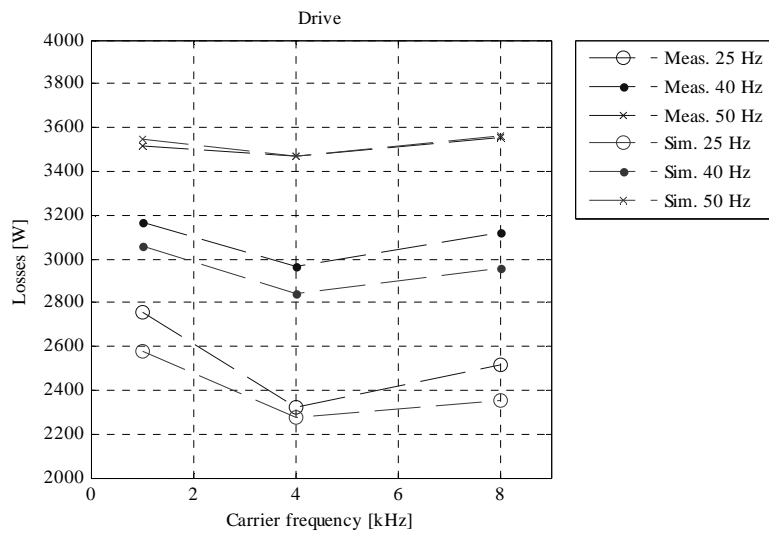


Fig 6.11. Simulated and measured drive losses as a function of carrier frequency at 92 % torque.

The drive system losses in Fig 6.11 summarizes the converter and motor losses. The differences in the simulated and measured motor losses at partial loads can be seen also from these curves. Both the simulated and measured drive system losses show that at the 4 kHz carrier frequency, the losses of the drive system are minimized. At the 8 kHz carrier frequency, the motor losses are slightly decreasing compared with the 4 kHz carrier frequency, but the increase in the frequency converter losses is larger than the decrease in the motor losses.

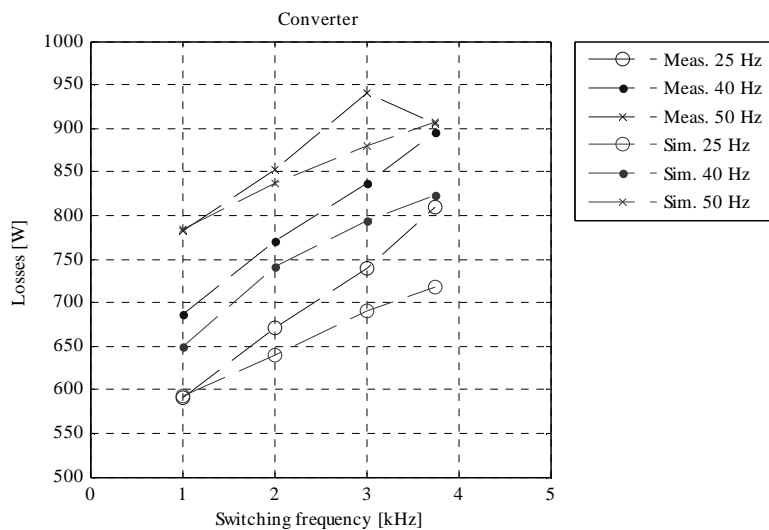


Fig 6.12. Simulated and measured DTC converter losses as a function of switching frequency at 92 % torque.

The effect of switching frequency in the simulated converter losses is too weak. In the measurements, the switching frequency impact on converter losses is higher than in the simulated results.

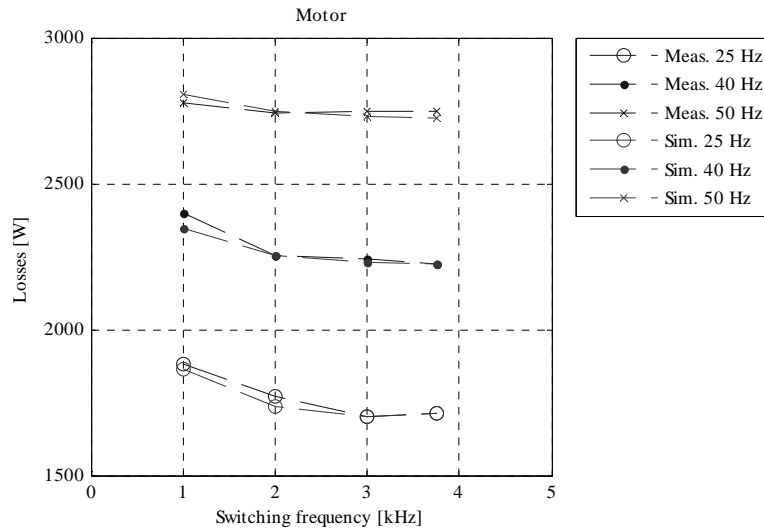


Fig 6.13. Simulated and measured 37 kW induction motor losses as a function of switching frequency when the DTC frequency converter is used at 92 % torque.

The simulated motor losses correspond well to the measured losses. No significant differences between the simulated and measured losses can be found. At the 50 Hz operation point, the switching frequency has almost no impact on the motor losses.

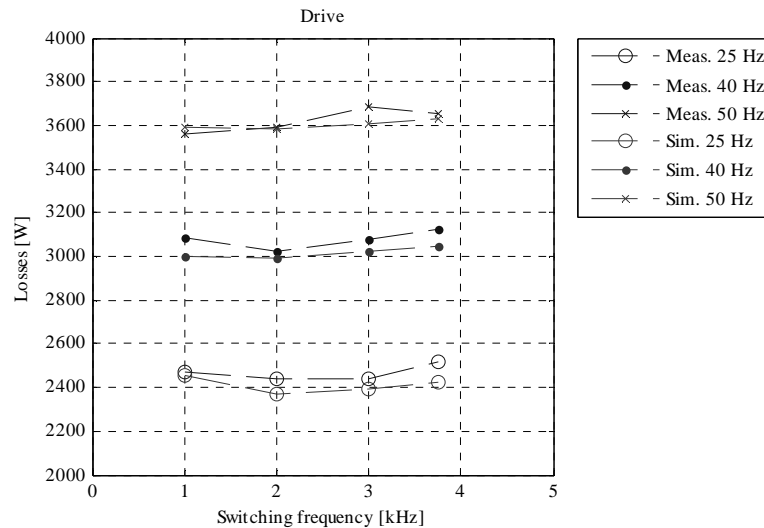


Fig 6.14. Simulated and measured drive system losses as a function of switching frequency at 92 % torque.

At the 50 Hz operating point, the drive system losses are similar to the switching frequencies from 1 kHz to 3 kHz, and it cannot be concluded which switching frequency minimizes the drive system losses. Although the simulated frequency converter losses are somewhat erroneous, the total simulated losses give a good picture of the drive system losses. The maximum error between the simulated and measured drive system losses are less than 100 W.

## 6.5 Torque ripple

As a drawback of the DTC control system is often mentioned its torque ripple. The torque ripple is extremely hard to measure reliably and remove the effects of load from the results. In Fig 6.15 the estimated electric torques of VC and DTC converters are illustrated when using the reference switching frequencies of the converters, a 4 kHz carrier frequency for the vector controlled drive and a 3 kHz average switching frequency for the DTC drive. The air gap torque is calculated from the measured values using Equations (1.20) and (1.21). The measured voltage has been filtered using a low-pass filter with a 20 kHz cut-off frequency before calculating the integral equation to obtain the flux linkage.

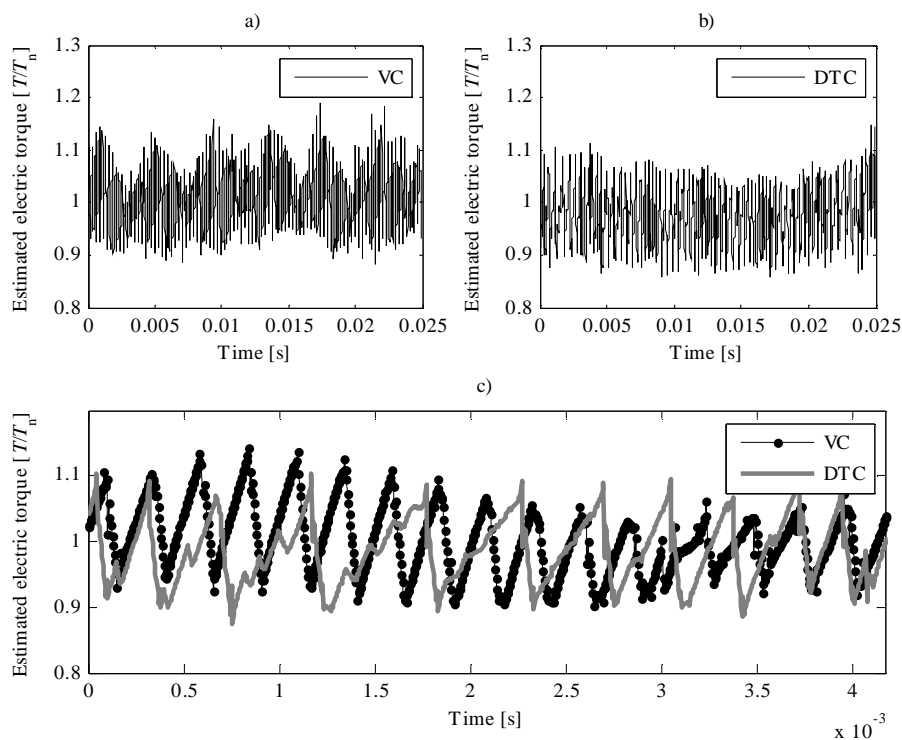


Fig 6.15. Estimated air gap electric torque of the 37 kW induction motor at the 40 Hz operating point with 92 % average load torque. a) Vector control supply with a 4 kHz carrier frequency, b) DTC supply with a 3 kHz switching frequency, c) Zoomed view.

Fig 6.15 shows that in this case the VC and DTC converters both have about similar air gap torque ripple.

## 7 CONCLUSION

This doctoral thesis studies the simulation of variable speed drives. Simulators are widely used in studying different phenomena. In the simulation of variable speed drives, there are multiple issues that have to be taken into account. The frequency converter model based on circuit (differential) equations controlled with a closed-loop feedback is able to produce voltage containing the same harmonic content as in the actual device. The accuracy of the FEM motor model loss calculation is good. The simple loss models used to calculate the frequency converter model include a lot of uncertainty, and they could be easily improved, although the loss model parameterization becomes a more challenging task.

The FEM motor model is shown to be a valuable tool in a motor design process, and the ability to simulate a FEM motor model under a PWM supply provides a means to improve the motor designs to operate more efficiently in a frequency converter use. This thesis shows that simulations can be used as a good starting point when analysing the extra losses produced by PWM waveforms in the motors. To deeper analyse the PWM-produced losses, information about the geometrical loss distribution, field and current distributions would be essential, but this information is unavailable in the FEM software version that is currently used in the simulator and is an item for further research.

The temperature rises of the motor, direct loss measurements and simulations all indicate that the DTC converter produces fewer losses in the motor than the VC drive with a comparable switching frequency. The objective of this dissertation was not to compare the performance between the two control methods (DTC and VC). The thesis loss results are based on two converters with different hardware and one motor, and therefore, generalizations about the control system performance should not be made. Both converters perform a motor identification run at the first start, and the control system is parameterized based on the identification run results. The motor parameter identification procedures of the converters are different and may lead to different results. Thus, the parameters that the converter control systems are using to drive the motor may be different in practice. The drives were measured using their sensorless control versions. The DTC is more robust against parameter variations than the vector control (coordinates transform). The target in the simulator development was not to improve the control system performance but to make the control system of the simulator to operate similarly as in the commercial devices.

The measuring system is an extremely important factor in the case of VSD measurements. During the measurements performed in the preparation of this thesis, it was found out that even the mechanical installation of the drive system can change the absolute loss values. It was also detected that the sampling of the electrical quantities has an effect on the measured loss values.

Although the fundamental wave is transferring most of the electric power from the frequency converter to the motor, the large harmonic content created by a modern frequency converter is the part that produces many undesired effects. However, this is a part of electric power that can be adjusted and manipulated in different ways. In addition to the temperature rise of the motor and the efficiency decrease, the dielectric stress of the insulation system and the damaging bearing currents induced by shaft voltages are harmful effects of PWM waveforms.

The effect of the switching frequency on the drive system losses is a complex function of motor construction, frequency converter losses, modulation method and operating point. For drive

efficiency comparison purposes, two different frequency converters supplying the same motor at a single operating point of the motor cannot give enough information to make reliable conclusions. In the efficiency measurement, the operating point where the motor is running at the nominal speed has more uncertainty than the operating points at lower speeds (in the linear region).

A direct loss measurement method can give a good understanding of the frequency converter losses, but the actual accuracy of these measurements is not yet investigated. Calorimetric measurements are the best way to verify the accuracy of the electric measurements.

### **7.1 Suggestions for further work**

The two-phase space vector modulation is one type of discontinuous pulse width modulation (DPWM) technique. This work can be extended to other types of DPWM methods that are reported in the literature. The different methods all have some advantages and disadvantages. Analogous vector control used in this thesis can be used to study the influence of the modulation method on motor losses.

The C-language platform has been proven to be a fast and reliable simulation tool. The slowest part of the simulator is the FEM motor model. The analytical loss equations for motors found in the literature could be implemented to even faster computation of the motor losses.

The simulator requires equivalent circuit parameters of the motor for fast and reliable loss simulation. These parameters could be identified from the FEM motor model at the beginning of the simulation.

The simulator uses a fixed time step for the FEM analysis. The calculation time could be shortened by using a variable-step simulation applying both the FEM and analytical model. The FEM is calculated only when the voltage vector is different from the previous value.

The simulation software does not take friction, windage or additional (stray) losses into account. These loss components could be calculated analytically to obtain a better overall picture of the total losses of the motor.

One feature of both the modern frequency converters and the frequency converter used in this thesis is the energy optimizing control of some kind. The energy efficient modes, for instance flux optimizing, improve the motor efficiency at partial loads. These modes could be implemented in the simulator, and the operation could be studied with simulations and verified by measurements.

Induction motor losses and slip are functions of motor temperature. To obtain even more accurate loss results, it is possible to add a thermal model of the motor to the simulator and use the feedback information in the FEM program.

## REFERENCES

Aarniovuori L., Laurila, L., Niemelä, M. and Pyrhönen, J. (2007), "Loss Calculation of a Frequency Converter with a Fixed-Step Circuit Simulator," In *the 12<sup>th</sup> European Conference on Power Electronics and Applications (EPE)*, Aalborg, Denmark.

Aarniovuori L., Laurila, L., Niemelä, M. and Pyrhönen, J. (2008), "Comparison of the Induction Motor Simulation Models – Analytical and FEM – in Drive System Controlled with Direct Torque Control," In *the 19th International Symposium on Power Electronics, Electrical Drives, Automation and Motion (SPEEDAM)*, Ischia, Italy.

Aarniovuori L., Laurila, L., Niemelä, M. and Pyrhönen, J. (2008), "Switching Frequency Harmonics of DTC IM Drive in a System Simulator with Analytical and FEM Motor Model," In *the 18<sup>th</sup> International Conference on Electrical Machines (ICEM)*, Vilamoura, Algarve, Portugal.

Aarniovuori L., Laurila, L., Niemelä, M. and Pyrhönen, J. (2009), "Comparison of Induction Motor FEM simulations fed by measured and reconstructed DTC inverter voltages," In *the 13th European Conference on Power Electronics and Applications (EPE)*, Barcelona, Spain.

Aarniovuori L., Laurila, L., Niemelä, M. and Pyrhönen, J. (2010), "DTC Frequency Converter Loss Analysis Using Coupled System Simulator and Measurements," In *the 19th International Conference on Electrical Machines (ICEM)*, Rome, Italy.

de Almeida A. T., Bertoldi, P., Leonhard, W., Editors (1997), *Energy Efficiency Improvements in Electrical Motors and Drives*, Springer-Verlag Berlin, Heidelberg.

de Almeida A. T., Ferreira, F.E., Fonseca, P. (2000), *Improving the Penetration of Energy-Efficient Motors and Drives*, ISR-Universidade de Coimbra, European Commission, Directorate-General for Transport and Energy, SAVE II Programme.

de Almeida A. T., Ferreira, F., Fonsenca, P., Falkner, H., Reichert J., West M., Nielsen, S. and Both, D. (2001), *VSDs for Electric Motor Systems*. Coimbra, Portugal: Inst Syst. Robot., Univ. Coimbra/EU, Directorate-General for Transport and Energy, SAVE II Programme.

Arkkio, A. (1987), *Analysis of Induction Motors Based on the Numerical Solution of the Magnetic Field and Circuit Equations*, Acta Polytechnica Scandinavica, Electrical Engineering Series, No. 59, 1987.

Arrillaga, J. and Watson, N. R. (2003), *Power System Harmonics*, John Wiley & Sons, Ltd, Chichester, England.

Belahcen, A. and Arkkio, A. (2008), "Comprehensive Dynamic Loss Model of Electrical Steel Applied to FE Simulation of Electrical Machines," *IEEE Transactions on Magnetics*, Vol. 44, No. 6, pp. 886-889.

Bertotti, G. (1998), *Hysteresis in Magnetism for Physicists, Material Scientists and Engineers*. London, U.K.: Academic, pp. 391–429.

Bierhoff, M.H. and Fuchs, F.W. (2000), "Semiconductor Losses in Voltage Source and Current Source IGBT Converters Based on Analytical Derivation." in *Proc. of IEEE 35th Power Electronics Specialists Conf. (PESC)*, vol. 4, Aachen, Germany, pp. 2836–2842.

Binder, A. (2008), "Potentials for Energy Saving with Modern Drive Technology – a survey," In *International Symposium on Power Electronics, Electrical Drives, Automation and Motion (SPEEDAM)*, Ischia, Italy.

Boglietti, A., Cavagnino, A. and Knight, A.M. (2007), "Factors Affecting Losses in Induction Motors with Non-Sinusoidal Supply," in *Conf. Rec. Ind. Appl. Conf.* vol. 1. pp. 1193–1199, New Orleans, LA, U.S.A.

van der Broeck, H.W. (1991), "Analysis of the harmonics in voltage fed inverter drives caused by PWM schemes with discontinuous switching operation," in *Proc. EPE'91 Conf.*, pp. 261–266.

Casadei, D., Serra, G. and Tani, A. (1994), "Effects of Flux and Torque Hysteresis Band Amplitude in Direct Torque Control of Induction Machines," in *Proc. of IECON'94*, Bologna, Italy. 1994. pp 299–304.

Casadei, D., Serra, G. and Tani, A. (1997), "Analytical Investigation of Torque and Flux Ripple in DTC Schemes for Induction Motors", in *Proc. IEEE IECON'97* New Orleans, LA, U.S.A., pp. 552–556.

Depenbrock, M. (1998), "Direct Self Control of Inverter-Fed Induction Machines," *IEEE Trans. on Power Electronics*, Vol. PE-3, no. 4, pp. 420-429.

De Doncker, R.W. and Novotny, D.W. (1994), "The universal field oriented controller," *IEEE Transactions on Industry applications*. Vol 30, No.1., pp. 92–100.

Dugan, R., McGranaghan, M.F., Santoso, S. and Beaty, H.W. (2002), *Electric Power System Quality*, second ed., McGraw-Hill, New York, U.S.A..

Erickson, R. (1997). *Fundamentals of Power Electronics*, New York: Chapman & Hall.

Heller, B. and Hamata, V. (1977), *Harmonic Field Effects in induction machines*. Elsevier. Amsterdam, 1977.

Hildebrand, E.N. and Roehrdanz, H. (2001), "Losses in Three-Phase Induction Machines Fed By PWM, Converter," *IEEE Transactions on Energy Conversion*, Vol. 16, No. 3., pp. 228–233.

Holmes, D.G. and Lipo, T.A. (2000), *Pulse Width Modulation For Power Converters – Principles and Practice*, Piscataway, NJ, U.S.A.: IEEE Press/John Wiley

Holz, J. (1994), "Pulsewidth modulation for electronic power conversion," *In Proceedings of the IEEE*, vol. 82. No. 8. pp. 1194–1214.

IEC. (2003), *IEC/TS 60034-17 3rd ed: Rotating electrical machines – Part 17: Cage induction motors when fed from converters – Application guide*

IEC. (2009), *IEC/TS 60034-31Ed 1: Rotating electrical machines – Part 31: Guide for the selection and application of energy-efficient motors including variable speed drives*. Committee Draft, 2009.

Idris, N.R.N. and Yatim, A.H.M. (2000), “Reduced torque ripple and constant torque switching frequency strategy for direct torque control of induction machine,” In *the Fifteenth Annual IEEE Applied Power Electronics Conference and Exposition*. Page(s): 154–161 vol.1, New Orleans, LA, U.S.A.

Idris, N.R.N., Yatim, A.H.M., Muhamad, N.D. and Ling T.C. (2003), “Constant Frequency Torque and Flux controllers for Direct Torque Control of Induction Machines,” In *IEEE 34<sup>th</sup> Annual Power Electronics Specialist Conference, PESC '03*. Vol. 3, pp. 1095–1100, Acapulco, México.

Jung, H-S., Hwang, S-H., Kim, J-M., Kim, C-U. and Choi, C. (2006), “Diminution of Current-Measurement Error for Vector-Controlled AC Motor Drives,” *IEEE Transactions On Industry Applications*, Vol. 42, No. 5, pp. 551-557.

Kanerva, S., Stulz, C., Gerhard, B., Burzanowska, H., Järvinen, J. and Seman S. (2004), “Coupled FEM and System Simulator in the Simulation of Asynchronous Machine Drive with Direct Torque Control,” In *International Conference on Electrical Machines ICEM 2004*. Cracow, Poland.

Kanerva, S. (2005). *Simulation of Electrical Machines, Circuits and Control Systems Using Finite Element Method and System Simulator*. Doctoral dissertation. Helsinki University of Technology, Finland.

Kang, J-K and Sul, S-K. (1999), “New Direct Torque Control of Induction Motor for Minimum Torque Ripple and Constant Switching Frequency,”. *IEEE Transactions on Industry Applications*, Vol. 35, No. 5, pp. 1072-1082.

Kang, J-K and Sul, S-K. (2001), “Analysis and Prediction of Inverter Switching Frequency in Direct Torque Control of Induction Machine Based on Hysteresis Bands and Machine Parameters,” *IEEE Transactions on Industrial Electronics*, Vol. 48, No. 3, pp. 545-553.

Kaukonen, J. (1999), *Salient Pole Synchronous Machine Modelling in an Industrial Direct Torque Controlled Drive Application*. Doctoral dissertation, Acta Universitatis Lappeenrantaensis 77, Lappeenranta University of Technology, Lappeenranta, Finland.

Kolar, J.W. and Ertl, H., (1991), “Influence of the Modulation Method on the Conduction and Switching Losses of a PWM Converter System,” *IEEE Transactions on Industry Applications*, Vol.27, No. 6, pp. 1063-1075.

Kovács, K.P. and Rácz, I. (1959), *Transiente Vorgänge in Wechselstrommaschinen*, I–II. Akadémia Kiadó, Budapest.

Kreyszig, E. (1993), *Advanced Engineering Mathematics*, seventh ed., New York, U.S.A.: John Wiley & Sons.

- Lascu, C., Boldea, I. and Blaabjerg, F. (2000), "A Modified Direct Torque Control for Induction Motor Sensorless Drive," *IEEE Transactions on Industry Applications*, Vol. 36., No. 1., pp. 122-130.
- Lascu, C., Boldea, I. and Blaabjerg, F. (2004), "Direct Torque Control of Sensorless Induction Motor Drives: A Sliding Mode Approach," *IEEE Transactions on Industry Applications*, Vol. 40., No. 2, pp. 582-590.
- Malinowski, M. (2001), *Sensorless Control Strategies for Three-Phase PWM Rectifiers*. Ph.D. Thesis. Warsaw, Poland
- Mecrow BC, Jack A.G. (2008), "Efficiency trends in electrical machines and drives," *Energy Policy*, Vol. 36, No. 12, pp. 4336-4341.
- Mihalcea, A., Szadados B. and Hoolboom, J. (2001), "Determining Total Losses and Temperature Rise in Induction Motors Using Equivalent Loading Methods," *IEEE Trans. on Energy Conversion*, Vol 16., No 3., pp. 214-219.
- Niemelä, M. (1999). *Position sensorless electrically excited synchronous motor drive for industrial use based on direct flux linkage and torque control*. Doctoral dissertation, Acta Universitatis Lappeenrantaensis 79, Lappeenranta University of Technology, Lappeenranta, Finland.
- Noguchi, T. and Takahashi, I. (1986), "A new quick-response and high-efficiency control strategy of an induction motor," *IEEE Trans. Industrial Applications*, vol. IA-22, pp. 820-827.
- Pohjalainen, P., Tiitinen, P. and Lalu, J. (1994), "The next-generation motor control method-direct torque control, DTC." *In Conf. Rec. EPE'94*, Orlando, FL, U.S.A., pp. 115-120.
- Polinder H., van der Pijl, F.F.A., de Vilder, G.-J., Tavner, P.J. (2006), "Comparison of direct-drive and geared generator concepts for wind turbines," *IEEE Transactions on Energy Conversion*. Vol. 21. Issue 3. pp. 725-733.
- Proakis, J.G. and Manolakis D.G. (1996), *Digital signal processing – principles, algorithms and applications*, Upple Saddle River, New Jersey: Prentice Hall, Inc..
- Pyrhönen J., Jokinen T. and Hrabovcová, V. (2008), *Design of Rotating Electrical Machines*. Chichester, England: John Wiley & Sons, Ltd.
- Pyrhönen, O. (1998), *Analysis and control of excitation, field weakening and stability in direct torque controlled electrically excited synchronous motor drives*. Doctoral dissertation. Acta Universitatis Lappeenrantaensis 74. Lappeenranta University of Technology, Finland.
- Rooks J.A. and Wallace A.K. (2004), "Energy efficiency of VSDs," *IEEE Industry Applications Magazine* 10, pp. 57-61.
- Salem, F.B. and Masmoudi A. (2007), "A comprehensive analysis of the inverter switching frequency in Takahashi DTC strategy," *The International Journal of Computation and Mathematics in Electrical and Electronic Engineering (COMPEL)*, Vol. 26. No. 1, pp. 148-166.

Slaets, B., Van Roy, R. and Belmans R. (2000), "Determining the Efficiency of Induction Machines, Converters and Softstarters," *Electromotion* vol:7 issue:2, pp.73–80.

Song, S.-H., Choi, J.-W. and Sul, S.-K. (2000), "Current Measurements in Digitally Controlled AC Drives," *IEEE Industry Applications magazine*, vol. 6, no. 4, pp. 51–62.

Sousa, G.C.D., Bose, B. K., and Cleland, J. (1992), "Loss modeling of converter induction machine system for variable speed drive," In *Proceedings of IEEE IECON'92*, IEEE, vol. 1, San Diego, CA, U.S.A., pp. 114–120.

Van Roy, P., Slaets, B. and Belmans R. (2000), *Induction Motor Efficiency: a number with many meanings*. [Online], [Accessed 9 August 2010], Available at <http://www.leonardo-energy.org/drupal/node/447>

Vas, P. (1998), *Sensorless Vector and Direct Torque Control*. New York: Oxford University Press, 1998.

**APPENDIX A PARAMETERS OF THE DRIVE SYSTEMS****Test setup 1.**

Table I. Motor parameters.

Nominal power	37 kW
Nominal voltage (delta)	400 V
Nominal current (delta)	69 A
Nominal frequency	50 Hz
Pole pairs	2
Nominal speed	1480 rpm
Rotor inertia	0.385kgm <sup>2</sup>
Stator resistance $R_s$	0.0629 $\Omega$
Rotor resistance $R_r$	0.0439 $\Omega$
Stator leakage ind. $L_{s\sigma}$	0.483 mH
Rotor leakage ind. $L_{r\sigma}$	1.003 mH
Magnetizing ind. $L_m$	28.88 mH

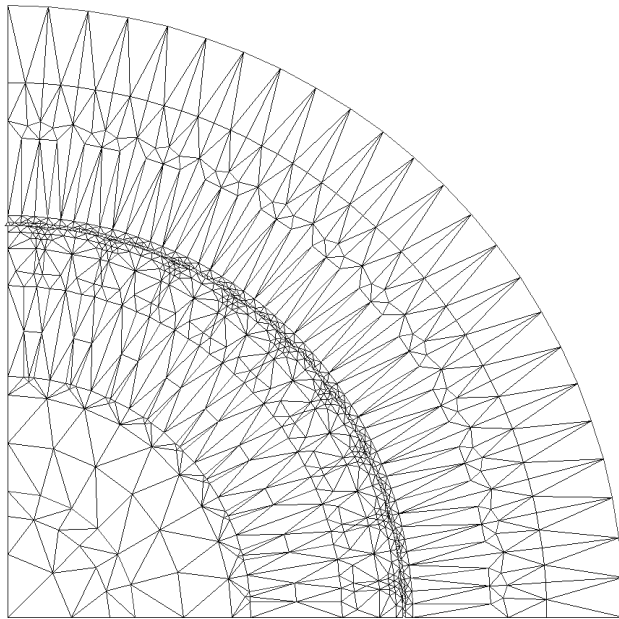


Fig A.1. 1st-order mesh of the 37 kW induction motor used in the FE analysis. The mesh contains 1448 elements and 917 nodes.

Table II. 37 kW DTC converter loss calculation parameters.

<b>Parameter</b>	<b>Explanation</b>	<b>Value</b>
$L_{\text{Input}}$	Line short circuit inductance + input choke inductance[mH]	0.386
$P_{\text{Extra}}$	Extra losses [W]	120
$R_{\text{DC L Input}}$	DC resistance of the input-choke [mΩ]	9.2
$ESR_L$	ESR value of input choke [mΩ]	14.4
$C$	DC link capacitance [mF]	2.4
$ESR_{C300}$	ESR value of DC link capacitance at 300Hz [Ω]	12.8
$ESR_{C600}$	ESR value of DC link capacitance at 600Hz [Ω]	11.0
$ESR_{C900}$	ESR value of DC link capacitance at 900Hz [Ω]	10.2
$ESR_{C1200}$	ESR value of DC link capacitance at 1200Hz [Ω]	9.9
$ESR_{C3000}$	ESR value of DC link capacitance at 3000Hz [Ω]	10.8
$R_{\text{discharge}}$	Intermediate circuit discharging resistor resistance [Ω]	33000
$R_F$	Diode on-state resistance [mΩ]	3.5
$U_F$	Diode threshold voltage [V]	0.9
$U_{\text{ce0}}$	Threshold voltage of the IGBT [V]	1.0
$U_{F0}$	Threshold voltage of the free-wheeling diode [V]	0.8
$R_{\text{ce0}}$	On-state resistance of the IGBT [mΩ]	9.3
$R_{F0}$	On-state resistance of the free-wheeling diode [mΩ]	6.7
$E_{\text{sw\_IGBT}}$	IGBT switching energy at rated current, $U_{\text{rated}}/2$ and 125°C [mWs]	45
$E_{\text{sw\_diode}}$	Free-wheeling diode reverse recovery energy at rated current, $U_{\text{rated}}/2$ and 125°C [mWs]	7

Table III. 37 kW vector converter loss calculation parameters.

Parameter	Explanation	Value
$L_{\text{Input}}$	Line short circuit inductance + input choke inductance[mH]	0.34
$P_{\text{Extra}}$	Extra losses [W]	70
$R_{\text{DC L Input}}$	DC resistance of the input-choke [ $\text{m}\Omega$ ]	7.2
$ESR_L$	ESR value of the input choke [ $\text{m}\Omega$ ]	8.2
$C$	DC link capacitance [ $\text{mF}$ ]	2.2
$ESR_{C300}$	ESR value of DC link capacitance at 300Hz [ $\Omega$ ]	7.8
$ESR_{C600}$	ESR value of DC link capacitance at 600Hz [ $\Omega$ ]	7.0
$ESR_{C900}$	ESR value of DC link capacitance at 900Hz [ $\Omega$ ]	6.2
$ESR_{C1200}$	ESR value of DC link capacitance at 1200Hz [ $\Omega$ ]	6.9
$ESR_{C3000}$	ESR value of DC link capacitance at 3000Hz [ $\Omega$ ]	6.8
$R_{\text{discharge}}$	Intermediate circuit discharging resistor resistance [ $\Omega$ ]	33000
$R_F$	Diode on-state resistance [ $\text{m}\Omega$ ]	2.2
$U_F$	Diode threshold voltage [V]	0.8
$U_{\text{ce0}}$	Threshold voltage of the IGBT [V]	1.0
$U_{F0}$	Threshold voltage of the free-wheeling diode [V]	0.7
$R_{\text{ce0}}$	On-state resistance of the IGBT [ $\text{m}\Omega$ ]	9.3
$R_{F0}$	On-state resistance of the free-wheeling diode [ $\text{m}\Omega$ ]	5.3
$E_{\text{sw\_IGBT}}$	IGBT switching energy at rated current, $U_{\text{rated}}/2$ and $125^\circ\text{C}$ [mWs]	50
$E_{\text{sw\_diode}}$	Free-wheeling diode reverse recovery energy at rated current, $U_{\text{rated}}/2$ and $125^\circ\text{C}$ [mWs]	8

**Test setup 2.**TABLE I.  
MOTOR PARAMETERS.

Nominal power	200 kW
Nominal voltage (delta)	400 V
Nominal current (delta)	350 A
Nominal frequency	50 Hz
Pole pairs	2
Nominal speed	1486 rpm
Rotor inertia $J$	3.3 kgm <sup>2</sup>
Stator resistance $R_s$	0.07 $\Omega$
Rotor resistance $R_r$	0.07 $\Omega$
Stator leakage ind. $L_{s\sigma}$	0.015 mH
Rotor leakage ind. $L_{r\sigma}$	0.280 mH
Magnetizing ind. $L_m$	6.30 mH

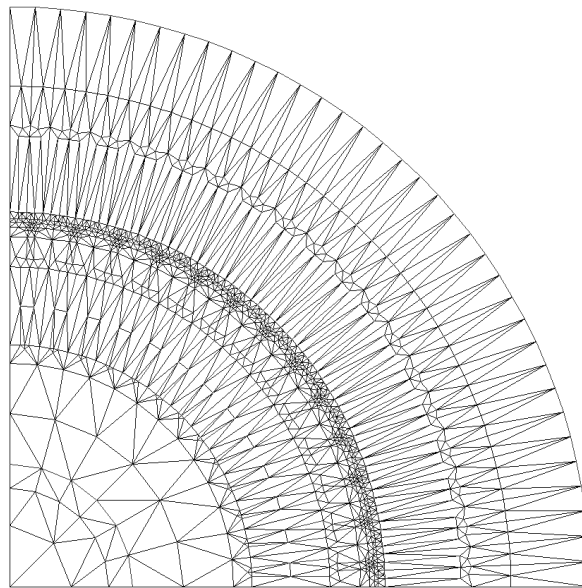


Fig. A.2: Finite element mesh of the 200 kW induction motor used in the study. The mesh consists of 2094 linear triangular elements and 1081 nodes.

**APPENDIX B EFFICIENCY MEASUREMENTS OF THE 37 kW INDUCTION MOTOR**

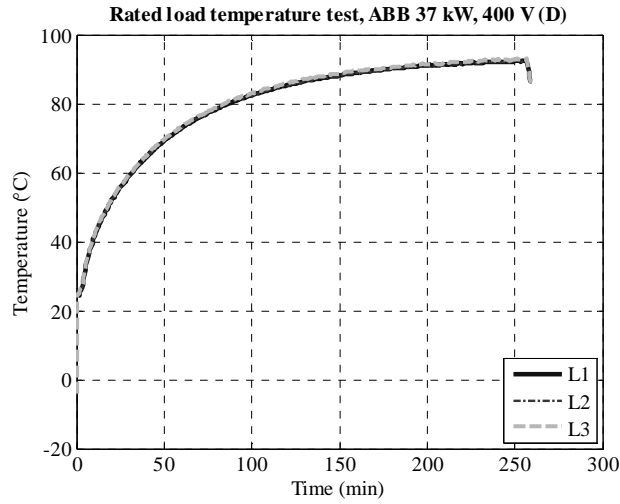


Fig. B.1: 37 kW induction motor temperatures during the rated load temperature test.

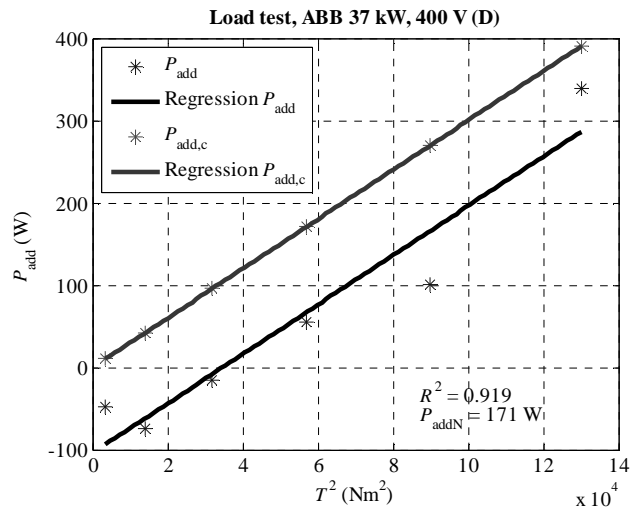


Fig. B.2: 37 kW induction motor additional losses regression lines.

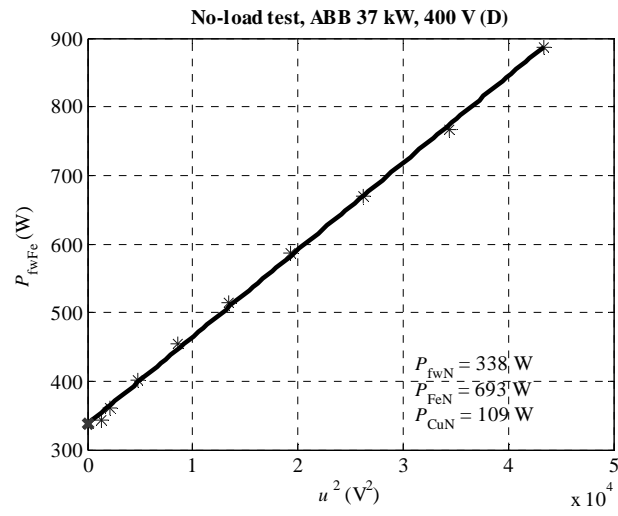


Fig. B.2: No-load test results of the 37 kW induction motor.

### APPENDIX C SPECTRA FIGURES

In the following figures, the measured and simulated current spectra of the ACS550 frequency converter are given. The simulations have been carried out with the analytical motor model discussed above. It should be noted that both the  $x$ - and  $y$ -axis scales in the figures are different from each other.

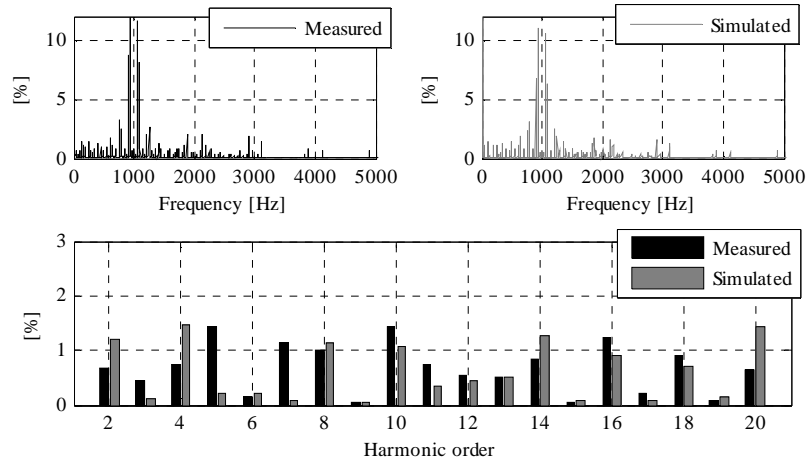


Fig C.1. Spectra of the simulated and measured motor phase currents of the 37 kW induction motor. The carrier frequency is set to 1000 Hz. The fundamental wave (25 Hz) is scaled outside the figure.

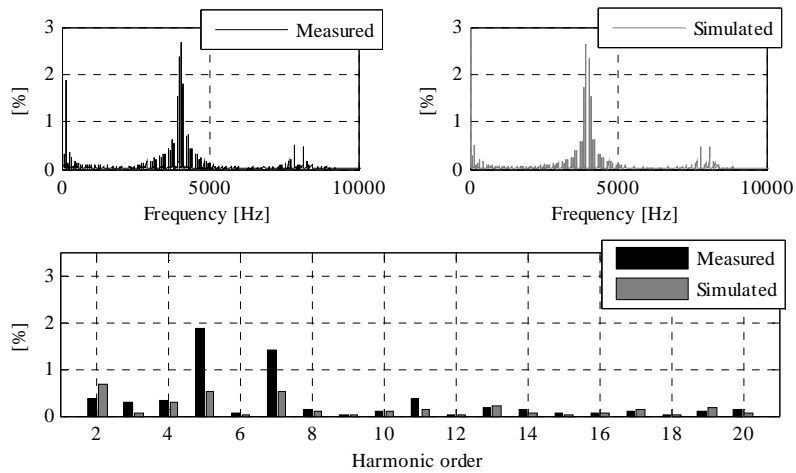


Fig C.2. Spectra of the simulated and measured motor phase currents of the 37 kW induction motor. The carrier frequency is set to 4000 Hz. The fundamental wave (25 Hz) is scaled outside the figure.

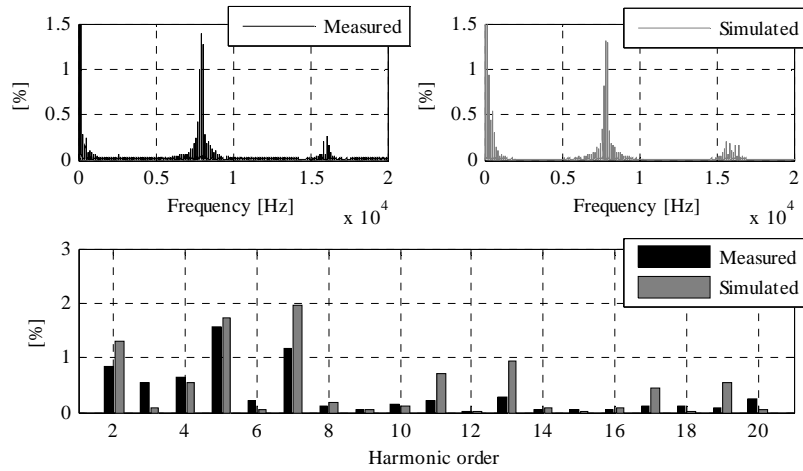


Fig C.3. Spectra of the simulated and measured motor phase currents of the 37 kW induction motor. The carrier frequency is set to 8000 Hz. The fundamental wave (25 Hz) is scaled outside the figure.

In the following figures, the measured and simulated current spectra of the ACS550 frequency converter are given. The simulations have been carried out with the FEM motor model. It should be noted that both the  $x$ - and  $y$ -axis scales in the figures are different from each other.

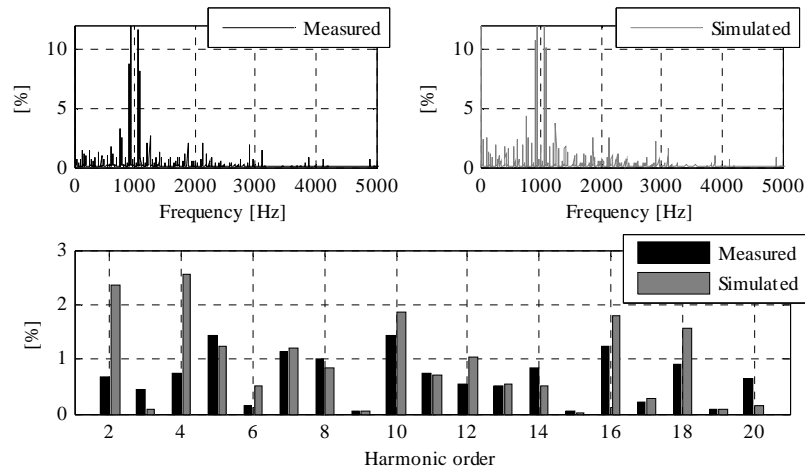


Fig C 4. Spectra of the simulated and measured motor phase currents of the 37 kW induction motor. The carrier frequency is set to 1000 Hz. The fundamental wave (25 Hz) is scaled outside the figure.

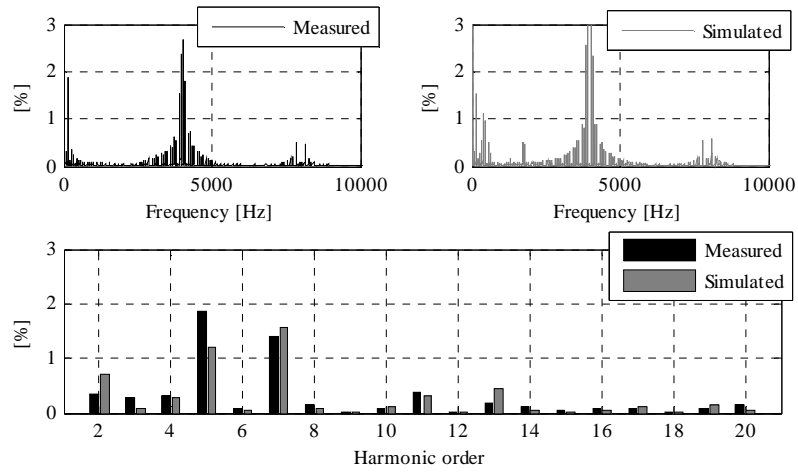


Fig C 5. Spectra of the simulated and measured motor phase currents of the 37 kW induction motor. The carrier frequency is set to 4000 Hz. The fundamental wave (25 Hz) is scaled outside the figure.

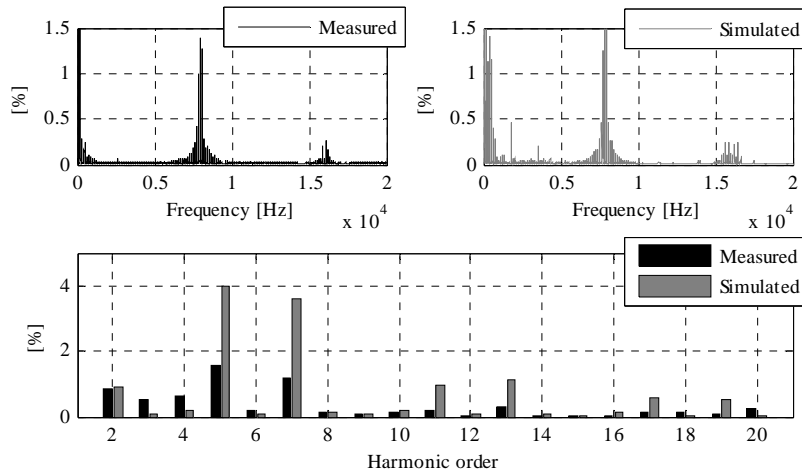


Fig C 6. Spectra of the simulated and measured motor phase currents of the 37 kW induction motor. The carrier frequency is set to 8000 Hz. The fundamental wave (25 Hz) is scaled outside the figure.

In the following figures, the measured and simulated current spectra of the ACS800 frequency converter are illustrated. The simulations have been carried out with the analytical motor model discussed earlier. It should be noted that both the  $x$ - and  $y$ -axis scales in the figures are different from each other.

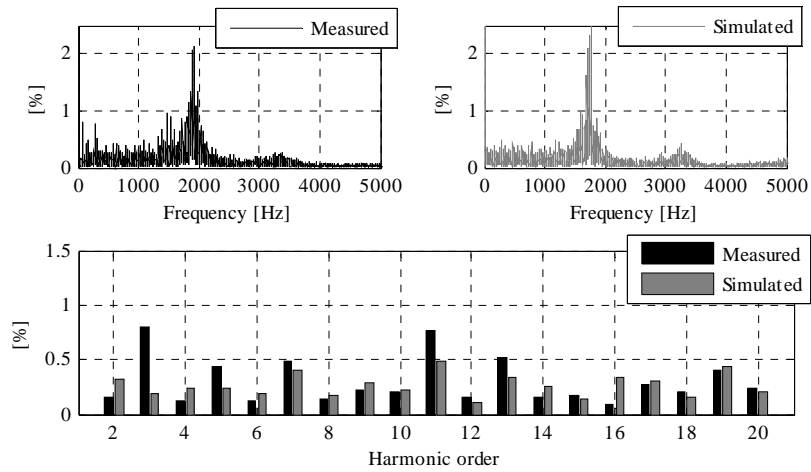


Fig C 7. Spectra of the simulated and measured motor phase currents of the 37 kW induction motor. The switching frequency is set to 1000 Hz. The fundamental wave (25 Hz) is scaled outside the figure.

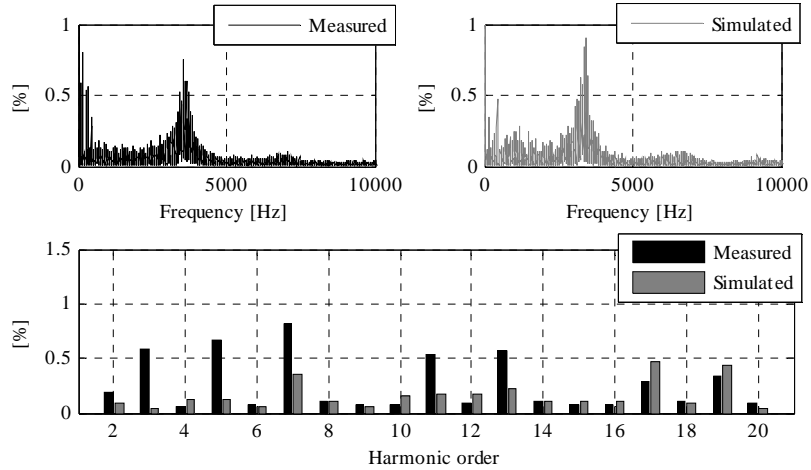


Fig C 8. Spectra of the simulated and measured motor phase currents of the 37 kW induction motor. The switching frequency is set to 2000 Hz. The fundamental wave (25 Hz) is scaled outside the figure.

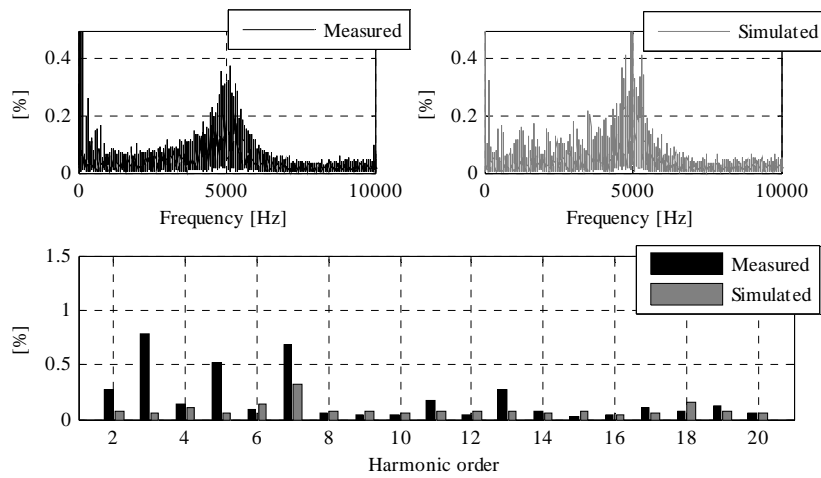


Fig C.9. Spectra of the simulated and measured motor phase currents of the 37 kW induction motor. The switching frequency is set to 3000 Hz. The fundamental wave (25 Hz) is scaled outside the figure.

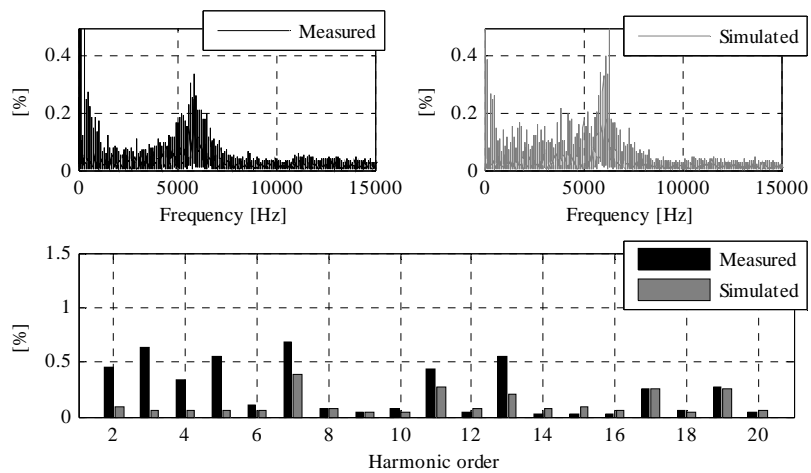


Fig C.10. Spectra of the simulated and measured motor phase currents of the 37 kW induction motor. The switching frequency is set to 3750 Hz. The fundamental wave (25 Hz) is scaled outside the figure.

In the following figures, the measured and simulated current spectra of the ACS800 frequency converter are illustrated. The simulations have been carried out with the FEM motor model. It should be noted that both the  $x$ - and  $y$ -axis scales in the figures are different from each other.

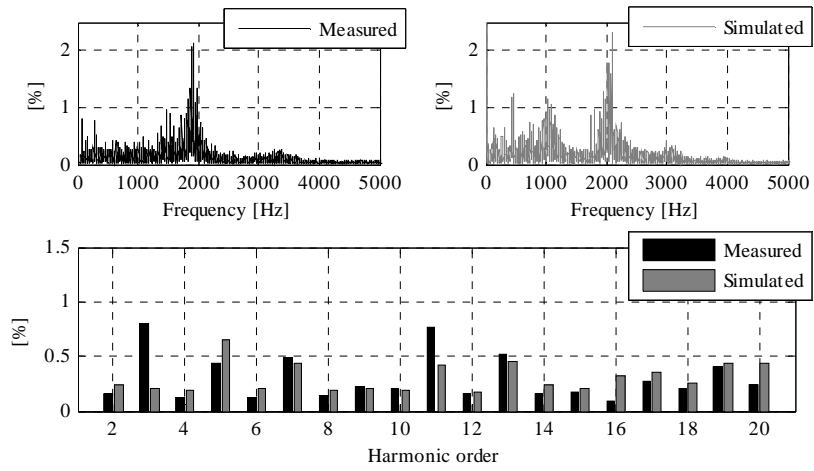


Fig C 11. Spectra of the simulated and measured motor phase currents of the 37 kW induction motor. The switching frequency is set to 1000 Hz. The fundamental wave (25 Hz) is scaled outside the figure.

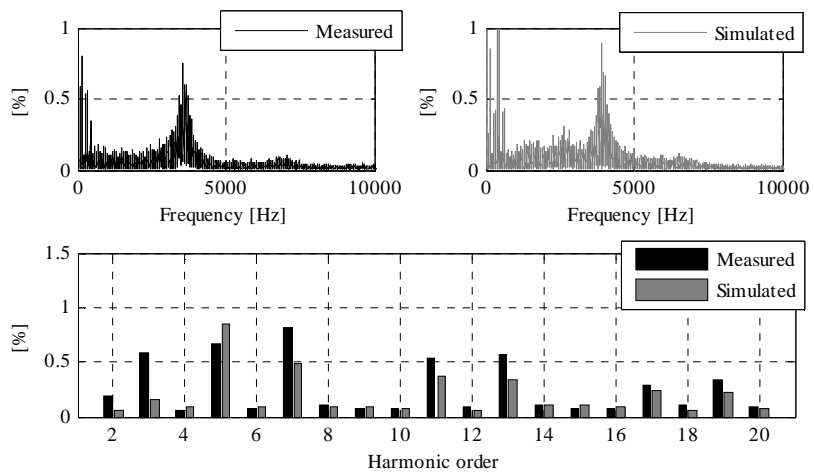


Fig C 12. Spectra of the simulated and measured motor phase currents of the 37 kW induction motor. The switching frequency is set to 2000 Hz. The fundamental wave (25 Hz) is scaled outside the figure.

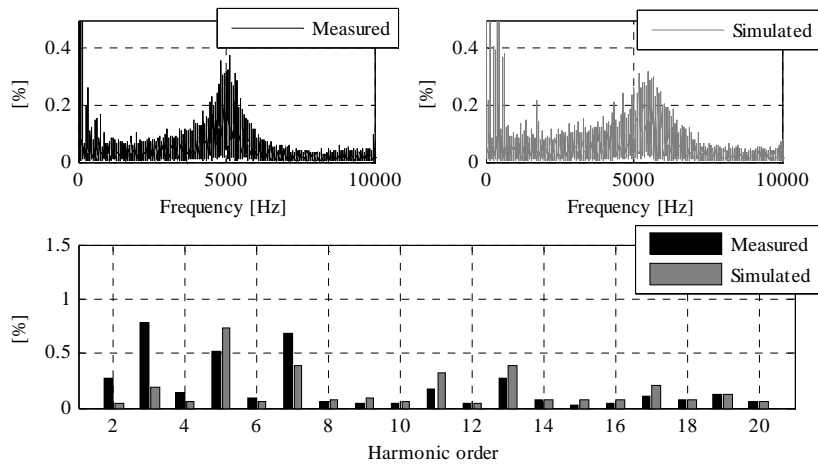


Fig C 13. Spectra of the simulated and measured motor phase currents of the 37 kW induction motor. The switching frequency is set to 3000 Hz. The fundamental wave (25 Hz) is scaled outside the figure.

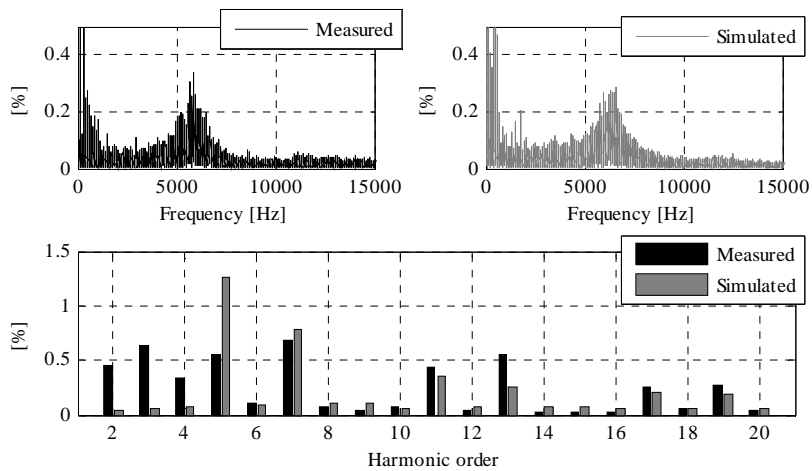


Fig C 14. Spectra of the simulated and measured motor phase currents of the 37 kW induction motor. The switching frequency is set to 3750 Hz. The fundamental wave (25 Hz) is scaled outside the figure.

## ACTA UNIVERSITATIS LAPPEENRANTAENSIS

353. KOHONEN, JARNO. Advanced chemometric methods: applicability on industrial data. 2009. Diss.
354. DZHANKHOTOV, VALENTIN. Hybrid LC filter for power electronic drivers: theory and implementation. 2009. Diss.
355. ANI, ELISABETA-CRISTINA. Minimization of the experimental workload for the prediction of pollutants propagation in rivers. Mathematical modelling and knowledge re-use. 2009. Diss.
356. RÖYTTÄ, PEKKA. Study of a vapor-compression air-conditioning system for jetliners. 2009. Diss.
357. KÄRKI, TIMO. Factors affecting the usability of aspen (*Populus tremula*) wood dried at different temperature levels. 2009. Diss.
358. ALKKIOMÄKI, OLLI. Sensor fusion of proprioception, force and vision in estimation and robot control. 2009. Diss.
359. MATIKAINEN, MARKO. Development of beam and plate finite elements based on the absolute nodal coordinate formulation. 2009. Diss.
360. SIROLA, KATRI. Chelating adsorbents in purification of hydrometallurgical solutions. 2009. Diss.
361. HESAMPOUR, MEHRDAD. Treatment of oily wastewater by ultrafiltration: The effect of different operating and solution conditions. 2009. Diss.
362. SALKINOJA, HEIKKI. Optimizing of intelligence level in welding. 2009. Diss.
363. RÖNKKÖNEN, JANI. Continuous multimodal global optimization with differential evolution-based methods. 2009. Diss.
364. LINDQVIST, ANTTI. Engendering group support based foresight for capital intensive manufacturing industries – Case paper and steel industry scenarios by 2018. 2009. Diss.
365. POLESE, GIOVANNI. The detector control systems for the CMS resistive plate chamber at LHC. 2009. Diss.
366. KALENOVA, DIANA. Color and spectral image assessment using novel quality and fidelity techniques. 2009. Diss.
367. JALKALA, ANNE. Customer reference marketing in a business-to-business context. 2009. Diss.
368. HANNOLA, LEA. Challenges and means for the front end activities of software development. 2009. Diss.
369. PÄTÄRI, SATU. On value creation at an industrial intersection – Bioenergy in the forest and energy sectors. 2009. Diss.
370. HENTTONEN, KAISA. The effects of social networks on work-team effectiveness. 2009. Diss.
371. LASSILA, JUKKA. Strategic development of electricity distribution networks – Concept and methods. 2009. Diss.
372. PAAKKUNAINEN, MAARET. Sampling in chemical analysis. 2009. Diss.
373. LISUNOV, KONSTANTIN. Magnetic and transport properties of II-V diluted magnetic semiconductors doped with manganese and nickel. 2009. Diss.

374. JUSSILA, HANNE. Concentrated winding multiphase permanent magnet machine design and electromagnetic properties – Case axial flux machine. 2009. Diss.
375. AUVINEN, HARRI. Inversion and assimilation methods with applications in geophysical remote sensing. 2009. Diss.
376. KINDSIGO, MERIT. Wet oxidation of recalcitrant lignin waters: Experimental and kinetic studies. 2009. Diss.
377. PESSI, PEKKA. Novel robot solutions for carrying out field joint welding and machining in the assembly of the vacuum vessel of ITER. 2009. Diss.
378. STRÖM, JUHA-PEKKA. Active  $du/dt$  filtering for variable-speed AC drives. 2009. Diss.
379. NURMI, SIMO A. Computational and experimental investigation of the grooved roll in paper machine environment. 2009. Diss.
380. HÄKKINEN, ANTTI. The influence of crystallization conditions on the filtration characteristics of sulphathiazole suspensions. 2009. Diss.
381. SYRJÄ, PASI. Pienten osakeyhtiöiden verosuunnittelu – empiirinen tutkimus. 2010. Diss.
382. KERKKÄNEN, ANNASTIINA. Improving demand forecasting practices in the industrial context. 2010. Diss.
383. TAHVANAINEN, KAISA. Managing regulatory risks when outsourcing network-related services in the electricity distribution sector. 2010. Diss.
384. RITALA, PAAVO. Coopetitive advantage – How firms create and appropriate value by collaborating with their competitors. 2010. Diss.
385. RAUVANTO, IRINA. The intrinsic mechanisms of softwood fiber damage in brown stock fiber line unit operations. 2010. Diss.
386. NAUMANEN, VILLE. Multilevel converter modulation: implementation and analysis. 2010. Diss.
387. IKÄVALKO, MARKKU. Contextuality in SME ownership – Studies on owner-managers' ownership behavior. 2010. Diss.
388. SALOJÄRVI, HANNA. Customer knowledge processing in key account management. 2010. Diss.
389. ITKONEN, TONI. Parallel-Operating Three-Phase Voltage Source Inverters – Circulating Current Modeling, Analysis and Mitigation. 2010. Diss.
390. EEROLA, TUOMAS. Computational visual quality of digitally printed images. 2010. Diss.
391. TIAINEN, RISTO. Utilization of a time domain simulator in the technical and economic analysis of a wind turbine electric drive train. 2010. Diss.
392. GRÖNMAN, AKI. Numerical modelling of small supersonic axial flow turbines. 2010. Diss.
393. KÄHKÖNEN, ANNI-KAISA. The role of power relations in strategic supply management - A value net approach. 2010. Diss.
394. VIROLAINEN, ILKKA. Johdon coaching: Rajanvetoja, taustateorioita ja prosesseja. 2010. Diss.
395. HONG, JIANZHONG. Cultural aspects of university-industry knowledge interaction. 2010. Diss.